Revista Brasileira de Ciências Mecânicas

1

REVISTA BRASILEIRA DE CIÊNCIAS MECÂNICAS
JOURNAL OF THE BRAZILIAN SOCIETY OF MECHANICAL SCIENCES

A REVISTA BRASILEIRA DE CIÊNCIAS MECÂNICAS publica trabalhos que cobrem os vários aspectos da ciência e da tecnologia em Engenharia Mecânica, incluindo interfaces com as Engenharias Civil, Elétrica, Química, Naval, Nuclear, Aeroespacial, Alimentos, Agrícola, Petróleo, Materiais, etc., bem como aplicações da Física e da Matemática à Mecânica.

Preliminary Considerations on a New Design Concept for Below the Knee Energy Storing Prosthesis

Felipe Nogueira
Instituto Tecnológico de Aeronáutica
Departamento de Estruturas

Sérgio F. Muller de Almeida
Instituto Tecnológico de Aeronáutica
Departamento de Projetos
12228-900 S. José dos Campos, SP Brazil

Abstract

This study develops a concept for the design and manufacture of energy storing prosthesis that attempts to simplify the design process of such prosthetic devices. This concept consists of three basic steps: identifying design requirements, computational analysis and tests. The most relevant parameters used in the process and design compromises between these parameters are identified and explained. Non linear behavior and expected results of non linear finite element analyses are explained together with an overview of laboratory and field tests performed. Some critical points identified in preliminary test results are presented. The methodology proposed was successfully applied to the development of a composite material energy storing prosthesis.
Keywords: Energy Storing Prosthesis, Composite Material, Biomechanics

Introduction

Advances in design and research of new materials have caused a change in the market of solid ankle prosthetic devices in recent years. This advances, allied with a growing demand for prosthesis that improve athletic performance, led to the development of energy storing prostheses (ESP).

ESP are high performance solid ankle flexible prostheses designed to store and release energy during gait. They have special characteristics that make them more attractive and comfortable than conventional prostheses. Some of these characteristics are:

- Less shock transmission;
- Better damping properties;
- Less weight, and
- Better response.

These new prostheses are designed so that their keel deforms during the second and third stages of the stance phase of gait (after heel strike), thus storing energy as a deformed spring. Therefore, kinetic energy from the swing phase is transformed into potential energy. Afterwards, in the stage of stance (toes off), the keel returns to its undeformed position releasing energy and helping to push the amputee into the swing phase of gait. At this instance, potential energy is converted again into kinetic energy.

Even though the benefits of ESP for below the knee amputees (BKA) have been reported by many sources (Gailey et al., 1994; and Alaranta et al., 1994), these is still a shortage of ESP in the Brazilian market.

The problem at hand is to design an inexpensive device that will improve the energy efficiency, therefore reducing the energy expenditure of BKA. Energy expenditure of a prosthesis can be defined as the difference of energy stored and energy lost due to hysteresis. It can be measured using ambulation techniques (Colborne, 1992) and estimated from finite element analyses.

Reducing energy expenditure is the same as maximizing energy efficiency. This can be achieved by enhancing the load transferring from heel to toes, simulating the action of foot and ankle. Also, new materials that reduce weight and help on the performance can be used.

Barr et al. (1992) calculated the energy efficiency of the Carbon Copy II® energy storing prosthetic foot of Flex Foot Inc., and of the SACH (solid ankle cushioned heel) foot of Otto Bock. The

ESP returned energy with an efficiency of 57% while the SACH foot returned only 29.3% of the energy it stored.

Colborne (1992) compared oxygen consumption during level walking of subjects fitted with the SACH foot, and with the energy storing Seattle Ankle/Lite® foot. The results of this work indicated that the oxygen consumption was significantly higher in the SACH foot, leading to the conclusion that the ESP reduced energy expenditure of the subjects tested.

The complexity, however, lies in the subjectivity of the problem. Each BKA is a particular case and requires a set of design parameters. Moreover, each BKA has a particular preference on how to adjust each of these parameters.

The objective of this research is to develop a new design concept. This new concept has to reduce manufacturing costs, conserve the characteristics of ESP and be customizable so it can be adapted to the subjectivity discussed above.

One of the main concerns is to establish the influence of measurable engineering quantities on comfort and on the design parameters. By doing so, it is possible to satisfy the BKA's preferences by adjusting the quantity that influences a particular design parameter.

This is achieved by manufacturing keels with different geometry. This way, it is possible to observe the change in engineering terms as well as in performance and comfort.

This design concept is just a set of steps that need to be taken in order to design and manufacture an ESP. Correlation to the results of some prototype tests are presented, but final design and results are not presented here. Final design and results are beyond the scope of this work.

Design Concept

The concept developed in the study consists of three main phases: identifying design requirements, computational analyses and tests.

In the first phase, the intention is to clarify objectives and set the general requirements of the design. The second and third phases are used to generate alternatives and to evaluate them in order to improve on the original designs.

One of the purposes of this article is to present the objectives of this design concept, which are, among others:

- Provide all necessary information for mold production;
- Adapt the design process to subjectivity;
- Reduce manufacturing costs;
- Reduce BKA's energy expenditure, and
- Improve performance.

Design Requirements. In order to determine the design requirements, the parameters involved have to be listed in advance. Therefore, a tree of objectives (Dieter, 1991) was constructed in order to clarify objectives and identify the design parameters.

The most relevant design parameters used in this study are:

- BKA's data (weight, foot size, physical activity, etc.);
- Strength;
- User Comfort;
- Stiffness;
- Durability;
- Material, and
- Manufacturing facilities.

The design is driven by compromises between the above parameters. Compromises of stiffness versus strength and user comfort are particularly important. In short, the prosthetic device has to be flexible to provide comfort but strong enough to withstand daily use under the BKA's specified level of physical activity.

Laminated graphite/epoxy composite materials were selected to be used in the prototypes because of their excellent mechanical properties. These materials can be tailored to sustain large loads and large deformations while maintaining their structural integrity and fatigue resistance.

Composite materials also have good orientation capabilities. The problem at hand calls for a material with mainly longitudinal properties, therefore the plies can be placed in a way to maximize the bending strength of the ESP, without compromising comfort.

The manufacturing facilities available are also important at the design stage. The designer should pay close attention to the manufacturing capabilities at his/her disposal so the prototypes can be easily manufactured.

Keels with different geometry were manufactured according to the design requirements specified above. One of these keels is shown in Fig. 1, together with a graphite/epoxy pylon.

The pylons were also manufactured using composite materials in order to minimize weight and fatigue problems. Several aluminum pylons fail due to fatigue as discussed by Wevers and Durance (1987).

Computational Analyses. This step was performed using the software ARIES for geometric modeling and NASTRAN for finite element (FE) analysis.

A geometric model was developed using the ARIES solid modeller. This model was useful in determining:

- Mass properties;
- Surface areas;
- Moments of inertia;
- Finite element model, and
- Mold fabrication.

Mass and inertia properties as well as surface areas are readily available from the model without the need of new analysis. These properties and areas are helpful in cost evaluation, mold fabrication and speeding the manufacturing of prototypes.

Finite element analyses were responsible for predicting the behavior of the prototype under testing conditions. They were also helpful in predicting failure indexes of the various plies of composite materials as well as predicting the maximum loads that the prototype could withstand.
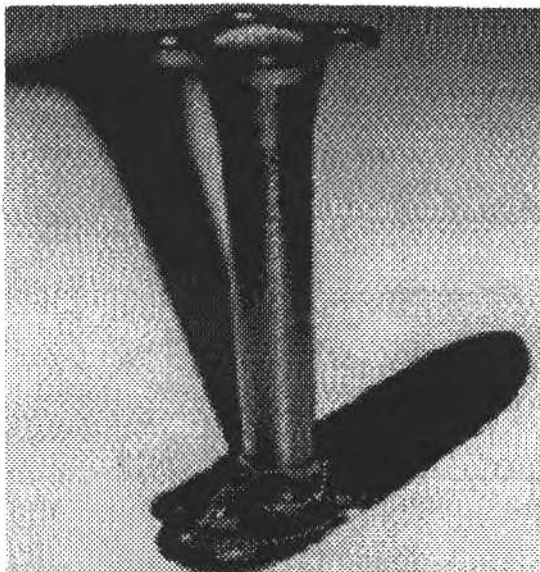
Fig. 1   Preliminary Design of an Energy Storing Prosthesis

The type of analysis performed was non linear because, as seen in Fig. 2, the load versus displacement curve of an ESP is non linear. This is due to the large displacements to which prostheses are submitted in regular use.

The non linear behavior of the prosthesis is controlled by some factors, among which:

- Laminate thickness;
- Keel taper, and
- Laminate lay up.

The interpretation of the graph in Fig. 2 shows a stiffening behavior as the load increases. This is a characteristic of ESP. Note that the area under the curve corresponds to the energy stored by the device during the first stages of the stance phase of gait.

Figure 2 shows the load vs displacement curve corresponding to a particular test with loads up to a level of 1500N. The degree of non linearity is not shown with accuracy in the figure because actual loading is higher (up to 4500N). Higher loads results in further stiffening not shown in the graph and, thus, in an augmented degree of non linearity.

Some of the energy is lost due to hysteresis, and some is returned to the BKA. The difference between the energy stored and the energy lost due to hysteresis dictates the efficiency of the device.

Therefore, the amount of energy lost due to hysteresis should be minimized. By doing so, one maximizes the energy efficiency of the ESP. FE analysis can be used to estimate the energy efficiency and modify the design so better energy efficiency can be achieved.

The output of a given FE analysis also points out the region with higher stress concentrations, worst stress gradients and failure indexes. Therefore, it is possible to determine critical points in the design, from a structural point of view, and change material or geometry to correct any imperfections.

Tests. The prototype keels were also submitted to several tests to validate and improve the design. These tests were used to simulate the actual loads that BKA submit their prosthesis to in regular use.

Two separate families of tests were performed. Laboratory tests were conducted using an Instron machine and field tests were performed with the assistance of a volunteer and a certified prosthetist.

Fig. 2   Typical Load vs. Displacement Graph of an ESP

Laboratory static tests performed consisted of a static proof test and a static test to failure. Specimens that passed the proof test were used in the failure test.

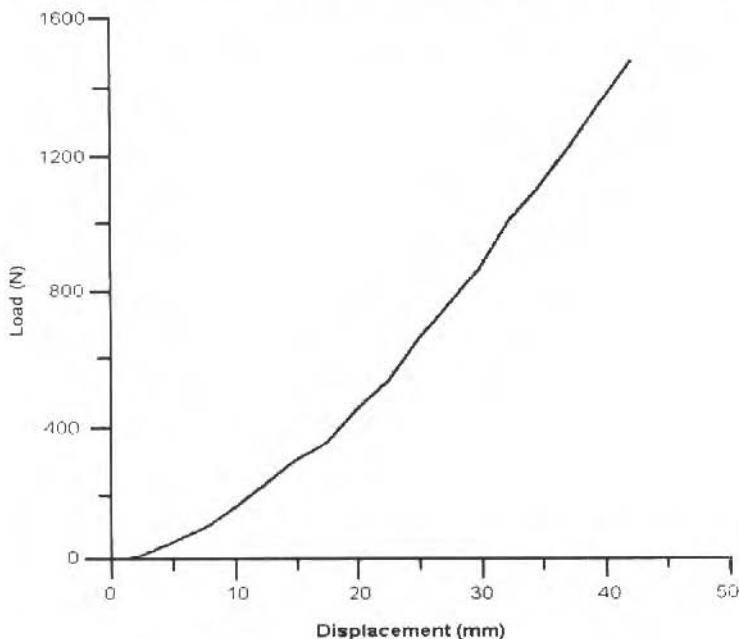The basic guidelines of the laboratory tests followed recommendations present in a document being circulated by the International Standardization Committee (ISO). This document is being circulated as a Draft International Standard and attempts to standardize the tests of lower limb prosthetics.

The amount of load applied in the proof test was determined following the guidelines of the ISO document. This document also provide guidelines to fatigue tests not concluded at the time of this publication.

The line of load application was determined based on a work by Grundy et al. (1975). According to this study, the forefoot supports most of the loading, about three times as much as the heel.

Moreover, the work points out that the maximum load in the forefoot occurs at a point in time just before the opposite's foot heel strikes the ground. This point is determined to be about 70 to 75 % of the foot's length, starting from the heel as seen in Fig. 3 (Grundy et al., 1975). This conclusions are also supported by a work of Wevers and Durance (1987).

Figure 3 shows the typical graphs of forces and center of pressure of the foot. Note that there are two load points marked as T and H. These letters mark the positions at which the opposite's foot toes leave the ground (T) and when the opposite's foot heel touch the ground (H).

Field tests consisted of a preliminary test to identify critical points in the design at an early stage and tests to determine geometry.

The preliminary field test identified four critical design issues: heel height, flexibility of heel and toes and pylon orientation adjustment. The subject fitted with the prototype affirmed that the heel was too rigid while the other extremity was not rigid enough. Another critical issue, adjustment, was raised during test reviewing with the certified prosthetist. In this reviewing, test results, prosthesis fitting and periodical adjustments were discussed.

Final tests are planned to test several keel with different thickness and taper. These tests will assess the influence of different aspects of the chosen geometry on the design parameters.

Mainly, the last test runs are designed so information on keel tapering can be obtained. The overall behavior of the keel is highly dependent on the geometry. After this last tests, the production molds will be manufactured.
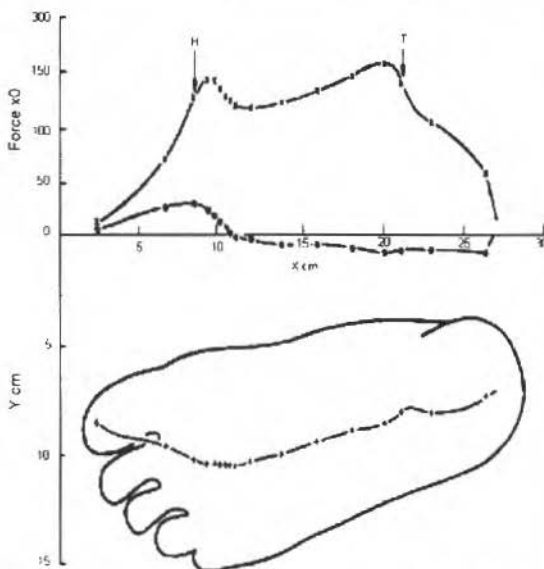

Fig. 3   Schematic Representations of Forces Under the foot (top) and Center of Pressure (Bottom) (Grundy et al., 1975)

Field Test Results

The results of the field tests were briefly commented in the last section. They are based on amputee's observations, and the main issues that appeared were:

- Heel not high enough;
- Heel is too rigid;
- Toes are not rigid enough, and
- Better adjustment of the pylon orientation is needed.

The heel height was found to be an important parameter. This is due to the fact that the higher the heel, the longer the deflecting portion of the keel. As the deflecting part of the keel is extended, there is more energy stored and released during a gait cycle.

The rigidity of the heel was considered the most critical point of the prosthesis. Some attempts are being made to soften the heel, but a compromise between heel softness and height is needed. Observations have also led to the conclusion that it is better to loose some softness in the heel than to loose height.

If the heel is too soft, it will sink more as it touches the ground and, thus, decrease the portion of the keel available for defection. On the other hand, if the heel is set rigid and high, there will be a greater portion of the heel available for deflection while shock absorption at the heel will be worse.

The problem with the rigidity of the toes has to do with the swing phase. The amputee complained that there was not enough push from the stance of gait to the swing phase. This is being corrected by means of a change in geometry.

Each BKA is a different problem. Therefore the prosthesis alignment is particular to each one. Sometimes, even a small adjustment will have an effect on the gait pattern of an amputee. So the adjustment of the ESP should be able to accommodate these fine tunings.

Adjustments in most commercial prosthesis are achieved using the well known pyramid mechanism. A newer adjustment mechanism that simplifies the work of the prosthetist is being tested.

There were some points in favor of the design as well. Among them, it is worth noticing the following:

- Keel as a whole is responding well, and
- Good response also at accelerated march.

As an ESP, the prototype is responding well to the loads of daily use in either laboratory or real life environment. The amputee walked with comfort and with no other complaints, except from the heel rigidity.

The assembly was simple and set up time was comparable to other prosthesis in the market.

Conclusions

The new design concept presented in this work attempts to simplify the design process of ESP. It identified the major design parameters as well as the major design objectives. Design phase and its objectives were also identified and their peculiarities were explained in a simplified fashion.

Computational analyses proved to be an effective way of predicting the behavior of a prototype before it is actually manufactured. The non linear behavior of ESP can be easily modeled in the FE analyses, speeding the design process.

Laboratory tests are being conducted, but the non linear behavior of the prosthesis has been confirmed. Figure 2 shows a typical load versus displacement curve of prototypes.

Field tests were able to determine critical points in the design at an early stage. Other tests are being performed to assess the influence of keel tapering on engineering quantities and comfort.

Test results also proved that the design concept was able to produce an energy storing prosthesis that compared well to some of the leading prosthesis in the international market. According to the test

subject, the overall performance of the prototype prosthesis was better than that of an Otto Bock Dynamic Foot® or to that of a Seattle Ankle/Life Foot®

The design concept proved to be an effective tool in the early design stages. Its phases, identifying design requirements, computational analyses and tests, are common practice in the engineering design procedure. This methodology was successfully applied to the development of the composite material ESP.

In conclusion, some of the major points of the problem itself worth noticing are:

*   Subjectivity;
*   Problem is non linear and presents stiffening;
*   Composite materials are used because of their properties, and
*   Design concept follows three phases.

Acknowledgments

References

Alaranta, H., et al., 1994, "Subjective Benefit of Energy Storing Prosthesis", Journal of Prosthetic and Orthotics, Vol. 2, pp. 92-97.

Barr, A. E., et al., 1992 "Biomechanical Comparison of the Energy-Storing Capabilities of Sach and Carbon Copy II Prosthetic Feet During the Stance Phase of Gait in a Person with Below-Knee Amputation", Physical Therapy, Vol. 72, pp. 344-354.

Colborne, C. R., 1992, "Analysis of Mechanical and Metabolical Factors in the Gait of Below Knee Amputees", American Journal of Physical and Medical Rehabilitation, Vol. 71, pp. 272-278.

Dieter, G. E., 1991, "Engineering Design, a Material and Processing Approach", McGraw-Hill, Inc., New York.

Gailey, R. S., et al., 1994, "Energy Expenditure of Trans-Tibial Amputees during Ambulation at Self-Selected Pace",Journal of Prosthetics and Orthotics, Vol. 2, pp. 84-91.

Grundy, M., et al., 1975, "An Investigation of the Centres of Pressure Under the Foot While Walking". The Journal Of Bone and Joint Surgery, Vol. 57-B, pp. 98-103.

Wevers, H. W., and Durance, J. P., 1987, "Dynamic Testing of Below-Knee Prosthesis: Assembly and Components", Prosthetics and Orthotics International, Vol. 11, pp. 117-123.

Dynamic Response of a Damped Cable With a Compliant Damped Support System

Elias Bittencourt Teodoro
Universidade Federal de Uberlândia
Departamento de
38400-206 Uberlândia, MG Brasil

Kenneth G. McConnell
Iowa state University - USA
50011 - Ames, LA

Abstract

Power lines are subject to complex aerodynamic forces that may cause galloping. Then a mathematical model was developed in which the conductor is represented by a taut string and the insulator support is modeled as a mass, spring, and damper. A technique called model modification was employed to study this model. A computer program was written to simulate the behavior of the cable under certain boundary conditions while different types of excitations are applied to the cable. The mode-summation method was successfully applied to this class of problem and the advanced model analysis indicated that energy absorber device reduced cable motion while reducing the forces transmitted to the supporting tower.
Keywords: Damped Cable, Support Systems, Mode - Summation Method

Introduction

The study of cable dynamics is a classical problem, and the analysis of oscillations of a cable has been of interest for many decades. Currently, wind-excited oscillations of overhead line continue to cause serious wear in cables and their structures.

A wide range of problems and applications are encountered in the literature; this literature, however, varies greatly in terms of simplifying assumptions and solution techniques. The simplest problem, of course, is the vibrating string problem with its attendant assumptions of constant cable tension and small deflection. Other solutions are available for certain restricted classes of the nonlinear equations of motion for large deflections of an elastic string.

The vibration modes and natural frequencies of a string, inextensible cable have been analyzed by Goodey (1961), Pusgley (1949), and Saxon and Cahn (1953). Dominguez (1972) used an inextensible discrete system approach to formulate the initial value problem, which is solved by using Laplace transforms. Cowper et al.(1973), Irvine(1974), Soler(1970), and West et al.(1975) determined the natural frequencies from the equations of motion for small oscillations of a shallow catenary.

The galloping phenomenon is highly complex because of the nonlinear, geometry-dependent, time-varying aerodynamic loads and the resulting amplitudes of vibration, which may cause interactions between various vibration modes and also between adjacent spans and their support hardware. To establish the basic mechanism of cable galloping, researchers have presented theories that try to explain the galloping phenomenon. At least two mechanisms have been introduced: the Den Hartog theory and the torsional theory. The Den Hartog theory argues that instability occurs when the absolute value of the negative slope section of the lift coefficient is larger than the drag coefficient.

Nigol and Buchan(1981) have done an extensive study concerning the vibration of a model transmission line in a simulated environment. They conclude that Den Hartog mechanism is not the cause of galloping. Their opinion is that galloping is caused largely by a self-excited torsional mechanism. The torsional theory suggests that galloping is caused by wind-induced torsional oscillations of the iced conductor that generate vertical oscillatory aerodynamic forces.

McConnell and Zemke(1980) have studied the coupled axial-torsional properties of ACSR electric conductors and Samras et al. (1974) have studied the coupling effect of underwater cables; both groups obtained similar results on the torsional-extensional properties. Samras et al. (1974) based their analysis on a linear model that is rather limited in its applications, because a nonlinear system such as

a catenary can behave quite differently than a linear system. However, the coupling effect developed separately by these two groups suggests that axial-torsional coupling may provide a tentative explanation for the torsional mechanism that appears to control galloping.

It was concluded by Myerscough(1973) that a conductor appears to settle ultimately into an oscillation pattern dominated by one particular harmonic or mode shape. Since the vertical motion is most dominant during galloping motion, we concentrated our attention on developing a mathematical model that includes only the first few mode shapes. This model should provide guidance in designing an energy absorber that will reduce both the magnitude of galloping and the peak impact loads that can occur at the support structure.

The Mathematical Model

A mathematical model was developed in which the conductor is represented by a taut string and the insulator support is modeled as a mass, spring, and damper. A schematic of a cable system is shown in Fig. 1. A technique called modal modification was employed to study this model. The advantage of this technique is that once the computer model is working with the taut string, it is a rather simple matter to implement a multispan catenary model. A computer program was written to simulate the behavior of the cable under certain boundary condition while different types of excitations are applied to the cable.
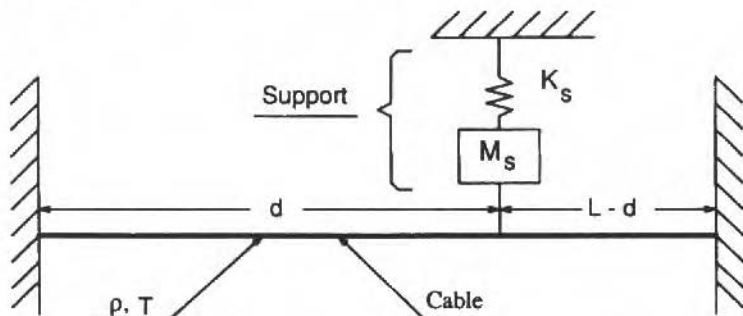
Fig. 1 A Taut Damped Cable with Mass-Spring Support at x = d

First we consider a differential element of a taut cable under tension T where density per unit length is considered constant. The cable is assumed to be like a string and offers no resistance to bending moments. It is further assumed that the string performs a small transverse motion in a vertical plane. The deflection slope at every point of the string are small in absolute value so that any variation in the tension due to the displacement of the string is negligible. From these assumptions the free-body diagram of a portion of the deflected string, the external loads of Fs(x,t), E(x,t) are applied. Real cable systems are influenced by a gravitational field g and a distributed damping along the string c [Ns/m²], the resulting differential equation of motion in the vertical direction in given by

$$T\frac{\partial^2 y(x,t)}{\partial x^2} - c\frac{\partial y(x,t)}{\partial x} - F_S(x,t) + E(x,t) - \rho g = \rho\frac{\partial^2 y(x,t)}{\partial t^2} \tag{1}$$

where E(x,t) is the excitation load per unit of length, and is defined as the sum of three terms, each of them participating on the modal sum as the model requires. These three terms include one distributed excitation force per unit length acting on the left span, one distributed excitation force per unit length acting on the right span, and one excitation point force acting on the cable. The acceleration of gravity due to the earth is g [m/s²]. The force at the damped support is define as

$$F_S(x,t) = \left[M_S\frac{\partial^2 y(x,t)}{\partial x^2} + C_S\frac{\partial y(x,t)}{\partial x} + K_S y(x,t)\right]_{x=d} \tag{2}$$

where M_S [kg] is the mass at the support, C_S [N s/m] is the damping at the support, and K_S [N/m] is the stiffness at the support.

The inclusion of damping considerably increases the difficulty of solving the differential equation of motion for the combined cable-support system. We wish to express the position of a point on the cable in terms of the mode shape and natural frequencies determined from an undamped system.

Using the separation of variables approach, we can write y (x,t) as the product of two functions X (x) which depends only space variable x, and Q(t) which depends only on the time variable t. A taut cable system model is altered by the addition of a mass and at the central support, which is referred to as a constrained structure.

The mode-summation method applied to a constrained structure will have the geometric coordinate vector {y (x,t)}, which is the product of the mode shape matrix [X(x)] and the generalized modal coordinate vector {Q (t)}.

The final solution for the position of the cable with time is given by a summation of the products of all eigenfunction solutions and all time-based functions. By using the constrained-structure approach, we can write our problem in matrix notation so that the position {y(x,t)} for each selected point along the span as a function of time variable becomes

$$\{y(x,t)\}_{Nx} = [X(x)]_{(Nx, Np)} \{Q(t)\}_{Np} \tag{3}$$

where Np is the number of eigenvalues $\{\lambda_{Np}\}$ computed using formulations defined by Teodoro(1994), where we find the necessary equations to compute the real roots. N_X is the number of subintervals in the span of length L.

Based on the matrix notation, and after rearranging terms Eqs. (1) can be rewritten as the eigenproblem

$$[M]\{\ddot{Q}(t)\} + [C]\{\dot{Q}(t)\} + [K]\{Q(t)\} = \{R(t)\} \tag{4}$$

where the dots indicate differentiation with respect to time, and the mass, damping, and stiffness matrices are defined by

$$[M] = \rho[X(x)]^T[X(x)] + M_s[X(x)]^T[X(d)] \tag{5}$$

$$[C] = c[X(x)]^T[X(x)] + C_s[X(x)]^T[X(d)] \tag{6}$$

$$[K] = \rho[X(x)]^T[X(x)][\Lambda] + K_s[X(x)]^T[X(d)] \tag{7}$$

where [X(d)] is a matrix with displacement of the support position only, and [Λ] is a diagonal matrix containing the real roots squared. The modal excitation force on the right-hand side of Equation (4) is given by

$$\{R(t)\} = [X(x)]^T\{E(x,t)\} - [X(x)]^T\{\rho g\} \tag{8}$$

The eigenproblem corresponding to Eq. (4) was solved using the QZ algorithm by Moler and Stewart (1973) for a generalized matrix eigenvalue problem. This method for the general case will give us a complex eigenvector matrix [U]. For each column of this matrix we have a complex eigenvalue that is an element of the diagonal matrix [Θ].

After some algebraic work we obtain the final solution for the generalized coordinate (time-based function). There will be three terms on this solution: the mode participation of load for each mode, the catenary shape of the cable due to the gravitational field, and the transient response which will die out due to the exponential decay caused by the system damping. Therefore, in order to investigate the effects of the inclusion of damping on the cable system, we consider only the mode participation term which is given by

$$
\left\{ \begin{array}{c} \{Q(t)\} \\ \\ \{\dot{Q}(t)\} \end{array} \right\} = [U]\left[\mathrm{diag}\!\left(\frac{1}{j\Omega - \theta_i}\right)\right][U]^{-1}\{h_E(t)\} \tag{9}
$$

where $j^2 = -1$ and $i = 1, \dots, Np$. $\{h_E\}$ is a vector dependent on the excitation load.

Transient Response When Left Span is Excited by a Point Load at the Midpoint

In the field, the actual power lines were excited manually by pulling on the cable near its midpoint in concert with the cable's response. This excitation process was simulated. This was accomplished by applying a point load at the midpoint of the left span (at $x=d/2$), this load had an excitation frequency equal to the natural frequency of the left span.

The initial conditions assumed were a displacement in the catenary shape and zero velocity. The point load was applied until a steady state of motion occurred. New initial conditions were obtained when the velocity had a maximum amplitude at the midpoint of the left span. The excitation force was set equal to zero at this time, and a transient solution was implemented with the new initial conditions of displacement and maximum velocity amplitude.

The computer program implemented the mathematical models described by Eq. 3, and Eq. 9. This program was used to calculate the responses at three selected locations: the midpoint of the left span $(x=d/2)$, the central support $(x=d)$, the middle of the right span $[x=d+(L-d)/2]$. The force transmitted to the structure at the central support $(x=d)$ was also calculated. These calculations were done for the physical parameters given in Table 1 and Table 2. These tables also show the types of natural frequency, the natural frequencies, and the modal damping.

Table 1   Damped Cable with Support and Both Ends Fixed - Natural Frequency and Damping Ratio $\tau_S = 7.0$

$$\rho = 1.302\,\mathrm{kg/m} \quad L = 404.774\,\mathrm{m}$$

$$T = 16,161.13\,\mathrm{N}$$

$$\zeta_C = 0.200 \quad \zeta_S = 0.080$$

$$v = 0.510 \quad \mu_S = 0.200$$

$$\omega_S = 0.259\,\mathrm{Hz}$$

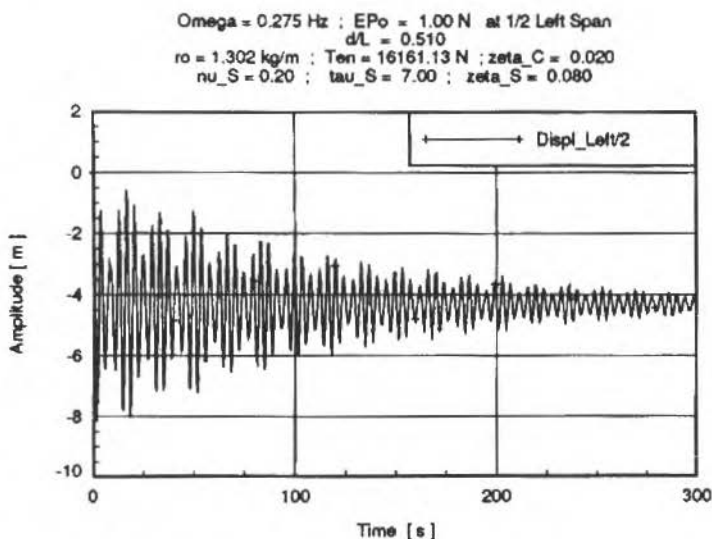| Index	Type	Frequency [Hz]	Damping Ratio [%]
1	support	0.242	0.5399
2	left	0.275	0.7498
3	right	0.301	0.4929
4	left	0.542	0.3880
5	right	0.564	0.3719
6	left	0.811	0.2600

Table 2   Damped Cable with Support and both Ends Fixed - Natural Frequency and Damping Ratio τ_S = 200.0

$$\rho = 1.302 kg/m \quad L = 404.774 m$$

$$T = 16, 161.13 N$$

$$\zeta_C = 0.200 \quad \zeta_S = 0.080$$

$$v = 0.510 \quad \mu_S = 0.200$$

$$\omega_S = 1.385 Hz$$

Index	Type	Frequency [Hz]	Damping Ratio [%]
1	left	0.270	0.7819
2	right	0.281	0.7510
3	left	0.541	0.3911
4	right	0.563	0.3757
5	left	0.810	0.2610
6	right	0.884	0.2509

A point load excitation of $EP_0 = 1.0 N$ was applied to the model at the midpoint of the left span ($x=d/2$) for a numerical simulation with an excitation frequency $\Omega = 1.(275) Hz$, which corresponds to the second cable system natural frequency (first natural frequency of the left-side span). The amplitude of motion at the midpoint of the left-side span is shown in Fig. 2. The corresponding displacement at the support point is show in Fig. 3 where the presence of an exponential decay and beating are evident. An exponential decay is present. As the higher frequency transients die out, and the cable reaches a steady state decay motion controlled by the fundamental frequency in approximately 300 seconds.

Fig. 2   Displacement at Midpoint of the Left-Side Span x = d/2 τ_S = 7.0 - Fixed Ends

Omega = 0.275 Hz ; EPo = 1.00 N at 1/2 Left Span
d/L = 0.510
ro = 1.302 kg/m ; Ten = 16161.13 N ; zeta_C = 0.020
nu_S = 0.20 ; tau_S = 7.00 ; zeta_S = 0.080
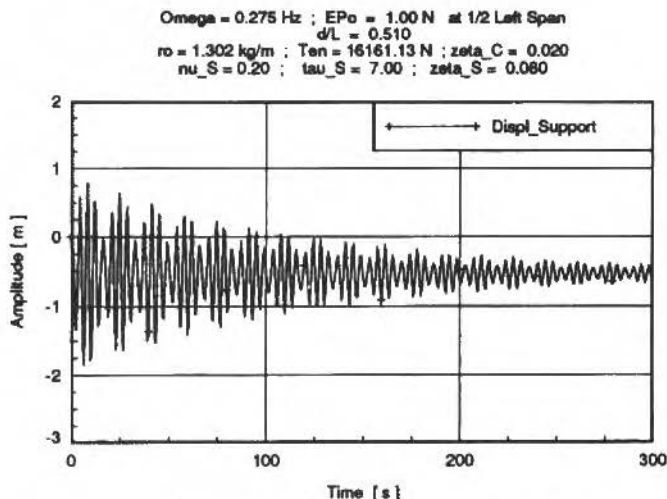
Fig. 3   Displacement at the Support Point -- τ_S = 7.0 - Fixed Ends

The force transmitted to the support tower is dependent on the support motion, the support-spring constant, the support damping, and the support velocity. The resulting force is shown in Fig. 4.

Omega = 0.275 Hz ; EPo = 1.00 N at 1/2 Left Span
d/L = 0.510
ro = 1.302 kg/m ; Ten = 16161.13 N ; zeta_C = 0.020
nu_S = 0.20 ; tau_S = 7.00 ; zeta_S = 0.080
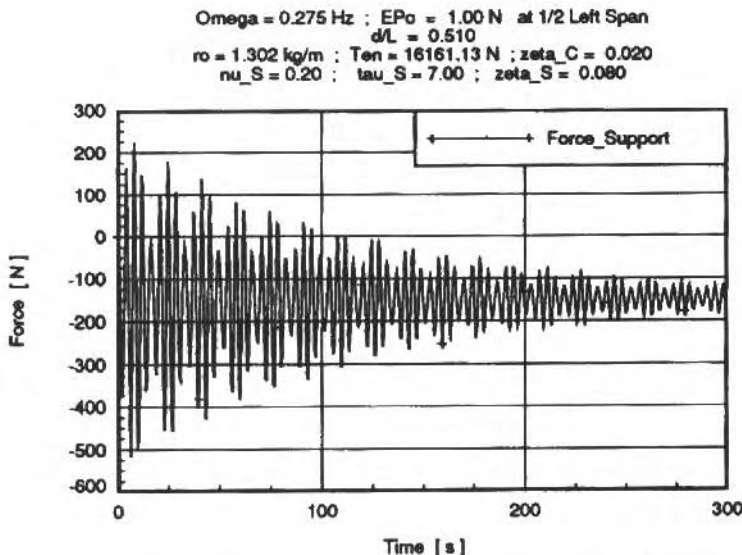
Fig. 4   Force Transmitted to the Tower by the Absorber System -- τ_S = 7.0 - Fixed Ends

For the case where all the other variables were kept constant and the spring-support ratio was increased to 200.0, the first six natural frequencies and their damping ratios are shown in Table 2. For this case, the support natural frequency has increased to 1.385Hz which is well above the cable's fundamental natural frequency. A comparison with Table 1 shows that while the left-span natural frequency decreased slightly, the right-span fundamental frequency had a larger decrease in value. The time response was once again simulated, with a different excitation frequency Ω = 0.270Hz, but still with the left-span natural frequency.

The displacement at the midpoint of the left-side span is shown in Fig. 5, where the exponential decay and a slight beating can be seen. With the amplitude of motion stabilizing around -3.75 in contrast to the amplitude of around -4.75 shown in Fig. 2, when the spring-support ratio was smaller.

Omega = 0.270 Hz ; EPo = 1.00 N at 1/2 Left Span
d/L = 0.510
ro = 1.302 kg/m ; Ten = 16161.13 N ; zeta_C = 0.020
nu_S = 0.20 ; tau_S = 200.00 ; zeta_S = 0.080
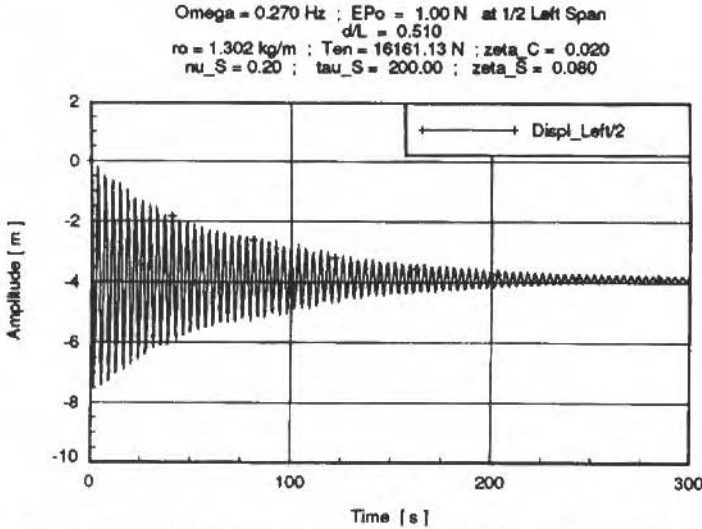
Fig. 5 Displacement at Midpoint of the Left-Side Span x = d/2 -- τ_S = 200.0 - Fixed Ends

The displacement at the support point is shown in Fig 6, where the presence of the beating is significant. This beating is caused by the small difference between the fundamental frequency of each left and right span.

Omega = 0.270 Hz ; EPo = 1.00 N at 1/2 Left Span
d/L = 0.510
ro = 1.302 kg/m ; Ten = 16161.13 N ; zeta_C = 0.020
nu_S = 0.20 ; tau_S = 200.00 ; zeta_S = 0.080
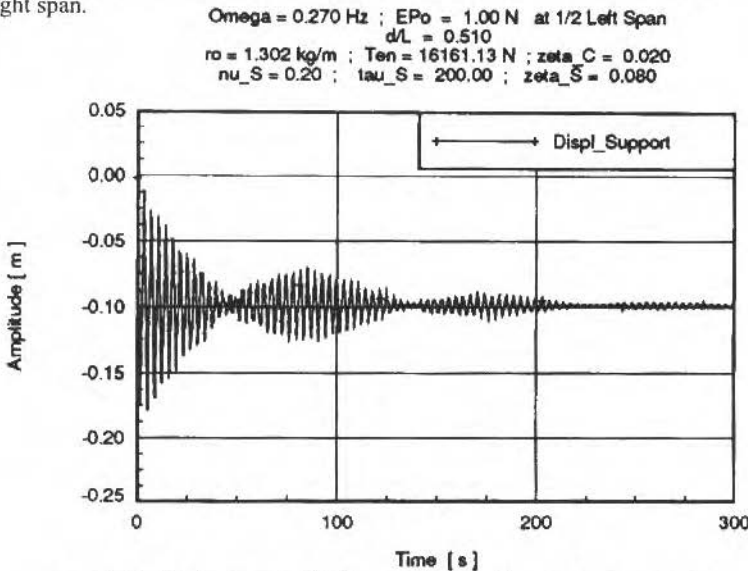
Fig. 6 Displacement at the Support Point -- τ_S = 200.0 - Fixed Ends

The force transmitted to the tower structure is shown in Fig. 7, where the average of the force magnitude has increased by a factor of 5 when compared to the force shown in Fig. 4. Although the displacement at the support has its average amplitude reduced by a factor of 5, the large value of the spring constant at the support result in a larger value for the force transmitted to the structure.

Conclusions

Introducing the compliant support into the cable system showed that is possible to reduce the cable motion uring the galloping phenomena.

The advanced model analysis indicated that energy absorber device reduced cable motion while reducing the forces transmitted to the supporting tower.

Omega = 0.270 Hz ; EPo = 1.00 N at 1/2 Left Span
d/L = 0.510
ro = 1.302 kg/m ; Ten = 16161.13 N ; zeta_C = 0.020
nu_S = 0.20 ; tau_S = 200.00 ; zeta_S = 0.080

Fig. 7   Force Transmitted to the Tower by the Absorber System -- τ_S = 200.0 - Fixed Ends

The mode-summation method was successfully applied to this class of problem, and the same type of behavior was observed from experimental measurements, using a prototype energy absorber installed in a 161kV near Jefferson-IA which supports the concept that energy absorber can introduce at least twice the apparent damping seen in the original system.

References

Cowper, G. R., Hrudey, T. M., and Lindberg, G. M., 1973, "The Oscillations of a Shallow Elastic Catenary", Nat. Res. Counc. Can. Tech. Rep. LTR-ST-657.
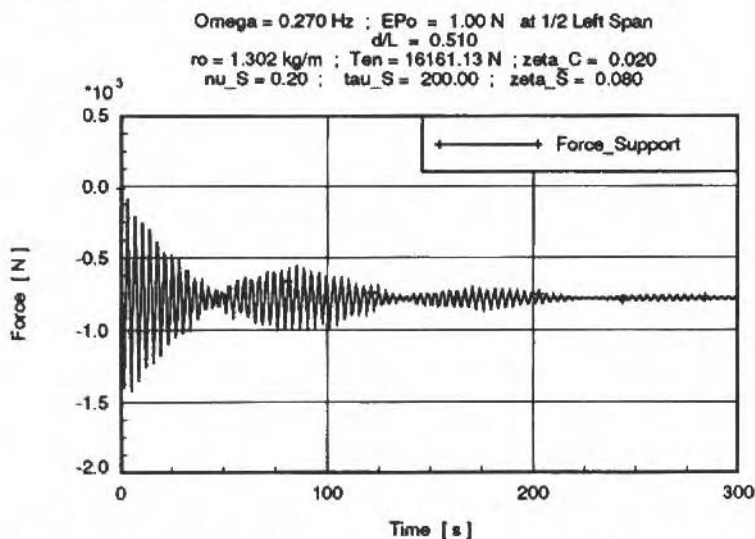
Dominguez, R. F., and Smith, C. E., 1972, "Dynamic Analysis of Cable Systems", J. Struct. Div. ASCE 98 (ST8), pp. 1817-1834.

Goodey, W. J., 1961, "On the Natural Modes and Frequencies of Suspended Chain", Q. J. Mech. Appl. Math. XIV (1), 118-127.

Irvine, H. M., and Caughey, T. K., 1974, "The Linear Theory of Free Vibration of a Suspended Cable", Proc. R. Soc. London, A341, pp. 299-315.

McConnell, K. G., and Zemke, W. P., 1980, "The Measurement of Flexural Stiffness of Multistranded Electrical Conductors While under Tension". Exp. Mech. June, 20 pp. 198-204

Moler, C. B., and Stewart, G. W., 1973, "An Algorithm for Generalized Matrix Eigenvalue Problems", SIAM Journal Numer. Anal. April, 10 (2), pp. 241-256.

Myerscough, C. J., 1973, "A Simple Model of Growth of Wind-Induced Oscillations in Overhead Lines", J. Sound Vib. 28 (4), pp. 699-713.

Nigol, O., and Buchan, P. G., 1981, "Conductor Galloping - Part 1, Den Hartog Mechanism", IEEE Trans. Power Appar. and Systems, 100(2), February, pp.708- 720.

Nigol, O., and Buchan, P. G. , 1981, "Conductor Galloping - Part 2, Torsional Machanism", IEEE Trans. Appar. and Systems, 100(2), February, pp. 708-720.

Pugsley, A. G., 1949, "On Natural Frequencies of Suspension Chains", Q. J. Mech. Appl. Math. v II (4), pp. 414-418.

Samras, R. K., Skop, R. A., and Milburn, D. A., 1974, "Analysis of Coupled Extensional-Torsional Oscillations in Wire Rope", Trans. ASME, J. Eng. Ind. 96, November, pp. 1130-1135.

Saxon, D. S., and Cahn, A. S., 1953, "Modes of vibration of a suspended chain", Q. J. Mech. Appl. Math. VI (3), 273-285.

Soler, A. I., 1970, "Dynamic Responses of Single Cables with Initial sag", J. Franklin Inst. 290 (4), October, pp. 377-387

Teodoro, E. B., 1994, Dynamics of a Power line when Supported by a Compliant Energy Absorber". Ph.D. Dissertation, Iowa State University, Ames.

West, H. H., Geschwindner, L. F., and Suhoshi, J. E., 1975, "Natural Vibrations of Suspension Cables", J. Struct. Div. ASCE 101 (ST11), November, pp. 2277-2291.

A Data Compression Method for the Modal Analysis of Spatially Dense Laser Vibrometer Measurements

José Roberto de França Arruda
Universidade Estadual de Campinas
Faculdade de Engenharia Mecânica
13083-970 Campinas, SP Brazil

Luiz Antônio S. B. Santos
Universidade Estadual de Campinas
Faculdade de Engenharia Elétrica
13083-970 Campinas, SP Brazil

Abstract

This paper investigates a method which can be used to compress two-dimensional velocity fields measured with the scanning LDV. The compressed data can be used as virtual measurements when estimating modal parameters. The data is compressed spatially using a two-dimensional Fourier series model. The approximation reduces and filters the measured data in the output space for each frequency line.
Keywords: Data Compression, Modal Analysis, LDV

Introduction

In modal tests using traditional transducers, the number of degrees of freedom measured on the structure under test usually ranges from tens to a few hundreds. Multiple Input / Multiple Output (MIMO) phase separation modal parameter estimation (MPE) algorithms (see, for instance, Allemang and Brown, 1987), such as the Least Squares Complex Exponential Method, the Eigensystem Realization Algorithm, and the Polyreference Orthogonal Polynomial Method, are commonly used to estimate the modal parameters from measured Frequency Response Functions (FRFs).

However, when spatially dense measurements are obtained with modern scanning Laser Doppler Vibrometers (LDVs), it is often impractical to use phase separation MPE methods due to the excessive amount of data (Sun et al., 1993). When the damping is small and the modes are well separated in the frequency domain, phase resonance tests or specially adapted frequency domain methods can be used (Arruda, 1993). Otherwise, some sort of condensation of the measured data is necessary to permit the use of the MIMO phase separation methods cited above.

As the number of modes interest is usually much smaller then the number of measured outputs, it is desirable to reduce the amount of spatial redundancy before the MPE algorithms are applied. The spatial condensation of measured data for modal analysis is a relatively new issue, which is becoming more relevant as the number of transducers used in modal testing increases and optical measurement techniques become more popular. Dippery et al. (1994) have proposed the linear combination of measured output into a smaller number of effective or virtual measurement stations. A constant, rectangular transformation matrix is used to condense the measured FRFs, organized in matrix form. This matrix is formed by juxtaposing the (N_0 x N_i) frequency response matrices measured at each frequency line, where N_0 is the number of outputs and N_i the number of inputs. The juxtaposition can be done either columnwise, yielding a matrix (N_0 x N_iN_s), or rowwise, yielding a matrix (N_0N_s x N_i), where N_s is the number of frequency lines. The transformation matrix is then obtained by the singular value decomposition (SVD) of this large matrix. It is simply the transpose of the U matrix of the SVD, truncated so that the first N_e singular vectors, associated with the most significant singular values, are retained.

The shortcomings of this condensation method are the computation effort involved in solving a large SVD problem and the fact that the estimation of the eigenvectors is still performed in the measurement space. Taking an example case, where 10,000 locations are measured (which is small in terms of the capability of a state-of-the-art LDV) at 400 frequency lines with 3 input references, the

matrix to be decomposed would be a complex, non-symmetric 10,000x1,200 matrix. Furthermore, the linear system of equations which must be solved in order to estimate the mode shape coefficients must be applied to 10,000 second members, i.e., a total of 10,000x1,200xN_m complex multiplications, where N_m is the number of estimated modes.

Therefore, the SVD-based condensation techniques are not suitable for spatially dense LDV measurements. This paper investigates an alternative method, which consists of approximating the data spatially using a two-dimensional Fourier series model referred to as the Regressive Discrete Fourier Series (RDFS) model (Arruda, 1992). It was shown (Arruda, 1992) that this techniques is applicable to both equally and non-equally spaced two-dimensional velocity fields measured with the scanning LDV. The approximation reduces and filters the measured data in the output space for each frequency line, thus generating a reduced set of data, which can also be interpreted as virtual measurements. The MPE procedure, both the eigenvalue and the eigenvector estimation, is performed upon the spatially reduced data. The expanded mode shapes can be reconstructed whenever necessary using the inverse RDFS.

To illustrate the proposed method, a set of FRFs was synthesized using spatially dense mode shapes measured with a scanning LDV using a phase resonance test. In this way, the exact modal parameters are known, and the method can be evaluated. A Polyreference Chebycheff Polynomial MPE method (Vold, 1990) was implemented and used to estimate the modal parameters from the condensed virtual measurements.

Spatial Domain Compression Using the RDFS

The data compression in the spatial domain can be done using a two-dimensional Fourier series, which takes advantage of the sinusoidal pattern of the mobility shapes of the structural surfaces sufficiently far from the boundaries. This is a well-known property of the wave equation solution for solids when the near-field effects are neglected.

For two-dimensional mobility shapes (Operational Deflection Shapes) mapped over a rectangular grid, say H_{mn}, one could think of using the two-dimensional Discrete Fourier Transform (DFT). The difficulty with using the DFT is that its implicit periodization introduces high-frequency components that account for the sharp edges present in the wrapped-around data. This phenomenon is known as leakage. In the data smoothing process, leakage is prejudicial, as it causes distortion of the low-pass filtered data. The usual way to reduce leakage is windowing, but this technique is not suitable in the case of finite length, spatial domain data. To overcome the leakage problem, the proposed technique consists of representing the data by a two-dimensional regressive discrete Fourier series (RDFS) proposed by Arruda (1992), which will be briefly reviewed here. Unlike the DFT, in the RDFS the original length of the data is not assumed to be equal to the signal period nor is the number of frequency lines assumed to be equal to the number of data points. With the two-dimensional, equally-spaced RDFS model, the mobility shape H_{mn} is expressed as:

$$H_{mn} = \sum_{k=-p}^{p} \sum_{l=-q}^{q} Z_{kl} W_M^{mk} W_N^{ln} + \varepsilon_{mn} \tag{1}$$

$$;m = 0, ..., M - 1; n = 0, ..., N - 1;$$

where H_{mn} represents the discretized data with constant spatial resolutions Δx and Δy, $W_M = \exp(i2\pi/M)$, $W_N = \exp(i2\pi/N)$, and ε_{mn} accounts for the noise and higher frequency contents of H. Note that $M \neq M$ and $N \neq N$. The length of the data in x is $M\Delta x$, but the period of the RDFS is $M\Delta x > M\Delta x$. The data reduction is achieved because $p \ll M$ due to the expected low ware number of the mobility shape surface. In the y direction $N\Delta x > N\Delta x$ and $q \ll N$. The $M \times N$ data in H are represented by a $(2p+1) \times (2q+1)$ complex matrix $\mathbf{Z}$ of elements Z_{kl}.

The RDFS is an approximation instead of an interpolation of H_{mn}. Thus, the Euler-Fourier coefficients cannot be calculated by the DFT. Rewriting Eq. (1) in matrix form:

$$H = W_M Z W_n + \varepsilon \tag{2}$$

The least-squares solution is given by:

$$Z = (W_M^H W_M)^{-1} W_M^H H W_N^H (W_N W_N^H)^{-1} \tag{3}$$

where the matrices to be inverted have a very small size, $(2p+1) \times (2p+1)$ and $(2q+1) \times (2q+1)$, respectively, and ^{H} denotes the matrix complex conjugate. The smoothed data $H^{(s)}$ may be obtained from:

$$H^{(s)} = W_M Z W_N \tag{4}$$

where W_M and W_N can be calculated for the desired spatial resolution. The reduction of the data is achieved as Z represents the data using only $(2p+1)(2q+1)$ values, instead of the original MN values. The formulation of the RDFS for non-equally spaced data given by Arruda (1992) can be used in the place of the formulation above when the mobility shapes are mapped over a non-regular, arbitrary grid.

Chebycheff Polynomial MPE Method

The Orthogonal Chebycheff polynomials MPE method (Vold, 1990) is applied to the compressed FRFs in matrices $Z(\omega)$. Therefore, instead of curve-fitting the large number of FRFs directly, the RDFS coefficients, taken as virtual measurement stations, are curve-fitted.

The RDFS coefficients are in fact linear combinations of the FRFs (see Eq. (1). Hence, the RDFS coefficients as a function of the frequency will have the same poles as the original FRFs. This allows us to write:

$$Z(\omega) = \frac{\sum_{k=0}^{r} a_k \phi_k(i\omega)}{\sum_{k=0}^{s} b_k \phi_k(i\omega)} \tag{5}$$

where ϕ_k is the kth Chebycheff polynomial, a_k is the kth polynomial matrix coefficient (of the same dimensions as Z), b_k is the kth denominator polynomial matrix coefficient, which is a scalar for single excitation, and $i = \sqrt{-1}$. Making, without loss of generality, $b_s = I$ one can write:

$$\sum_{k=0}^{s-1} Z(\omega)^H \phi_k^* b_k^H - \sum_{k=0}^{r} \phi_k^* I a_k^H = -\phi_s^* Z(\omega)^H \tag{6}$$

where I is the identity matrix and * denotes the complex conjugate of a scalar. Arranging Eq. (6) in matrix form for ω varying produces a linear system of equations which constitutes a least-squares problem, and can be easily solved for ak and bk.

It is important to mention that the frequency ω should be scaled so that the frequency range is always $[0,1]$. This improves the condition of the least squares problem.

Vold (1990) proposed that, instead of computing the corresponding power series polynomial coefficients to form the companion matrix, one could form a companion matrix problem in the orthogonal polynomial basis. The modified companion matrix can be formed by combining the characteristic equation, which in the case of multiple references is:

$$\left[\sum_{k=0}^{n} [b_k] \phi_k(i\omega) \right] \{V\} = \{0\} \tag{7}$$

with the formula to generate the orthogonal Chebycheff polynomials:

$$\phi_m (i\omega) \{V\} = 2s\phi_{m-1} (i\omega) \{V\} - \phi_{m-2} (i\omega) \{V\} \tag{8}$$

Solving the combined eigensystem of equations formed in the usual way, a companion matrix is formed, and the eigenvalues S_r, $r=1, ..., nN_i$ **** are obtained. The first N_i elements of the eigenvectors V_r are the modal participation vectors L_r of the partial fraction expression of $Z(\omega)$:

$$[Z(\omega)] = \sum_{r=1}^{N} \{\varphi_r\} \left(\frac{L_r^T}{i\omega - s_r} \right) + \{\varphi_r^*\} \left(\frac{L_r^H}{i\omega - S_r^*} \right) \tag{9}$$

where $N = nN_i$ and $\{\varphi_r\}$ are the mode shapes. It should be noted that the eigenvectors and the modal participation vectors are in the compressed RDFS space.

Once the modal participation vectors and the eigenvalues are known, computing the eigenvectors is straightforward. Equation (9) can be rearranged for each element (o) of matrix $Z(\omega)$ to yield:

$$H_0 = \Psi_0 B^T \tag{10}$$

where:

$$B = \begin{bmatrix} LW_1 \\ LW_2 \\ \cdot \\ \cdot \\ \cdot \\ LW_m \end{bmatrix}; \quad L = [L_1 \ L_2 \ ... \ L_{2N}];$$

$$W_i = \text{diag} [i\omega_i - s_1 \quad i\omega_i - s_2 \quad ... \quad i\omega_i - s_{2N}]^{-1}$$

where m is the number of frequency lines.

Solving the linear system of equations in Eq. (10) for each elements of matrix $Z(\omega)$ yields the mode shapes in the compressed RDFS space. The mode shapes in the measurement space can be computed with Eq. (4).

Results

A prototype software was developed to verify the proposed formulation. The algorithm may be summarized as follows:

1. Apply a robust data smoothing technique to eliminate outliers from measured mobility shapes.

2. Apply the RDFS to each mobility shape.

3. Curve-fit the RDFS coefficients as functions of the frequency (using them as virtual measurement stations).

4. Obtain the polynomial coefficient matrices a_k and b_k, which form the reduced model.

5. Build a companion matrix with the computed polynomial coefficients and extract the eigenvalues and eingenvectors of the structure.

6. Expand the mode shapes whenever necessary with the inverse RDFS.

In order to illustrate the use of the proposed space-frequency data compression method, a hybrid numerical-experimental simulation of a free-free-free-free rectangular aluminum plate was used. The plate, which is 425.45x457.20x3.17 mm, was hung from tiny holes in its corners using fish lines and was excited sinusoidaly using a shaker. The response was measured with a scanning LDV. The phase resonance condition was sought for each mode by varying the excitation frequency and observing the phase between the excitation signal and the measured velocities. The natural frequencies and mode shapes of the first 10 modes were measured using the methodology described by Sun et al. (1993). The mobility shapes were numerically simulated using the formulation of the FRFs for a proportionally-damped structure:

$$H_{ij}(\omega) = \sum_{r=1}^{S} \frac{\psi_{ir}\psi_{jr}}{\omega_r^2 - \omega^2 + i2\xi\omega\omega_r},$$ (11)

where φ_{ir} is the ith element of the rth mode shape vector. The excitation station was kept constant at one of the plate corners, $j=1$, while the measurement stations varied, $i=1$, MN. The same modal damping factor $\xi = 0.01$ was used for all the modes. For each frequency ω, the elements of the vector $H_{ij}=1$; $i=1$, MN, where arranged in matrix form following the mapping which was used when measuring the mode shapes with the LDV, thus producing a mobility shape H_{mn}; $m=0$, M-1; $n=0$, N-1. The simulated FRFs are unscaled; each mode shape was normalized to unitary amplitude.

The proposed methodology was used to estimate the 5 modes in the frequency range 200-300 Hz (modes 6-10) using a 1 Hz frequency resolution. Table 1 shows the estimated undamped natural frequencies and modal damping coefficients compared to the exact values. In this noise-free case the result is, as expected, nearly exact. The data compression using the RDFS did not introduce any noticeable error. Table 1 also shows the correlation coefficients, known as Modal Assurance Criterion (MAC), between the estimated mode shapes and the exact mode shapes. Again the results are very good. It should be noted that the estimated mode shapes represent a smoothed version of the modes used in the simulation, which are contaminated with measurement noise. Figure 1 shows a graphical comparison of exact and estimated mode shapes.

Table 1   Modal Parameter Estimation Results

mode	natural freq. [Hz]		damping coef [%]		MAC
	exact	estimated	exact	estimated	
6	211.500	211.682	1	0.99	0,9996
7	237.180	237.244	1	0.99	0.9998
8	245.670	245.724	1	0.99	0.9991
9	249.770	299.820	1	0.99	0.9982
10	290.550	290.582	1	0.99	0.9989

Conclusions

A spatial domain data compression method which makes the use of phase-separation, global modal parameter estimation methods viable when treating spatially dense LDV measurements was proposed. The method takes advantage of the sinusoidal spatial character of structural vibration, as it curve fits a spatial Fourier series to the measured velocities. The regressive approach permits the approximation of two-dimensional velocity fields measured over non-equally-spaced grids and can be extended to treat arbitrary, non-rectangular grids. Besides, it avoids the leakage problems of the DFT without windowing the short length spatial data.

(a)

(f)

(b)

(g)

(c)

(h)

(d)

(i)

(e)

(j)
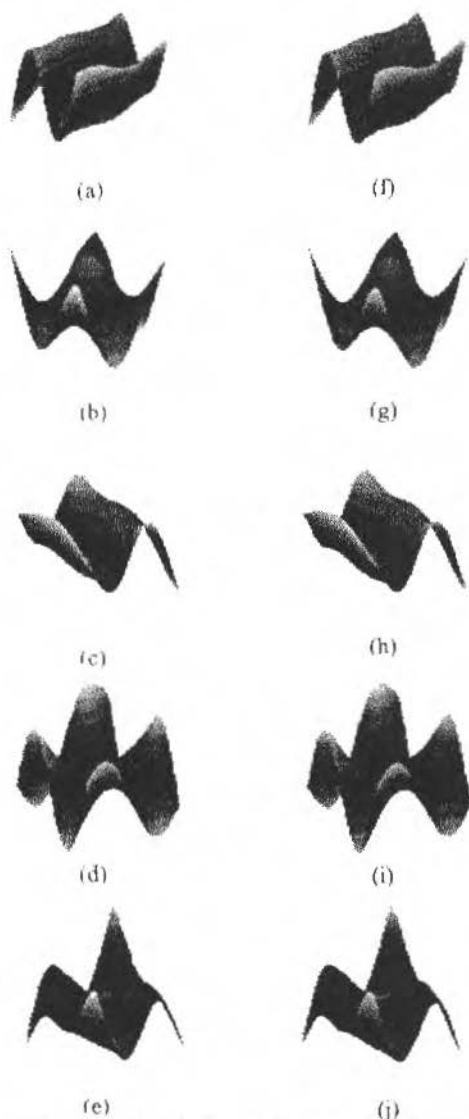
Fig. 1   Comparison of Exact and Estimated Mode Shape (6 -10). (a - e) Exact Modes; (f-j) Estimated Modes

A modified Chebycheff orthogonal polynomial polyreference method proposed by Vold (1990) was used. The method is particularly suitable for this application because it estimates parameters in the frequency domain with arbitrary frequency spacing, which is frequently the case with LDV measurements. The frequency lines where the mobility operating shapes are measured can be chosen in the neighborhood of the resonances, where the measurements are richer in terms of modal information. The method is applied to spatially compressed data, thus saving computation effort and memory space. The results can be stored in the compressed format, and expanded whenever necessary.

The proposed method was validated using a hybrid experimental-numerical example where the mode shapes were obtained experimentally using a LDV and the mobility operating shapes were simulated using the experimental modes.

Acknowledgments

References

Allemang, R. J., and Brown, D. L., 1987, "Modal Parameter Estimation," in: Experimental Modal Analysis and Dynamic Component Synthesis, AFWAL-TR-87-3069, Vol. III, Air Force Wright Aeronautical Labs., Ohio, USA.

Arruda, J. R. F., 1992, "Surface Smoothing and Partial Spatial Derivatives Computation Using a Regressive Discrete Fourier Series," Mechanical Systems and Signal Processing, Vol. 6, No. 1, pp. 41-50.

Arruda, J. R. F.,1993, "Spatial Domain Modal Analysis of Lightly-Damped Structures Using Laser Velocimeters," Journal of Vibration and Acoustics, Vol. 115, No. 3, pp. 225-231.

Arruda, J. R. F., Rio, S. A. V., and Santos. L. A. B., "A Space-Frequency Data Compression Method for Spatially Dense Laser Doppler Vibrometer Measurements," Shock and Vibration, to appear.

Dippery, K. D., Phillips, A. W., and Allemang, R. J., 1994, "Condensation of the Spatial Domain in Modal Parameter Estimation," Proc. of the 12th Int. Modal Analysis Conference, Honolulu, Hawaii, USA., January 31 - February 3, pp. 818-824.

Sun, F., Mitchell, L. D., and Arruda, J. R. F., 1993, "Mode Decoupling Considerations in Mode Shape Measurements of a Plate With Monoexcitation and Laser Doppler Vibrometer," Experimental Techniques," Vol. 17, No. 4, pp. 31-37.

Vold, H., 1990, "Numerically Robust Frequency Domain Modal Parameter Estimation," Sound and Vibration, January, pp. 38-40.

Estudo do Recalque Isotérmico de Anéis e Cilindros Pelo Método dos Elementos Finitos

Cylinders and Rings Hot Upset Forging Analysis by the Finite - Element Method

Evandro Cardozo da Silva
Sérgio Tonini Button
Universidade Estadual de Campinas
Faculdade de Engenharia Mecânica
Departamento de Engenharia de Materiais
13083-970 Campinas, SP Brasil

Abstract

The state of the art in forging points to precision forging. The modern competitive forging industry uses computational systems to plan it, instead of the conventional trial and error methods. Based on this tecnology, this work develop a bidimensional finite element mathematical model of rigid-viscoplastic analysis of cylinders and rings hot upsetting, and the code validated by comparing simulation with the upper bound method and experimental results. Theoretical calibration curves used to define friction in the ring test were provided with simulations by the finite element method (FEMME).

Keywords: Forging, Hot Upsetting, Finite Element Method, Cylinders, Rings

Resumo

O estado da arte, no forjamento, aponta para o forjamento de precisão. O seu projeto através do método tradicional de tentativa de erro cede lugar ao uso de sistemas computacionais na indústria de forjados competitiva atual. Com base nesta tecnologia é desenvolvido neste trabalho um modelo matemático bidimensional de elementos finitos de análise rígido-viscoplática para o recalque simples de cilindros e anéis, sendo o código validado por comparação da simulação com o método do limite superior e resultados experimentais. As simulações pelo método de elementos finitos resultara nas curvas de calibração teóricas usadas na avaliação de atrito pelo teste de anel.

Palavras-chave: Forjamento, Recalque Simples, Cilindros, Anéis, Método dos Elementos Finitos

Introdução

O forjamento de precisão tem por meta a produção de forjados com uma qualidade de acabamento que reduza, em parte ou integralmente, as operações secundárias de acabamento. Para atingir este objetivo o projeto de uma peça forjada exige o abandono do método tradicional de tentativa e erro (Lowe, 1988). O uso de sistemas computacionais passa a ser a ferramenta essencial para conduzir a indústria de forjados a se adaptar a novos requisitos tecnológicos para assegurar custos competitivos nos diferentes mercados.

Para o recalque simples de cilindros e anéis é desenvolvido neste trabalho um modelo matemático bidimensional de elementos finitos de análise rígido-viscoplástica, cuja tecnologia é a base para o aprimoramento e implantação do processo de forjamento de precisão.

O código do modelo matemático em linguagem FORTRAN 77 tem sua validade verificada por comparação da simulação usando elementos finitos quadrilaterais linear e quadrático com método do limite superior e resultados experimentais.

Foram verificadas as influências sobre as simulações, do emprego de materiais de importância tecnológica distintos, de fatores de atrito diversos, de várias velocidades de processo e outros parâmetros preponderantes. Sendo assumido o estado plano de deformação o modelo adotado mostrou-se adequado para análise do recalque de cilindros e anéis fornecendo resultados compatíveis com as observações experimentais e as informações encontradas na literatura.

Usando o método de elementos finitos simulou-se a variação dos diâmetros internos de anéis com as proporções geométricas convencionais e   indicadas por gráficos para vários fatores de atrito (m) na

interface peça-matriz. Este procedimento é a maneira convencional de representar curvas de calibração teóricas usadas na avaliação de atrito com o teste de anel.

Simulação do Processo de Forjamento

O modelo matemático dos processos de conformação de metais tem por objetivo fornecer informações que possibilitam o correto projeto e controle desses processos. Para tanto o método de análise deve ser capaz de determinar os efeitos de vários parâmetros sobre as características de escoamento dos materiais. Além disso, a eficiência computacional, tanto quanto a solução exata, é uma importante consideração para o método ser útil na análise de problemas de conformação de materiais. Sendo atualmente crescente na indústria a necessidade de códigos computacionais econômicos, fáceis e confiáveis para modelar processos de conformação. Com este enfoque, o método de elementos finitos rígido-plástico (ou rígido-viscoplástico) tem sido o de maior sucesso na análise de uma série de problemas de conformação de metais.

O método de elementos finitos (MEF) rígido plástico que foi desenvolvido por Lee e Kobayashi (Oh, 1982), sendo aplicado na análise de vários problemas tais como recalque de cilindro sólido, compressão de anel, extrusão e dobramento de chapas. O método tem sido também aplicado com sucesso na previsão de formação de defeitos no recalque e extrusão (Gunasekera et al., 1982), e a medição do atrito peça-matriz. Foi estendido para material rígido-viscoplástico por Oh (1982) e aplicado para recalque e compressão de anel no campo de trabalho a quente, cuja formulação é descrita em trabalho anterior (Silva et al. 1993) e encontrada detalhada na literatura (Kobayashi et al., 1989; Zienkiewicz e Taylor, 1991).

Resultados Numéricos e Validação Experimental

Os resultados da simulação do método de aproximação adotado (MEF) são comparados com os resultados experimentais do recalque de cilindros e anéis. Ensaios experimentais foram realizados no laboratório de conformação mecânica da UNICAMP (Silva, 1995) com o mesmo material simulado.

Neste trabalho, os elementos linear e quadrático foram implementados e aplicados na análise do recalque a quente de cilindros e anéis entre matrizes planas. Os resultados numéricos do modelo de elementos finitos desenvolvido, são comparados com alguns trabalhos encontrados na literatura (Lee e Altan, 1972; Price e Alexander, 1976; e Kobayashi et al., 1989).

Compressão de Cilindros. A deformação é não homogênea na compressão de cilindros sólidos com atrito na interface peça-matriz. Portanto a superfície livre embarrila ou sofre dobramento ("folding").

A forma do barrilamento é influenciada pelas condições de atrito e pela geometria da peça. A geometria é representada pelas razões de altura por diâmetro, pequena (menor que 1,6) e grande, resultado num barrilamento simples e duplo, respectivamente (Price e Alexander, 1976). Este fenômeno é visualizado na Fig. 1 pela representação gráfica da malha distorcida da simulação da compressão de tarugos de grandes razões de altura-diâmetro equivalentes aos trabalhos de Kobayashi et al., (1989).

Condições Computacionais e Procedimentos. A análise do forjamento de compressão de cilindros isotérmica foi realizada para dois atritos diferentes. Os atritos usados na análise são m=0,3 (condição de lubrificação) e m=0,6 (sem lubrificação) (Oh, 1982).

O tarugo cilíndrico indeformado tem as dimensões de 25,4 mm (1 pol.) em altura e 50,8 mm (2 pol.) em diâmetro. O material usado na análise é titânio Ti-6Al-4V a 900 ** . A relação tensão-taxa de deformação é obtida da literatura (Schey, 1987) (C=140, m=0,4). A velocidade da matriz superior usada na análise foi de 24,5 mm/s (1 pol./s) e a matriz inferior é estacionária.
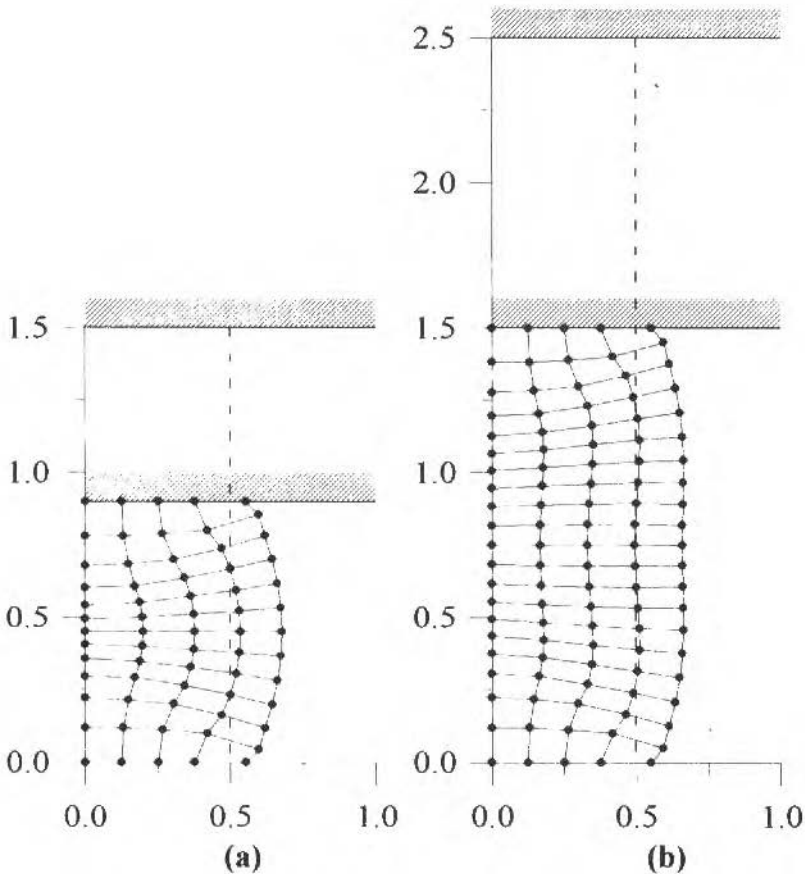
Fig. 1   Malha Distorcida Indicando a Influência da Geometria da Peça Sobre a
Forma do Barrilamento: (a) Ho/Do = 1,5 e (b) Ho/Do = 2,5, para 40% de Redução na Altura

Resultados e discussões. A Fig. 2 mostra uma malha MEF indeformada usada para a análise e as malhas distorcidas calculadas com deslocamento da matriz de 0,4 Ho. A malha é construída de 36 elementos lineares (ou 9 elementos quadráticos) o que corresponde a 49 nós. Para melhor comparação, as distorções da malha para ambos os casos de atrito são superpostas. Como pode ser observado na Fig. 2 (b), com o processo de deformação o barrilamento da superfície livre se forma. Ocorre o dobramento ("folding") da superfície lateral para a matriz superior e inferior simetricamente de forma mais acentuada para o atrito elevado. Ao longo do processo de recalque do material é grande a deformação na região central e na interface peça-matriz, como pode ser observado das distorções das malhas para o maior atrito.

As simulações são comparadas com as medições experimentais das seções transversais de cilindros. Estas foram obtidas por Leal et al., (1992), que realizou ensaios de compressão a frio e a quente de alumínio recozido. Esses dados foram selecionados para uma avaliação inicial do presente MEF por estarem disponíveis. Sendo o alumínio um material dependente da taxa de deformação, espera-se simular o escoamento de outros materiais com a mesma característica.
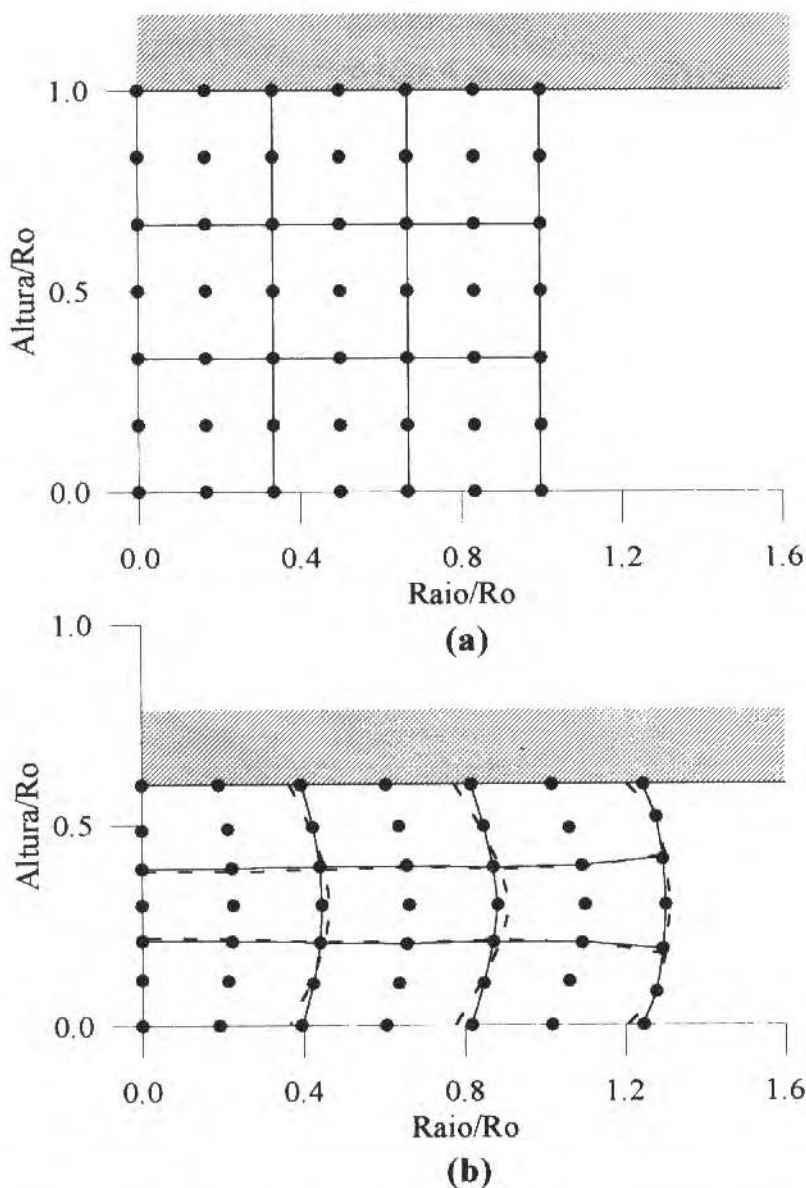
Fig. 2 Distorções da Malha para as Simulações do MEF a Deslocamento da Matriz de (a) 0,0 Ho e (b) 0,4 Ho. As Linhas Cheias são para m=0,3 e as Linhas Tracejadas para m=0,6. As Unidades são Múltiplas do Raio Indeformado

A simulação com m=0,6 é comparada com o caso sem lubrificação para uma redução de 46,9% na redução da altura do cilindro na Fig. 3. Esta figura mostra que o resultado da simulação está em boa concordância com o experimento.

Como o alumínio forjado isotermicamente se comporta de forma semelhante ao chumbo forjado a temperatura ambiente (Oh, 1982), podemos para a nossa análise substituir o chumbo da literatura pelo alumínio.
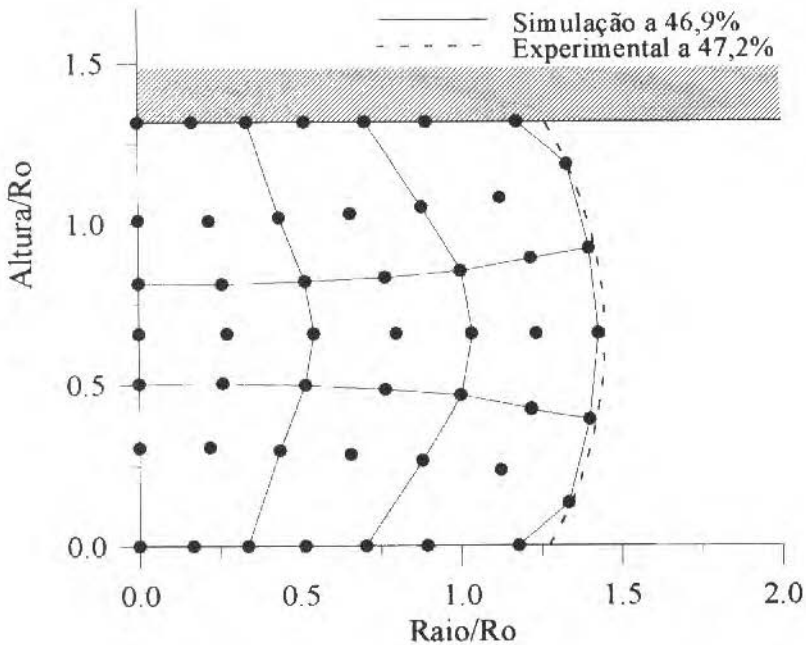

Fig. 3   Seção Transversal Simulada Comparada com o Experimento para uma Redução de 47,2% na Altura do Cilindro. Simulação: Ti-6A1-4V, 900°C, m=0,6. Experimental: Alumínio Comercialmente Puro, a 400°C, a Seco

Compressão de Anéis. Na Fig. 4 podemos identificar facilmente o comportamento do escoamento do metal em função do atrito na compressão de anéis. Esta solução para a simulação valida na formulação adotada pois se encontra largamente comprovada na literatura (Lee e Altan., 1972), Kobayashi et al, 1989, Zienkiewicz e Taylor, 1991).

Condições Computacionais e Procedimentos. A realização da simulação do recalque de anel segue os mesmos parâmetros do recalque de cilindro de titânio (Fig. 2), com exceção da geometria que possui uma relação (6:3:2) 3 pol (76,2 mm) D.E. x 1,5 pol (38,1 mm) D.I. x 1 pol (25,4 mm) altura, normalmente usada para anéis. Estas condições revelam os resultados obtidos para anéis de titânio Ti-6A1-4V a 900°C.

Resultados e Discussões. A simulação com m=0,6 é comparada com o caso sem lubrificação para uma redução de 38,4% na altura do anel na Fig. 5. observa-se uma boa concordância do resultado da simulação com o experimental medido do perfil da seção transversal do anel, comprimido a quente isotermicamente.
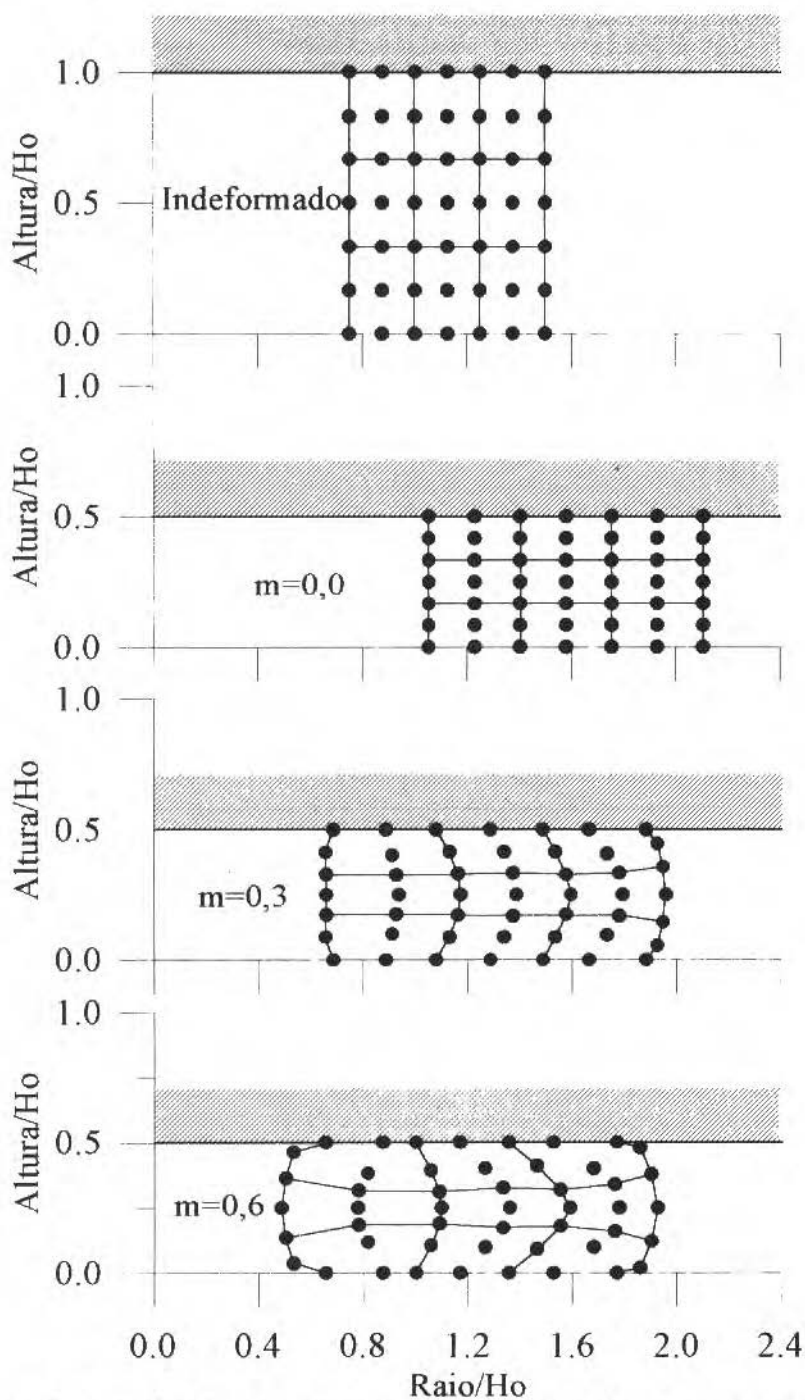
Fig. 4 Distorções da Malha nas Simulações do MEF da Compressão de um Anel para os Fatores de Atrito m=0, 0,3 e 0,6. As Unidades são Múltiplas da Altura Indeformado
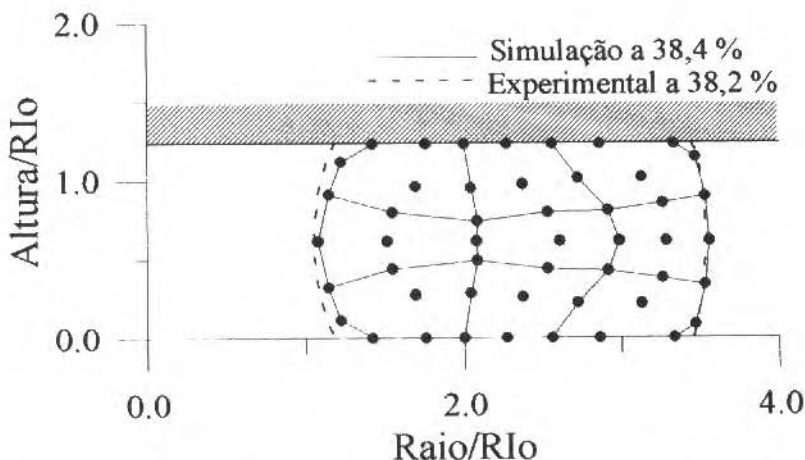
Fig. 5   SeçãoTransversal Simulada Comparada com o Experimento para uma Redução de 38,4% na Altura do Cilindro. Simulação: Ti-6A1-4V, 900°C, m=0,6. Experimental: Alumínio Comercialmente Puro, a 350°C, a Seco

O Teste de Anel

Noções Básicas. O fator de atrito, m, no forjamento é comumente medido realizando o teste de compressão de anel. A forma e característica do teste foram descritas em trabalho anterior (Silva, 1995). Observa-se que a variação que ocorre no diâmetro interno do anel durante a compressão é uma boa indicação das condições de atrito na interface peça-matriz. O teste de compressão de anel para determinar o fator de atrito é fácil de ser realizado, e a técnica exige somente a medição do diâmetro interno do anel forjado. Podendo ser aplicado sob diferentes condições, o que possibilita a avaliação do atrito na interface para vários lubrificantes sob condições de produção reais ou próximas das reais.

Análise de Deformação na Compressão de Anéis. O valor do atrito na interface é obtido pela comparação dos valores teóricos e experimentais do diâmetro interno do anel comprimido. Para tanto, uma análise baseada no método de elementos finitos rígido-viscoplástico adotado é comparada com o experimento.

Neste modelo foram consideradas as variações locais na tensão de escoamento e deformação. Para análise pretendida, o programa de computador desenvolvido permite simular o teste de compressão de anel para prever a mudança no diâmetro inicial e os perfis de barrilamento da superfície livre. As simulações comparadas com os experimentos, conduzidos com anéis de alumínio 1100 recozido, foram em geral de boa concordância exceto para atritos muito altos (Lee e Altan, 1972) (método do limite superior).

Aplicações do Teste de Anel para Determinar o Fator de Atrito. Através da simulação determinam-se as dimensões do anel para várias reduções na altura e diferentes fatores de atrito. Estes resultados são representados graficamente pelas assim denominadas "curvas de calibração", traçando o percentual de variação do mínimo diâmetro interno em função da redução percentual da altura do anel para vários fatores de atrito m. Os gráficos para uma mesma geometria de anel (Diâmetro Externo: Diâmetro Interno: Altura) de 6:3:2, são mostrados na Fig. 6.

As condições experimentais e verdadeiras de forjamento de anéis devem ser semelhantes para determinar o fator de atrito na interface peça-matriz. Seguindo a mesma relação DE: DI: Altura usada na curva de calibração (Fig. 6) o teste é conduzido para várias reduções de altura pré-determinadas lubrificando-se o anel ou a matriz, ou ambos, com o lubrificante em estudo. A altura final e o diâmetro mínimo do furo no barrilamento interno são medidos cuidadosamente para cada redução e os valores adequadamente representados na curva de calibração equivalente. O fator de atrito, m, corresponde à condição na interface é então estimado comparando a curva experimental resultante com as teóricas de calibração. Este procedimento é ilustrado na Fig. 6. Anéis de alumínio (DE 18 mm x DI 9 mm x Altura

6 mm) são forjados a quente para aproximadamente 10, 20, 30 e 40% de sua altura original sem lubrificação (seco). Observa-se que o fator de atrito, m, é aproximadamente 1,0 para a condição a seco. Para cada geometria inicial da amostra diferente da vista (6:3:2), usada no experimento de forjamento de anel, corresponde uma nova montagem de curvas de calibração.

O mesmo procedimento é observado no trabalho de Lee e Altan(1972) sendo os resultados comparativos de sua simulação e deste trabalho com o experimento por ele levantado representado na Fig. 6. Observa-se uma sensível melhora nos resultados teóricos obtidos pelo MEF em relação ao método do limite superior na comparação com o experimento para grandes deformações.
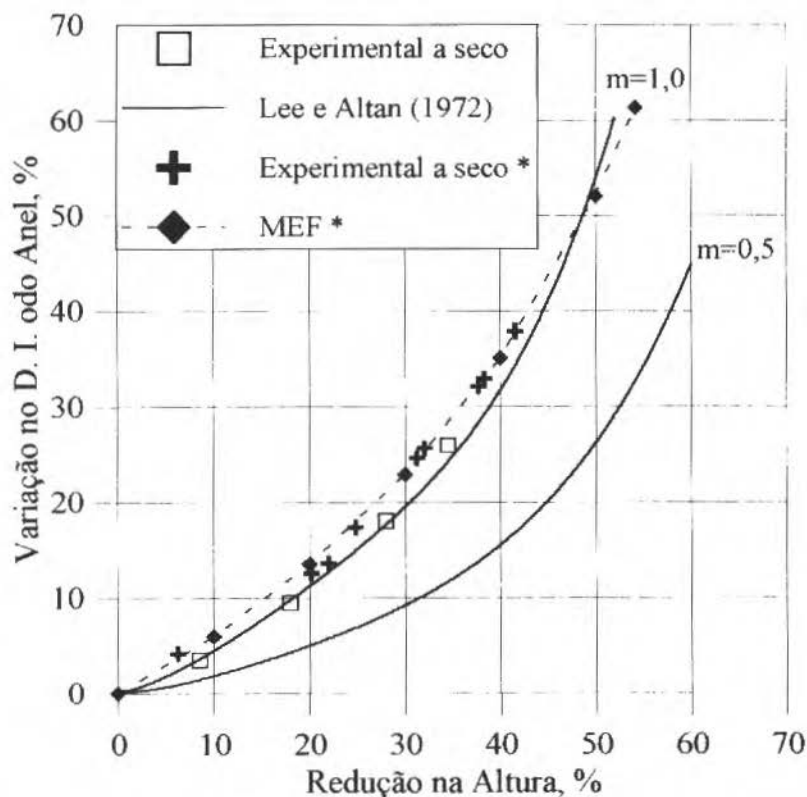

Fig. 6　Curvas de Calibração Teóricas usadas para um Anel com a Relação 6:3:2 e Resultados Experimentais para Forjamento de Anéis para duas Condições de Atrito. O * se refere aos Resultados do Presente Trabalho

Conclusões

A aproximação de elementos finitos para materiais rígido-viscopláticos tratando-os como fluidos viscosos não-Newtonianos é proposta. Para tanto foi desenvolvido um programa de computador para similar o teste de anel e o forjamento de recalque de um cilindro para prever o perfil de barrilamento e durante o recalque e determinar as curvas de calibração no recalque de anéis para avaliar o fator de atrito m de um teste de anel. Este programa pode ser usado para amostras de diversas dimensões e materiais.

Com o presente método (MEF) comprovou-se que a forma de barrilamento, no estudo do barrilamento no recalque de cilindros, é influenciada pela razão altura-diâmetro inicial e pelas condições de atrito.

No recalque de anéis verificou-se que o diâmetro interno aumenta no caso de baixo atrito e decresce no caso de alto atrito. Esta dependência no comportamento do escoamento do metal no atrito é extensivamente usada no teste de lubrificantes, condições de lubrificação, e para determinar o fator de atrito na interface.

Agradecimentos

Referências

Gunasekera, J. S., Gegel, H. L., Malas, J. C., Doraivelu, S. M., e Morgan, J. T., 1982, "Computer-Aided Processes Modelling of Hot Forging and Extrusion of Aluminium Alloys", Annals of CIRP, Vol. 31, pp. 131-144.

Kobayashi, S., Oh, S. I., e Altan, T., 1989, "Metal Forming and the Finite-Element Method", Oxford University Press, Inc.

Leal, C. V. G., e Button, S. T., 1992, "Qualificação de Produtos Obtidos pelo Processo de Forjamento de Precisão", Relatório Parcial de Pesquisa do Programa PIBIC CNPq/UNICAMP, DEMa - FEM - UNICAMP.

Lee, C. H., e Altan, T., 1972, "Influence of Flow Stress and Friction Upon Metal Flow in Upset Forging of Rings and Cylinders", Journal of Engineering for Industry, August, pp. 775 -782.

Lowe, T. C., 1988, "Computer Simulation of Deformation Processing", Journal of Metals, Vol. 40, No. 4, pp. 6-11.

Oh, S. I., 1982, "Finite Element Analysis of Metal Forming Processes with Arbitrarily Shaped Dies", International Journal of Mechanical Science, Vol. 24, No. 8, pp. 479-493.

Price, J. W. H., e Alexander, J. M., 1976, "A Study of Isothermal Forming or Creep Forming of Titanium Alloy", 4th North American Metalworking Research Conference Proceedings, pp. 46-53.

Schey, J. A., 1987, "Introduction to Menufacturing Processes", Second Edition, McGraw Hill.

Silva, E. C., Lima, Felipe A. A., e Button, S. T., 1993, "Simulação do Recalque a Quente pelo Método de Elementos Finitos", Anais do XII Congresso Brasileiro de Engenharia Mecânica, Vol. II, Brasília, Brasil, pp. 1611-1614.

Silva, E. C., 1995, "Estudo do Processo Isotérmico de Forjamento de Precisão através do Método de Elementos Finitos", Tese de mestrado, Universidade Estadual de Campinas, SP, Brasil.

Zienkiewicz, O. C., e Taylor, R. L., 1991, "The Finite Element Method - Vol. 2 Solid and Fluid Mechanics Dynamics and Non-linearity", Vol. II. McGraw Hill.

Model of Brittle Materials Single Point Machining With High Removal Rates

Jaime Gilberto Duduch
Arthur José Vieira Porto
Renato Goulart Jasinevicius
Universidade de São Paulo
Escola de Engenharia de São Carlos
Departamento de Engenharia Mecânica
São Carlos, SP Brazil

Anthony E. Gee
Cranfield University

Abstract

Diamond turning and form-grinding are viable options for manufacturing optical surfaces with adequate surface finish for use in infra-red and forseeably in visual light applications, both spherical and aspherical, without the need for post-machining finish. This restrict ductile-regime (plastic removal of material) diamond turning requires that no cut should exceed the so called critical depth or thickness producing crack-free grooves. However, very low material removal rates are obtained. This work proposes a model in which a greater part of the material may be removed through brittle microfracture whilst a surface and sub-surface can be obtained with low damage levels.
Keywords: Single Point Machining, Brittle Materials, High Removal Rate

Introduction

Requirements for optical glasses, ceramics and crystalline semiconductors each call for the forming of brittle materials with low damage (McKeown, 1986). As a result, there is an increasing interest in the machining of brittle materials, especially in the electronic and optical industries (McKeown, 1990; Puttick et al., 1989; Smith, 1990). Brittle materials are susceptible to surface and sub-surface damage due to local stress concentrations when contact is made with sharp and hard objects such as tools or grits during machining or indentation. Examples of such materials in common use in industry are silicon (Tönshoff et al., 1990), germanium, optical glasses, sapphire and fine ceramics recently developed as structural, functional and biological materials in high performance applications such as electronic and optical devices and heat and wear resistant parts, e.g., silicon nitride and silicon carbide (Puttick and Franks, 1990). To meet the increasing demand for such components, high efficiency machining techniques are needed, characterized by low inherent forces and low damage.

Brittle materials are used for their superior properties and ability to take a polish. However, brittleness affects their machinability, so that machined surfaces of brittle materials have previously been characterized by considerable sub-surface damage. This damage can be normally removed by lapping and polishing or etching (Wills-Moren et al., 1982; Abe, 1991; Dow and Scattergood, 1990; Stümpel and Becker, 1991). Unfortunately, traditional methods of working brittle materials such as lapping, polishing and chemical etching are processes which, in addition to being time-consuming, introduce figure errors into the original surface. Diamond turning and form-grinding are viable options for manufacturing optical surfaces with adequate surface finish for use in infra-red and forseeably in visual light applications, both spherical and aspherical, without the need for post-machining finish (see, e.g., Giovanola and Finnie 1980 and Tönshoff et al., 1990), This restrict ductile-regime (plastic removal of material) diamond turning requires that no cut should exceed the so called critical depth or thickness producing crack-free grooves. However, very low material removal rates are obtained (Chao, 1991).

This work proposes a modal in which a greater part of the material may be removed through brittle microfracture whilst a surface and sub surface can be obtained with low damage levels. The shape and position of the tool is such that the cracks formed would not propagate below the machined surface, being removed in subsequent cuts. It transpires that machining with single-point diamond tool may not be as uneconomical as it appears at first thought.

Model of Brittle Materials single Point Machining

Initial Observations. In the early stages of this work, the necessity to machine sample with irregular surfaces (large waviness) let to experiments based upon cut widths less than the critical feed-per-revolution (Fig. 1). since the cut was difficult to maintain over large areas. The first attempts at ductile test cuts were discouraging, since brittle fracture invariably occurred.
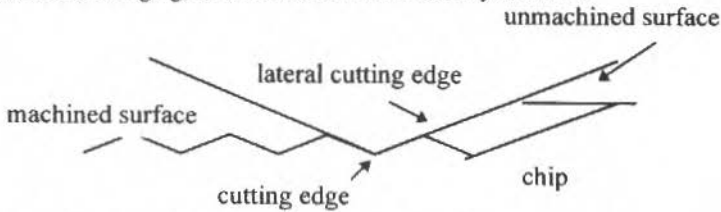

Fig. 1   Geometry of Cut with Large Depth of Cut and Small Feedrate

When the first apparently successful ductile test cut was attained, the feedrate was gradually increased to investigated the ductile/brittle transition as a function of the feed-per-revolution. After being machined, the sample was examined with Normarski microscopy. The feed was $5\,\mu m/$ revolution and the depth of cut was $7\,\mu m$, but no cracks could be observed (Fig. 2).

Since this result was very unlikely, the tool was examined on a Normarski microscope. Figure 3 is a micrograph of the cutting edge of a "roof" shape tool. As can be seen, the cutting edge has worn to become a flat surface truncation.
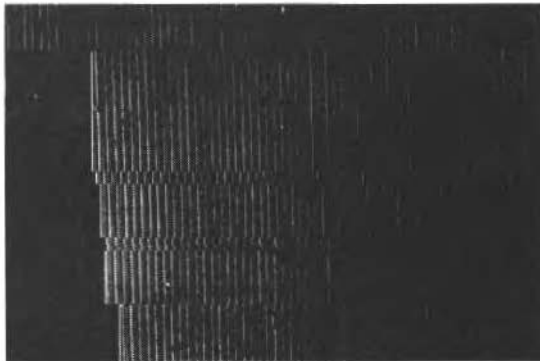

Fig. 2   Normarski Micrograph of a Silicon Sample. Feedrate $5\,\mu m$ / Rev and Depth of Cut $7\,\mu m$, but no Cracks can be Observed
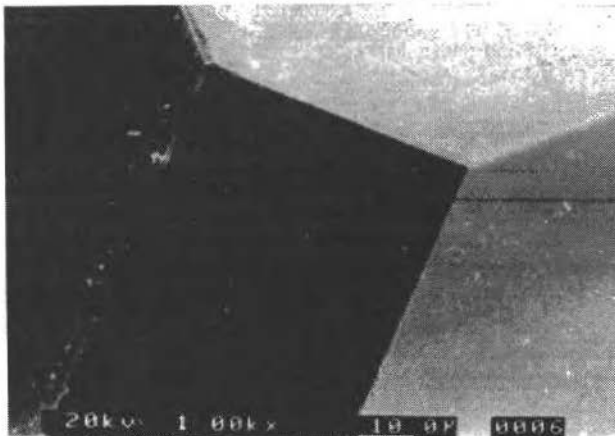

Fig. 3   Micrograph of the Cutting Edge of a Truncated "Roof" Shaped Tool

Close observation of this new "facet" shows a fine surface roughness with no visible cracks and sharp edges as if it had bee polished. As can be seen in Fig. 4, the geometry of cutis radically different from that of a roof shaped tool.
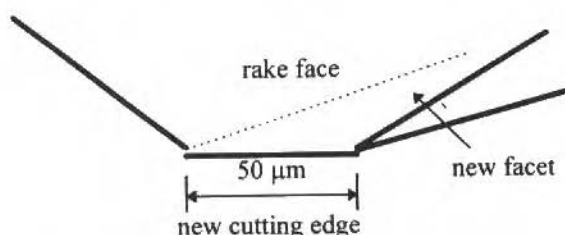

Fig. 4   Geometry of the Worn Roof-Shaped Single -Point Diamond Tool

However, this does not explain ductile machining with feedrate $5\,\mu m$ per revolution and depth of cut above $7\,\mu m$. Talysurf traces of the surface of the sample revealed a peak-to-valley amplitude of around $0.1\,\mu$ and period of around $5\,\mu m$. This profile indicated a possible tilt between the facet (worn cutting edge) and the machined surface.

Proposed Model. Considering a small lateral tilt of the tool with respect to the machined surface, the geometry would be as represented in Fig. 5. Chip formation can be divided into two distinct regions: Region I extending from the surface S down to the depth of the corner C and Region II extending from corner C down to the depth of the tool tip T. Because of the different angles of the toll in the direction of feed, the chip width in region I will approach the feed/revolution value whereas in region II it will be much thinner. With the high feedrate employed ($5\,\mu m$ / revolution) region II may be expected to initiate lateral cracking. As shown by Lawn and Swain (1975) this may be expected to extend downward for a few micrometres, i.e., to a maximum depth d_b of brittle cut.

If, however, the angle of the tool in region II from C to T causes a subcritical chip width, machining there can be expected to be ductile and the region II ductile. machining may be expected to remove the brittle cracking caused by region I.
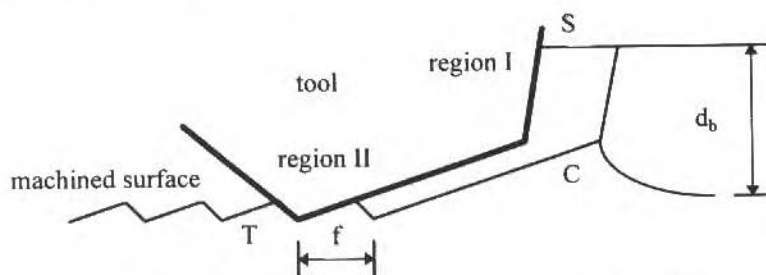

Fig. 5   Geometry of Cut with the Tiled with Respect to the Machined Surface

The chip can be divided in two distinct regions. In region I (from the unmachined surface up to about $3\,\mu$ above the machined surface) the chip is about $4\,\mu$ thick which most certainly would give rise to brittle fracture. Region II of the chip (up to about $3\,\mu$ above the machined surface) chip thickness is very fine (less than $0.3\,\mu$ thick) and, therefore, can be considered in plane stress state (classical orthogonal cut). Material in this region may shear and deform up the front (rake) face of the tool without cracking.

A possible explanation for the attainment of a fine machined surface is that the cracks in region I propagated sideways and upwards (instead of penetrating vertically downwards), in which case a tilt of the tool would not have any influence on the result obtained. However, in order to investigate the influence of the tilt, a polished silicon sample was machined (faced) with the same parameters (cross

feed 5 μ /rev and depth of 7 μ) but with both toll and sample carefully set up so that the cutting edge of the tool was parallel to the sample surface (no tilt). The machined surface was examined with Normarski and scanning electron microscopy showing considerable damage as shown in Fig. 6.

This result led to the basic hypothesis that cracks in region I would propagate downwards as well as sideways (Fig. 7) but, since region I is about 3 micrometers above the machined surface, cracks would not propagate below the machined surface, being removed in subsequent cuts.

In order to demonstrate the validity of this model, a series of test cuts were carried out as follows.

Fig. 6   Micrograph of Machined Silicon Sample. Depth of Cut 7 μ , Feedrate 5 μ /Rev and no Tilt Between Cutting Edge and Sample Surface
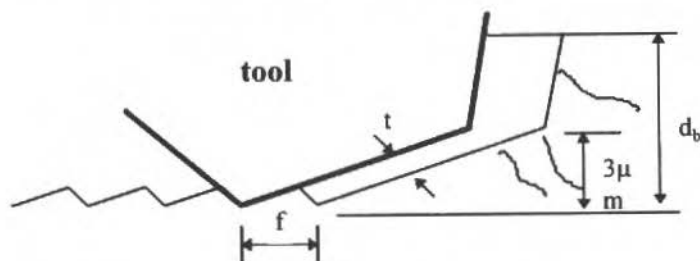

Fig. 7   Model of Propagation of Cracks in Diamond Turning of Brittle Materials

(1) Effect of the tilt (δ). A polished silicon sample was faced with a truncated ("flat"-tip) tool (Fig. 3), whose leading face was overhung by 30° arc from vertical in the cutting direction (i.e., equating to a tool "rake" angle of -30°). Other parameters are: feedrate (f) 3 μ / rev, depth of cut (d) 5 μ , rake angle (a) 30° and different tilts (δ) of the front cutting edge with respect to the sample surface (Fig. 8) by inserting foils known thickness under a side of the tool mount.

Three test cuts were done: δ = 4.5° (h = 4 μ), δ = 3° (h = 2.6 μ) and δ = 2° (h = 1.7 μ). The results are summarized in Table 1.

(2) Effects of the feed-rate. Test cuts were performed on a polished silicon sample for four different feedrates f = 5.0, 5.5, 6.0 and 6.5 μ /rev with respective thickness of chip in region II t = 0.39, 0.43, 0.47 and 0.50) μ . The other parameters were kept constant: δ (°) = 4.5°, d= 7 μ and α = 30°.

Table 1   The Influence of the Tilt of the Tool in the Machined Surface (Polished Silicon)

δ °	h (μ)	comments
4.5	4.0	no detectable damage
3.0	2.6	some cracks observed (Fig. 9)
2.0	1.7	a large number of cracks (Fig. 10)
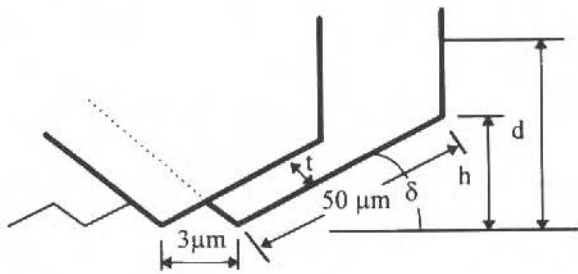
Fig. 8   Geometry of Cut. Feedrate 3 μ   /Rev, Depth of Cut 5 μ   , Rake Angle 30° and Variable Tilt

For t = 0.39 μ   and 0.43 μ   the machined surface exhibited no damage, but large cracks could be observed for t = 0.47 μ   and 0.50 μ   . This test shows that if t exceeds a critical value (around 0.43 μ   ), a sharp transition from plastic removal to brittle fracture occurs in region II, propagating cracks below the machined surface.
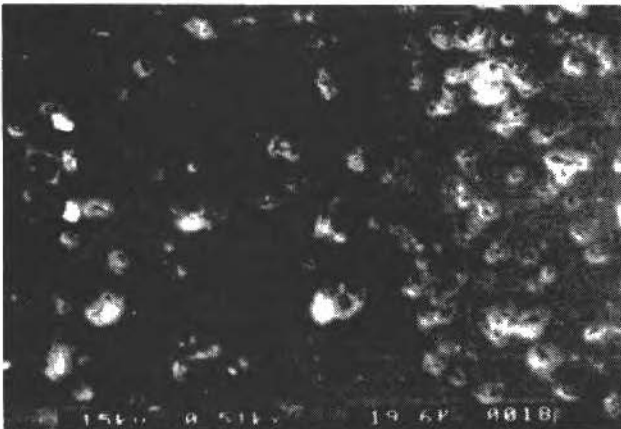
Fig. 9   Micrograph of Machined Silicon Sample. Cutting Parameters: See Text, δ = 3°
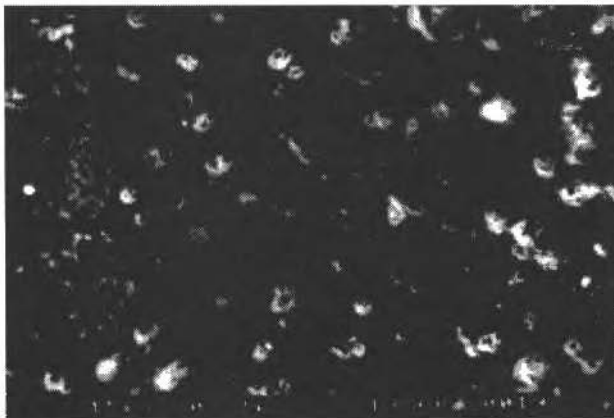
Fig. 10   Micrograph of a Machined Silicon Sample. Cutting Parameters: See Text, δ = 2°

(3) Influence of errors in the feed mechanism on the chip thickness. From Fig. 11, the chip thickness may be written as

$t = f.\sin \delta$

Assuming $\delta = 4.5°$, $t = 0.078$ f, thus if there is an error in f of $\pm 2\mu m$, the variation in the chip thickness will be less than 8% of this, i.e., ± 8nm.

Fig. 11   Influence of Feedrate and In-Feed Errors on Chip Thickness

(4) **Influence of spindle run out**. From Fig. 11, it can be seen that vertical displacements due to errors (either from the in-feed mechanism or spindle) cause the chip thickness to vary nearly the same quantity, however, (slow) creep motions of the in-feed mechanism and radial run-out of the spindle will have little influence on the chip thickness.

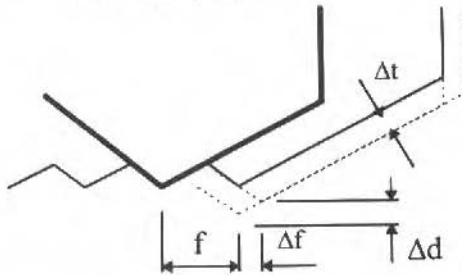(5) **Influence of peripheral speed**. The material removal rate is proportional to the feedrate which depends on the spindle speed and advance. However, if the peripheral speed exceeds a certain limit, the local (point of contact of the tool) temperature of the material increases causing the material to melt.

Conclusions

Ultra-precision machining to sub-micrometric depths is shown to be a threshold area of work requiring a combination of the best of materials, measurement and control (McCue, 1983). Such levels of performance permit exploitation of a regime of machining in ostensibly brittle materials such that brittle crack propagation is not significant. Investigations based on earlier indentation results (Lawn and Wilshaw, 1975; Lawn and Evans, 1977; Puttick et al., 1989) show clearly that, subject to the requirement for monitoring the cut below some critical ingress dimension, e.g., of the order of 0.5 μ in silicon, significant areas can be machined to a "mirror finish".

Investigations (both theoretical and experimental) of single-point machining of brittle materials confirm the critical depth of cut for ductile behaviour was in the submicrometric region. However, apparently order of magnitude increases in cut depth could be used by controlled brittle machining with damage limited to some depth and "cleaning up" simultaneosly of this by a different region of the tool as shown in Fig. 7.

It is considered that exploitation of this may have implications for the economics of single-point machining as a productive process.

References

Abe, T., 1991, "A Future Technology for Silicon Wafer Processing for VLSI", Precision Engineering, Vol. 13(4), pp. 251-255.

Chao, C-L., 1991, "Investigations of the Machining of Glasses and Other Normally Brittle Materials", Ph.D. Thesis, Cranfield University, Cranfield, Bedford, UK.

Dow, T. A., and Scattergood, R. O., 1990, "Ductile/brittle Transition and Development of Ductile Mode Grinding Technology", J. Japan. Soc. Prec. Eng., Vol. 56(5), pp. 18-23.

Giovanola, J. H., and Finnie, I., 1980, "On the Machining of Glass", J. Mater. Sci., Vol. 15 pp. 2508-17.

Lawn, B. R., and Evans, A. G., 1977, "A Model for Crack Initiation in Plastic/Elastic Indentation Fields", J. Mater. Sci., Vol. 12, pp. 2195-2201.

Wills-Moren, W. J., Modjarrad, H., and Read, R. F. J., 1982, "Some Aspects of the Design and Development of a Large High Precision Diamond Turning Machine", Annals of the CIRP, Vol. 38(1), pp. 409-414.

Lawn, B. R., and Swain, M. V., 1975, "Microfracture beneath Point Indentation in Brittle Solids", J. Mater. Sci., Vol. 10, pp. 113-122.

Lawn, B. R. and Wilshaw, R., 1975, "Review of Indentation Fracture: Principles and Applications", J. Mater. Sci., Vol. 10, pp. 1049-1081.

McCue, H. K., 1983, "The Motion Control System for the Large Optics Diamond Turning Machine (LODTM)", Proc. SPIE, Vol. 433, pp. 68-75, San Diego, CA, USA.

McKeown, P.,1986, "High Precision Manufacturing and the British Economy", Proc. I. Mech. E., Vol. 200, pp. 1-19, London, UK.

McKeown, P. A., Carliste, K., Shore, P., and Read, R. F. J., "Ultra-Precision, High Stiffness CNC Grinding Machines for Ductile Mode Grinding of Brittle Materials", Proc. SPIE, Vol. 1320, pp. 301-313.

Puttick, K. E., and Franks, A., 1990, "The Physics of Ductile-Brittle Machining Transitions: Single-Point Theory and Experiments", J. Japan. Soc. Prec. Eng., Vol. 56(5), pp. 12-17.

Puttick, K. E., Rudman, M. R., Smith, K., Franks, A., and Lindsey, K., 1989, "Single-Point Diamond Machining of Glasses", Proc. Roy. Soc. A., Vol. 426, pp. 19-30.

Smith, S. T., 1990, "Machining of Silicon Using High-Speed Miniature Diamond Cutters", J. Phys. D: Appl. Phys., Vol. 23, pp. 607-616.

Stümpel, J., and Becker, P., 1991, "Silicon as a Length and Angle Ruler in Nanotechnology", Proc. of the 6th International Precision Engineering Seminar (IPES 6), Braunschweig, W. Germany, pp. 31-38.

Tönshoff, H. K., Schmieden, W. V., Inasaki, I., König, W., and Spur, G., 1990, "Abrasive Machining of Silicon", Annals of the CIRP, Vol. 39(2), pp. 621-635.

Análise do Comportamento Estático e dos Autovalores e Autovetores de Manipuladores Flexíveis

Analysis of the Structural Static Response, Eigenvalues and Eingenvectors of Manipulators With Flexible Joints and Links

Fernando Antonio Forcellini
Nelson Back
Universidade Federal de Santa Catarina
Departamento de Engenharia Mecânica
88040-900 Florianópolis, SC Brasil

Abstract

This work presents a methodology for simulation and analysis of the manipulators with flexible joints and links. Are proposed numerical procedures that permit obtain the structural static response, natural frequencies, vibration modes for diferents positions of the system.
Keywords: Flexible Joint Robots, Structural Static Response, Natural Frequencies, Vibration Modes

Resumo

Na fase de projeto preliminar de manipuladores articuladores, é de fundamental importância a utilização de ferramentas que possibilitem a análise de seu cmpontamento estrutural. Estas ferramentas devem, a partir de uma modelagem represenrativa, permitir a simulação do sistema em diferentes situações. Este trabalho apresenta uma sistemática para a simulação e análises estática e dos autovetores, onde são consideradas as flexibilidades das ligações e juntas. São mostrados os resultados de simulações para várias posições de um manipulador dentro de seu espaço de trabalho.
Palavras-Chave: Manipuladores Flexíveis, Comportamento Estrutural

Introdução

Atualmente há uma grande necessidade de sistemas robotizados que possuam características superiores de performance tais como, alta precisão e repetibilidade, boa capacidade de carga e baixo peso. Sendo que para um bom projeto tanto mecânico como do sistema de controle de robôs manipuladores, é de fundamental importância a modelagem e simulação dos mesmos.

Este trabalho tem por objetivo apresentar um procedimento destinado a simulação e análise da estrutura de sistemas robóticos articulados, quando estes estão na fase de projeto preliminar, possibilitando que a concepção seja avaliada e obtidas informações importantes para as demais fases de projeto.

A característica principal deste procedimento é a consideração da flexibilidade das ligações e juntas do método de elementos finitos e das equações de Lagrange na modelagem, e a abordagem numérica empregada.

Modelagem

O sistema a ser modelado constitui-se de uma cadeia cinemática aberta, de corpos flexíveis interconectados por juntas rotacionais, e a modelagem utilizada segue o procedimento proposto por Forcellini (1994), que é baseado no formalismo Lagrangeano, e resulta num modelo expresso em termos de coordenadas generalizadas, que representam os grandes deslocamentos das juntas e os pequenos deslocamentos devidos à flexibilidade das ligações.

Com relação às juntas/sistema de acionamento, a modelagem leva em conta a inércia dos atuadores, relações de transmissão envolvidos e sua elasticidade, a qual é considerada através de molas torcionais lineares. As ligações são tratadas através de técnica de elementos finitos, onde são considerados os

efeitos de deflexão, deformação axial, cisalhamento, inércia rotatória e torção permitindo assim a modelagem adequada de vigas curtas e longas.

O modelo é expresso através de um conjunto de equação diferenciais, expresso conforme as Eqs. (1) e (2), onde [M(p)] é a matriz de inércia do sistema; [C(p, p)] é a matriz que contém os efeitos giroscópicos; [K] é a matriz que engloba a rigidez das ligações e das juntas; {G(p)} é o vetor que contém as cargas devidas á gravidade, e o vetor {Q(p)} os carregamentos externos. O vetor das coordenadas generalizadas é dada por $\{p\} = \{\theta\, q\, \phi\}^T$, onde os θ's são as coordenadas de corpo rígido das ligações, os q's representam as coordenadas nodais do modelo e os ϕ's são as coordenadas dos rotores dos atuadores.

$$\begin{bmatrix} M_{\theta\theta} & M_{\theta q} & 0 \\ M_{q\theta} & M_{qq} & 0 \\ 0 & 0 & M_{\phi\phi} \end{bmatrix} \begin{Bmatrix} \ddot{\theta} \\ \ddot{q} \\ \ddot{\phi} \end{Bmatrix} + \begin{bmatrix} C_{\theta\theta} & C_{\theta q} & 0 \\ C_{q\theta} & C_{qq} & 0 \\ 0 & 0 & 0 \end{bmatrix} \begin{Bmatrix} \dot{\theta} \\ \dot{q} \\ \dot{\phi} \end{Bmatrix}$$

$$+ \begin{bmatrix} K & 0 & -K \\ 0 & U & 0 \\ -K & 0 & K \end{bmatrix} \begin{Bmatrix} \theta \\ q \\ \phi \end{Bmatrix} + \begin{Bmatrix} G_\theta \\ G_q \\ 0 \end{Bmatrix} = \begin{Bmatrix} Q_\theta \\ Q_q \\ Q_\theta \end{Bmatrix} \tag{1}$$

ou

$$[M(p)]\{\ddot{p}\} + [C(p,p)]\{\dot{p}\} + [K]\{p\} + \{G(p)\} = \{Q(p)\} \tag{2}$$

Análise Estática

Nesta análise, são desprezados os dois primeiros termos do lado esquerdo da Eq. (2), de modo a obter-se as seguintes equações de equilíbrio estático

$$\begin{bmatrix} K & 0 & -K \\ 0 & U & 0 \\ -K & 0 & K \end{bmatrix} \begin{Bmatrix} \theta \\ q \\ \phi \end{Bmatrix} = \begin{Bmatrix} Q_\theta(\theta, q) \\ Q_q(\theta, q) \\ Q_\phi(\theta, q) \end{Bmatrix} \tag{3}$$

onde o vetor carga $Q(\theta, q)$ contém as parcelas devidas a forças externas à gravidade.

Devido ao vetor carga Q ser função das coordenadas θ e q, as quais são também as incógnitas do problema, foi desenvolvido um procedimento para a solução deste problema, o qual é descrito a seguir.

Na obtenção do comportamento estático do sistema, o objetivo é determinar o deslocamento das coordenadas generalizadas para diferentes posições do sistema. Como nesta situação é conhecido o valor das coordenadas ϕ's, e considera-se não haver movimento algum nos atuadores, o problema consiste na determinação das coordenadas de corpo rígido das ligações θ's, e das coordenadas nodais q's das ligações.

Como pode ser observado, os elementos do vetor dos carregamentos do sistema de equações lineares Eq. (3), são funções das coordenadas θ's e q's que são incógnitas do sistema.

Para uma primeira aproximação para o vetor dos carregamentos, são utilizados valores para os θ's, fornecidos pela seguinte relação

$$\{\theta_R\} = \{\phi\} - [K]^{-1}\{Q_{\theta R}\} \tag{4}$$

que é obtida da Eq. (3), considerando o manipulador contendo juntas flexíveis e ligações rígidas, e $\{Q_{\phi R}\}$ sendo o torque nas juntas considerando o manipulador rígido. Desta forma, $\{\theta_R\}$ representa o vetor contendo os deslocamentos de corpo rígido das ligações devido á flexibilidade das juntas.

Com estes valores dos θ 's obtidos, e considerando o desacoplamento entre a rigidez das ligações e das juntas, parte-se para uma determinação aproximada das coordenadas nodais utilizando o seguinte sistema de equações

$$[U]\{u\}^{(i)} = \{Q_q(\theta_R, q_R)\} \tag{5}$$

onde Q_q é aproximado utilizando-se os θ 's e os valores de q_R como iguais a zero.

Com os θ 's e os q_R's obtidos parte-se para a determinação inicial das coordenadas θ's utilizando a seguinte expressão

$$\{\theta\}^{(i)} = [K]^{-1}\{Q_\theta(\theta_R, q^{(i)})\} + \{\phi\} \tag{6}$$

com $\{\theta\}^{(i)}$ obtido parte-se para a obtenção de $\{q\}^{(i+1)}$, e assim sucessivamente seguindo o seguinte esquema iterativo

$$[U]\{q\}^{(i+1)} = \{Q_q(\theta^{(i)}, q^{(i)})\} \tag{7}$$

$$\{\theta\}^{(i+1)} = [K]^{-1}\{Q_\theta(\theta^{(i)}, q^{(i+1)})\} + \{\phi\} \tag{8}$$

onde $\{u\}^{(1)}$ e $\{\theta\}^{(1)}$ são obtidos das Eq. (5) e (6), respectivamente.

O processo iterativo segue até que ocorra a convergência, ou seja $\sum|q^{(i-1)} - q^{(i)}| \le TO$.

Nesta etapa , também pode-se obter a resposta estática do sistema considerando-se somente a flexibilidade das ligações. Para isto, são utilizadas as Eqs. (5) e (7) e considerando-se $\theta = \theta_R = \phi$.

A resolução dos sistemas de equações anteriormente mostrados é feita utilizando-se o método de Gauss com pivotamento.

Análise dos Autovalores e Autovetores

O objetivo desta análise é a determinação das freqüências naturais e modos de vibração do sistema modelado. Esta análise deverá ser feita para várias posições do manipulador, dentro de seu espaço de trabalho, uma vez que a inércia do sistema é dependente de sua configuração.

O autoproblema a ser tratado nesta etapa é representado pela seguinte equação

$$\begin{bmatrix} K \\ & U \end{bmatrix}[\phi] = [\Lambda]\begin{bmatrix} M_{\theta\theta} & M_{\theta q} \\ M_{q\theta} & M_{qq} \end{bmatrix}[\phi] \tag{9}$$

onde $[\theta]$ é a matriz cujas colunas são os autovetores, e $[\Lambda]$ é uma matriz diagonal que contem os autovalores.

Para a solução do autoproblema, implementou-se no programa o método da Iteração Subespacial (Bathe e Wilson, 1984), o qual fornece os primeiros p autovalores ordenados, bem como os correspondentes autovetores.

Assim como na análise estática, pode-se obter os autovalores e autovetores do sistema, considerando-se apenas as flexibilidades das ligações. Para isto, o autoproblema é montado da seguinte forma

$$[U] [\phi] = [\Lambda^*] [M_{qq}] [\phi] \tag{10}$$

Simulações e Resultados

Para ilustrar os resultados obtidos com a formulação e procedimentos numéricos apresentados, será considerada uma situação de projeto de um manipulador articulado, onde já se tem definidas as configurações cinemática e estrutural, ou seja, já definidos o comprimento, material forma de cada ligação, e as transmissões envolvidas.

O manipulador a ser analisado possui três ligações, como mostra o esquema da Fig. 1, e apresenta as seguintes características: comprimentos das ligações $L_1 = 660,4$ mm, $L_2 = 431,8$ mm e $L_3 = 433,1$ mm; comprimento dos ombros $l_{y1} = 200$ mm e $l_{z2} = 100$ mm; massas das ligações $m_1 = 13,21$ kg, $m_2 = 17,80$ kg e $m_3 = 5,1$ kg; módulos de elasticidade $E_1 = E_2 = E_3 = 210$ GPa; módulos de elasticidade transversal $G_1 = G_2 = G_3 = 79$ GPa; áreas de seções transversais $A_1 = 2544,91$ mm^2, $A_2 = 5244,63$ mm^2 e $A_3 = 1498,16$ mm^2; momentos de inércia $I_1 = 515388,17$ mm^4, $I_2 = 2187047,04$ mm^4 e $I_3 = 178363,02$ mm^4.
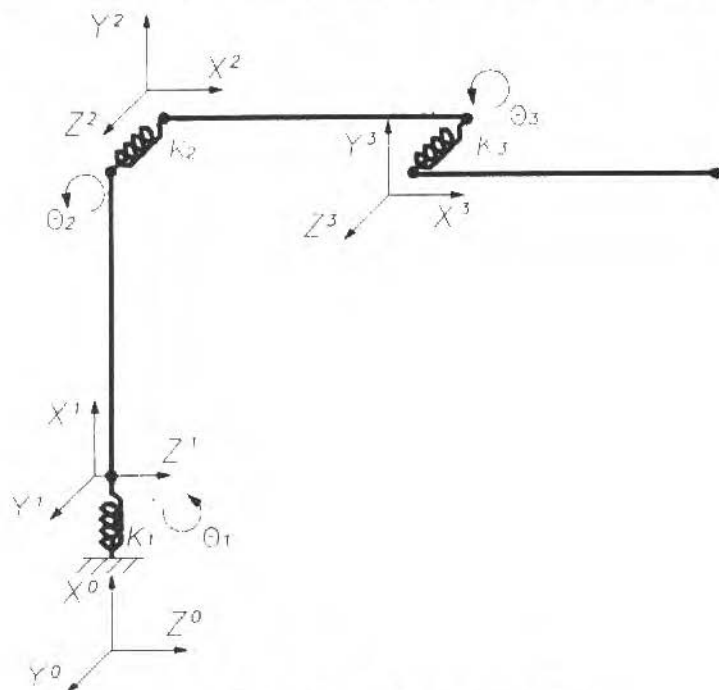
Fig. 1   Modelo da Cadeia Cinemática

Para este manipulador, considera-se para a rigidez das juntas, os mesmos valores utilizados por Lin e Yuan (1990) para manipuladores articulados, que são: $K_1 = K_2 = K_3 = 30 \times 10^6$ Nmm/rad.

As simulações foram feitas para dez diferentes posições da cadeia cinemática dentro do espaço de trabalho, mostradas na Fig. 2. Foi utilizada uma malha onde considerou-se cada ligação discretizada através de cinco elementos finitos, ou seja $n_1 = n_2 = n_3 = 5$ elementos.

Análise estática. O objetivo principal é a verificação da precisão de posicionamento da extremidade da cadeia, e como esta é influenciada pelos parâmetros de rigidez do sistema.

	1	2	3	4	5	6	7	8	9	10
φ_1	0°	0°	0°	0°	0°	0°	0°	0°	0°	0°
φ_2	0°	0°	0°	30°	45°	60°	75°	90°	90°	90°
φ_3	−90°	−45°	0°	−30°	−45°	−60°	−75°	−90°	−45°	0°

Fig. 2   Posições do Manipulador

Para cada posição foram determinados os deslocamentos das coordenadas de corpo rígido das ligações e também das coordenadas nodais das ligações, devido à flexibilidade das juntas e ligações respectivamente.

Com estes resultados, foi possível a obtenção dos erros de posição da extremidade da cadeia cinemática. Estes erros são obtidos através da diferença entre a estrutura rígida e deformada.

A Fig. 3 apresenta a variação dos valores de erro no plano XZ, para as dez posições mostradas na Fig. 2, onde é considerado apenas o efeito da gravidade atuando sobre o sistema.

A Fig. 4 mostra a variação do deslocamento sofrido pelas ligações em torno dos eixos das juntas 2 e 3, para as dez posições, devidos à elasticidade do sistema de transmissão.
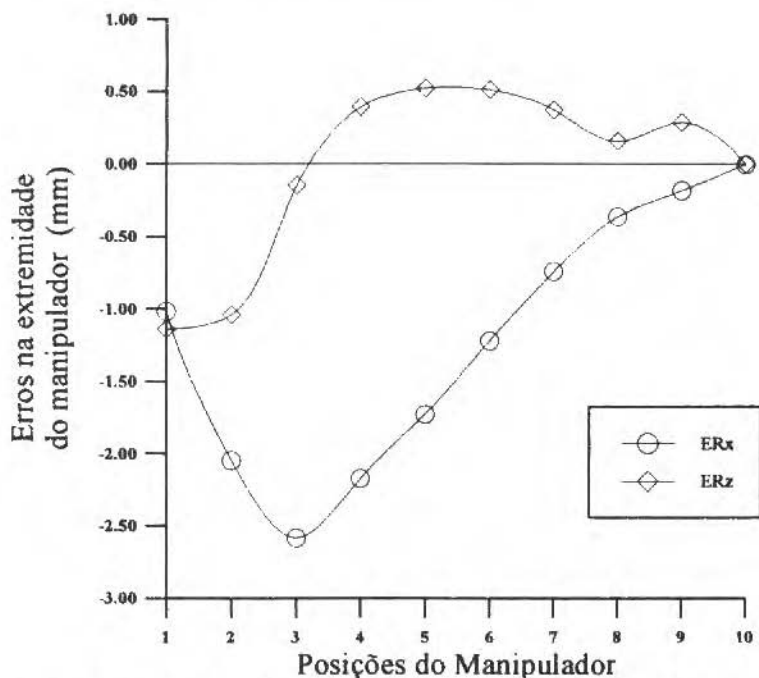
Fig. 3   Erros na Extremidade do Manipulador, para $K_1 = K_2 = K_3 = 30 \times 10^6$ Nmm/rad
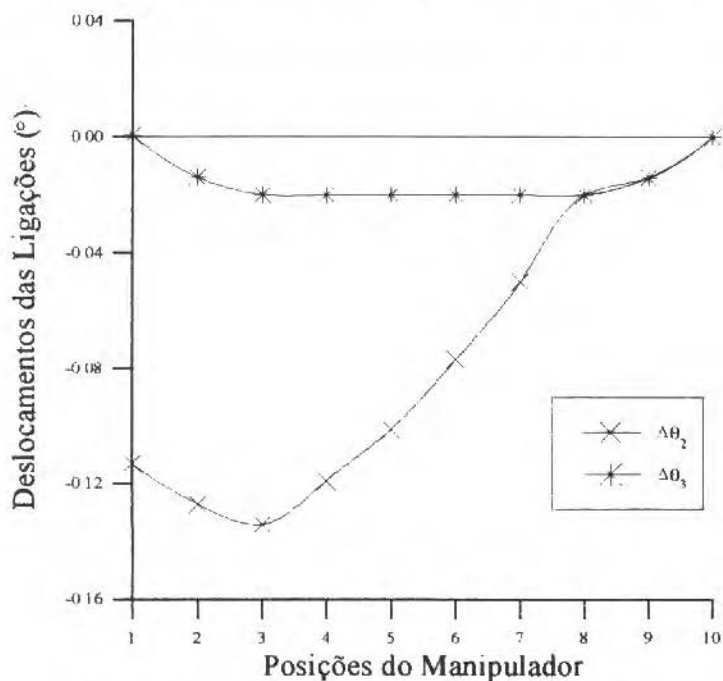

Fig. 4   Deslocamento das Ligações, para $K_1 = K_2 = K_3 = 30 \times 10^6$ Nmm/rad
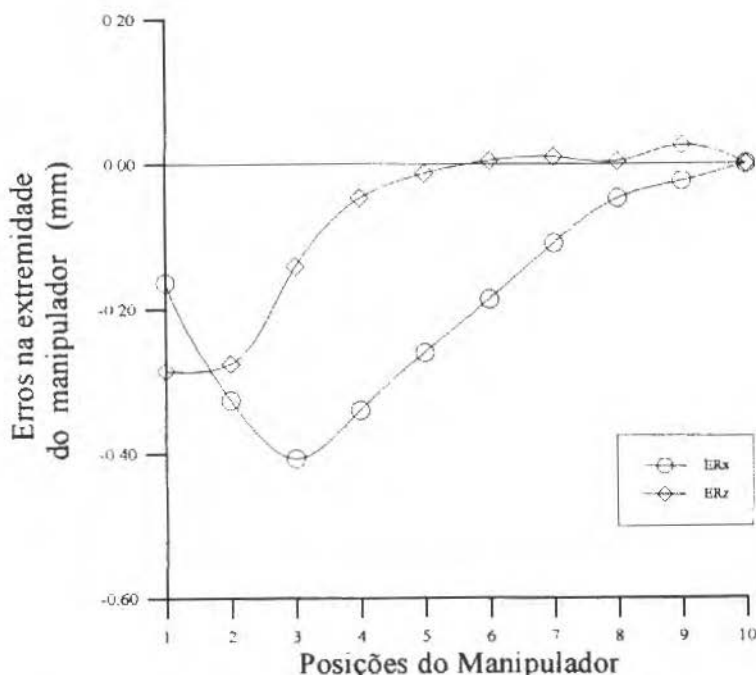
A Fig. 5, mostra os erros da extremidade do manipulador quando este é considerado como tendo as suas juntas rígidas, ou seja, os erros devidos apenas à flexibilidade das ligações . Comparando-se os valores dos erros mostrados nas Figs. 3 e 5, pode-se observar que a contribuição devida aos deslocamentos decorrentes das flexibilidades das juntas, sobre os erros, é bastante mais significativa que a devida aos deslocamentos nodais.

Observa-se que as posições onde ocorrem o maior e o menor erro, são onde a extremidade da cadeia alcança o limite do seu espaço de trabalho, e também que estão associadas, respectivamente, aos maiores e menores valores dos deslocamentos devidos à flexibilidade das juntas.

Análise dos autovalores e autovetores. O objetivo principal aqui é verificar a influência da posição e das flexibilidades do manipulador sobre as sua freqüências naturais.

Serão mostrados os primeiros autovalores e autovetores, obtidos para a mesma configuração utilizada nas simulações para o caso estático.

A Fig. 6 mostra a variação dos cinco primeiros autovalores da configuração contendo as ligações flexíveis e juntas rígidas, para as dez posições mostradas na Fig. 2.

Fig. 5   Erros na Extremidade do Manipulador Considerando as Juntas Rígidas

A Fig. 7, mostra os três primeiros autovetores para esta configuração, posicionada com as seguintes coordenadas de juntas: $\phi_1 = 0°$, $\phi_2 = 45°$ e $\phi_3 = -90°$.

A Fig. 8 mostra a variação dos autovalores, quando as juntas possuem como rigidez $K_1 = K_2 = K_3 = 30 \times 10^6$ Nmm/rad.
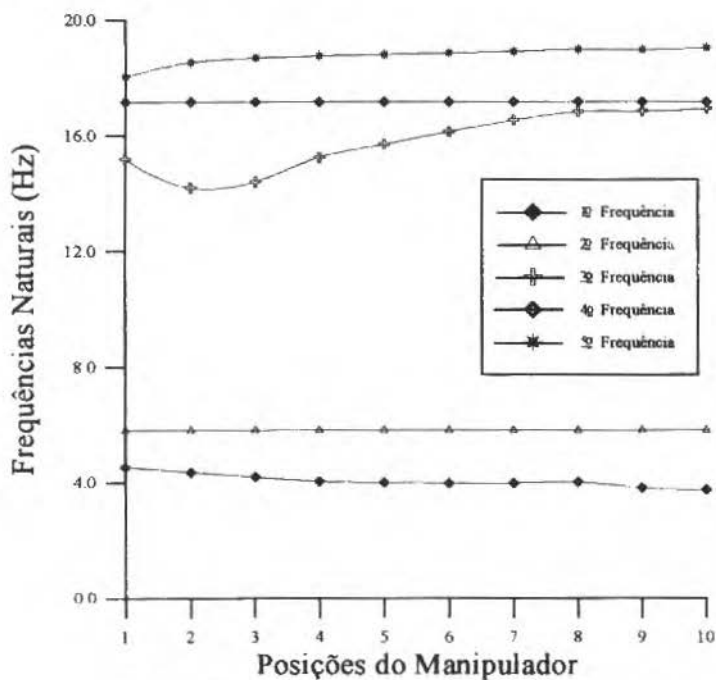
Fig. 6   Autovalores Considerando-se as Juntas Rígidas
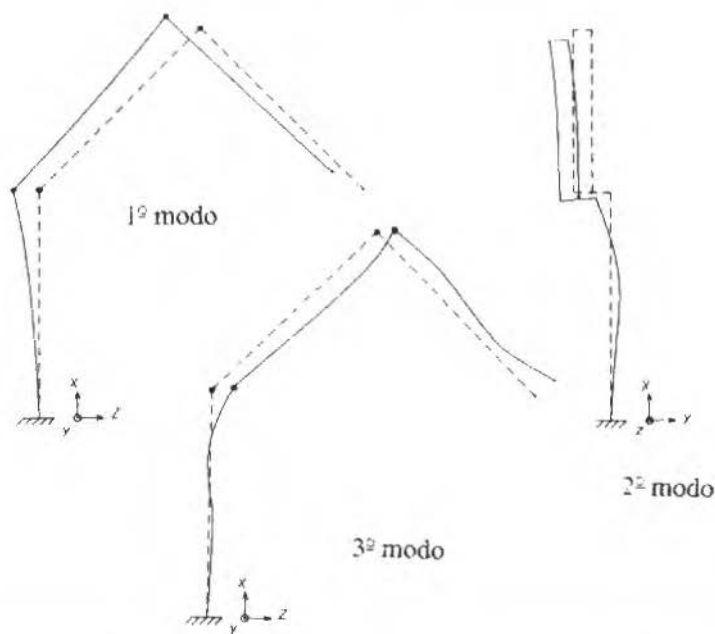
Fig. 7   Autovetores para as Três Freqüências mais Baixas, Considerando-se as Juntas Rígidas
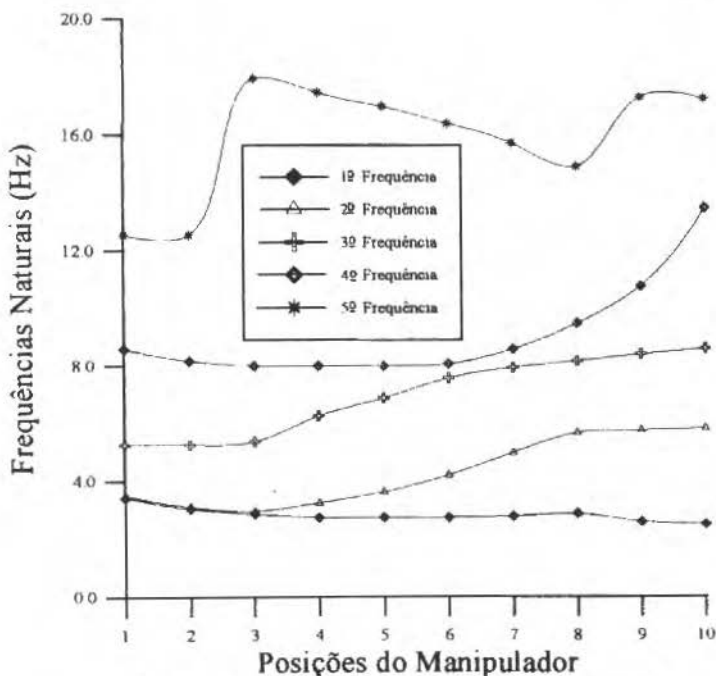
Fig. 8   Autovalores para $K_1 = K_2 = K_3 = 30 \times 10^6$ Nmm/rad

Comparando-se as Figs. 6 e 8, pode-se notar que a flexibilidade das juntas além de reduzir os valores das freqüências afeta a variação destes, para as posições da cadeia cinemática dentro do seu espaço de trabalho. Observa-se que a configuração contendo juntas flexíveis, apresenta uma diminuição média dos valores de freqüência de 35%, com relação à configuração contendo juntas rígidas.

A Fig. 9 mostra os três primeiros modos de vibração, para o manipulador contendo $K_1 = K_2 = K_3 = 30 \times 10^6$ Nmm/rad.
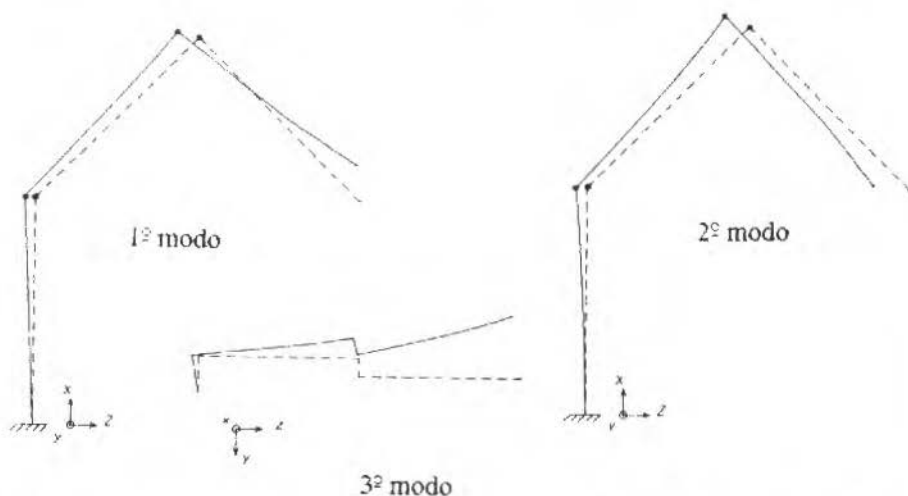
Fig. 9   Autovetores para as Três Freqüências mais Baixas, $K_1 = K_2 = K_3 = 30 \times 10^6$ Nmm/rad

Comparando-se estes modos como os mostrados na Fig. 7, observa-se que a flexibilidade das juntas gera movimentos de oscilação das ligações em torno dos eixos das juntas, e que os movimentos devidos aos deslocamentos nodais ficam menores.

Conclusões

O procedimento proposto mostrou ser bastante adequado para a obtenção de informações a respeito do desempenho estrutural da cadeia cinemática de manipuladores articulados, onde pode-se observar da influência das flexibilidades das ligações e juntas sobre o desempenho do sistema.

As análises permitem identificar os pontos críticos da estrutura, ou seja, aqueles que mais contribuem para a deterioração do desempenho.

Observou-se que a flexibilidade das juntas é a maior responsável pela deterioração da resposta estática do sistema e que exerce significativa influência sobre o comportamento das freqüências naturais e modos de vibração do sistema.

Referências

Bathe, K. J., e Wilson, E. L., 1984, "Numerical Methods in Finite Element Analysis" Prentice-Hall, New York.
Forcellini, F. A., 1994, "Sistematização da Modelagem e Simulação de Manipuladores Flexíveis", Tese de Doutorado, Univ. Federal de Santa Catarina, SC, Brasil.
Lin, L. C., e Yuan, K.,1990, "Control of Flexible Joint Robots via External Linearization Approach", Journal of Robotic Systems, Vol. 7 pp. 1-22.

Análise do Escoamento de HFC-134a em Tubos Capilares Usando o Modelo de Dois Fluidos

Analysis of the HFC-134a Refrigerant Flow through Capillary Tubes Using the Two-Fluid Model

Andre Luiz Seixlack
Universidade Estadual Paulista
Faculdade de Engenharia
Departamento de Engenharia Mecânica
15378-000 Ilha Solteira, SP Brasil

Alvaro Torebes Prata
Cláudio Melo
Universidade Federal de Santa Catarina
Departamento de Engenharia Mecânica
88040-900 Florianópolis, SC Brasil

Abstract

This work presents a numerical model to simulate refrigerant flow through capillary tubes, commonly used as expansion devices in refrigeration systems. The capillary tube is considered straight and horizontal. The flow is taken as one-dimensional and adiabatic. Steady state and thermodynamic equilibrium conditions are assumed. The two-fluid model, involving four conservation equations and considering the hidrodynamic nonequilibrium between the liquid and vapor phases is applied to the flow region. The pressure profiles and the mass flow rates given by the model are compared with experimental data.
Keywords: Refrigerant Fluid, Flow Through Capillary Tubes, Two-Fluid Model, HFC-134a

Resumo

Apresenta-se neste trabalho, um modelo numérico para a simulação do escoamento de fluidos refrigerantes no interior de tubos capilares usados como dispositivos de expansão em sistemas de refrigeração. Nesse modelo, o tubo capilar é considerado reto, horizontal, com escoamento unidimensional, adiabático, em regime permanente e sem regiões de metaestabilidade. Para a região bifásica é usado o modelo de dois fluidos, que envolve quatro equações de conservação e considerada o não equilíbrio hidrodinâmico entre as fases. Para a validação do modelo, as distribuições de pressão e os fluxos de massa obtidos são comparados com resultados experimentais.
Palavras-chave: Escoamento de Fluido Refrigerante, Tubo Capilar, Modelo de Dois Fluidos, HFC-134a

Introdução

Tubos capilares são dispositivos de expansão largamente usados em sistemas de refrigeração e condicionamento de ar de pequeno porte, com capacidade máxima da ordem de 10 KW. Consistem de um tubo de comprimento variando entre 1,0 e 6,0 m e diâmetro variando entre 0,5 e 2,0 mm, o torna a nomenclatura "tubo capilar" inapropriada uma vez que tais diâmetros são muito grandes para produzirem uma ação capilar.

Os tubos capilares exercem uma influência significativa sobre o fluxo de massa de refrigerante e, em consequência, sobre o desempenho dos sistemas de refrigeração. Para uma determinada pressão de condensação o sistema estabelece uma pressão de sucção, de forma que o fluxo de massa deslocado pelo compressor seja igual àquele fornecido pelo dispositivo de expansão.

A análise do escoamento em tubos capilares, quer seja de forma experimental ou analítica, tem sido objeto de estudo de vários pesquisadores. Bolstad e Jordan (1948) mediram as distribuições de pressão e temperatura ao longo de tubos capilares de vários diâmetros e comprimentos, que empregavam o CFC-12 como fluido refrigerante. Considerando o tubo adiabático e com líquido subresfriado em sua entrada, as distribuições obtidas foram similares àquelas mostradas na Fig. 1.

Observa-se nessa Fig. a ocorrência de uma pequena queda de pressão na entrada do tubo capilar, entre os pontos 1 e 2. Entre os pontos 2 e 3 o decréscimo de pressão é linear, enquanto a temperatura mantém-se aproximadamente constante. O ponto 3, sob condições de equilíbrio termodinâmico, corresponde ao início da vaporização do fluido refrigerante.

A partir do ponto 3 em direção ao final do tubo, as linhas de pressão e de temperatura tornam-se coincidentes e a redução de pressão é consideravelmente maior, devido à aceleração e aos efeitos causados pelo atrito no escoamento bifásico. Na saída do tubo, ponto 4, Bolstad e Jordan verificaram a existência da condição de escoamento blocado e mostraram que, alcançada tal condição, reduções posteriores na pressão de evaporação exerciam pouca influência sobre o fluxo de massa.

O escoamento em tubos capilares pode tornar-se metaestável, quando o refrigerante permanece como líquido a uma temperatura superior à sua temperatura de saturação.

Dentre os modelos teóricos encontrados na literatura, para a simulação do escoamento em tubos capilares, muitos consideram o escoamento bifásico como homogêneo. Essa é a abordagem mais simples do problema, quando o escoamento bifásico é assumido como monofásico, com pseudo-propriedades obtidas pela média ponderada das propriedades das fases individuais. Com isso, as velocidades de cada fase são consideradas iguais e as equações a serem resolvidas são as mesmas do escoamento monofásico.
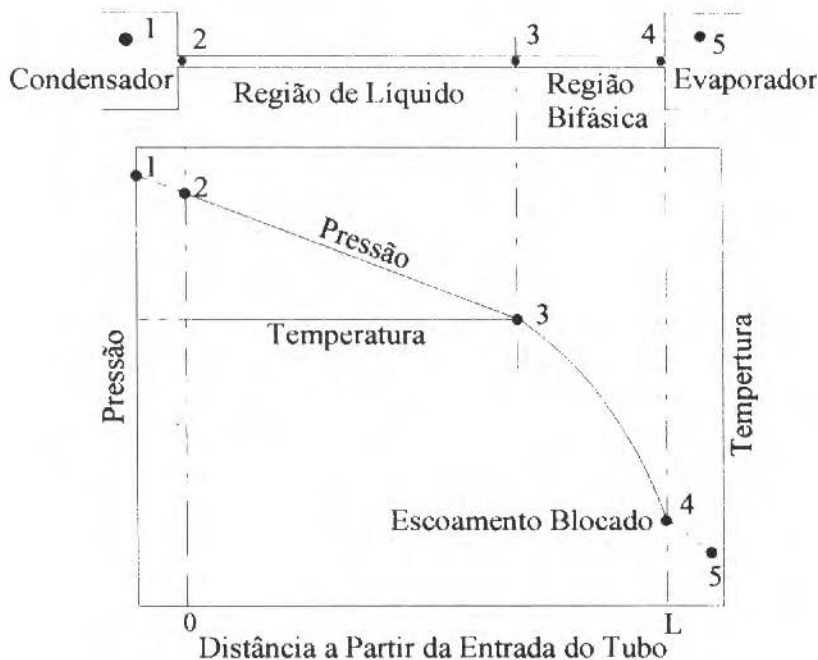
Fig. 1 Distribuições de Pressão e Temperatura ao Longo de Tubos Capilares Adiabáticos (Bolstad e Jordan, 1948).

No presente trabalho, o modelo de dois fluidos (Ishii, 1975) é usado para melhor representar o escoamento bifásico em tubos capilares. Para isso, são resolvidas quatro equações de conservação na região bifásica, permitindo que sejam considerados o não equilíbrio hidrodinâmico e três regimes de escoamento: bolhas, agitante e anular. Na validação do modelo, as distribuições de pressão e os fluxos de massa obtidos são comparados com os resultados experimentais de Melo et al. (1995), para diferentes tubos capilares operando com o refrigerante HFC-134a e em diferentes condições de operação.

Modelo Proposto

No presente modelo, o escoamento ao longo do tubo capilar é dividido em duas regiões: uma de líquido subresfriado e outra de escoamento bifásico líquido-vapor. As hipóteses simplificativas consideradas são: (i) o tubo capilar é reto, horizontal e com diâmetro constante; (ii) o escoamento é incompressível na região de líquido subresfriado; (iii) o escoamento é unidimensional, em regime permanente, adiabático e em equilíbrio termodinâmico; (iv) o refrigerante é livre de óleo. Observa-se que os efeitos de tensão superficial são desconsiderados, uma vez que é assumido que ambas as fases estejam à mesma pressão.

Equação para a região de líquido. Considerando o escoamento isentálpico nessa região, a equação da conservação da quantidade de movimento é dada por

$$\frac{dp}{dz} = -\frac{f_L G^2}{2D\rho_L} \tag{1}$$

onde z é a distância ao longo do tubo, p é a pressão, f_L é o fator de atrito calculado pela correlação de Churchill (1977), G é o fluxo de massa de refrigerante, ρ_L é a massa específica do refrigerante líquido e D é o diâmetro do tubo.

Equações para a região bifásica. As equações de conservação para as fases de líquido (L) e de vapor (V), são dadas por

(i) Conservação da massa:

$$\frac{d}{dz}[(1-\alpha)\rho_L v_L + \alpha\rho_v v_v] = 0 \tag{2}$$

onde, α é a fração de vazio (razão entre a área ocupada pela fase de vapor e a área total da seção transversal do duto) v_L e v_v são as velocidades do líquido e do vapor, respectivamente.

(iii) Conservação da qualidade de movimento para as fases de vapor e de líquido:

$$\frac{d(\alpha\rho_v v_v^2)}{dz} = -\alpha\frac{dp}{dz} - F_{WV} - F_{LV} + \Gamma_v v_i \tag{3}$$

$$\frac{d[(1-\alpha)\rho_L v_L^2]}{dz} = -(1-\alpha)\frac{dp}{dz} - F_{WL} + F_{LV} + \Gamma_L v_i \tag{4}$$

onde F_{LV} é a força interfacial por unidade de volume, atuando sobre a fase líquida na direção do escoamento e na direção oposta sobre a fase de vapor, F_{WL} e F_{WV} são as forças por unidade de volume devido ao atrito entre a parede do tubo e as fases de líquido e vapor, respectivamente, $\Gamma_k = [d(\alpha_k\rho_k v_k)/dz]$, onde k = L k = V, é a taxa de transferência de massa por unidade de volume na interface e v_i é a velocidade interfacial, dada por: $v_i = \eta v_L + (1-\eta)v_v$, sendo $\eta = 0,5$ (Wallis, 1969).

(iii) Conservação de Energia:

$$\frac{d}{dz}\left[(1-\alpha)\rho_L v_L\left(h_L + \frac{v_L^2}{2}\right) + \alpha\rho_v v_v\left(h_V + \frac{v_v^2}{2}\right)\right] = 0 \tag{5}$$

onde h_L e h_V são as entalpias das fases líquidas e de vapor, respectivamente.

Com isso, o modelo proposto consiste das equações de conservação (1) a (5), que devem ser solucionadas para o cálculo das variáveis: p, na região de líquido e v_L, v_V, p e α, na região bifásica. Para tanto, é necessário especificar as equações constitutivas para as forças F_{Wk} e F_{LV}, e as correlações para o cálculo das propriedades termodinâmicas ρ_L, ρ , h_L e h_V. Tais propriedades foram obtidas por ajustes dos dados fornecidos por Gallagher et al. (1993).

Condições de Contorno. De acordo com a Fig. 1, a pressão do refrigerante na entrada do tubo, é dada por

$$z = 0 \rightarrow p_2 = p_{cond} - \left[G^2 (1 + K) / 2\rho_L \right] \tag{6}$$

onde p_{cond} é a pressão de condensação, $K = 0,8$ (White, 1994) é o fator de perda de carga na entrada do tubo. A temperatura na entrada do tubo, T_2, é obtida em função da temperatura de saturação e do grau de subresfriamento.

Assumindo que a nucleação ocorra na pressão de saturação corresponde à temperatura de entrada no tubo capilar, $p_3 = p_{sat}(T_2)$ e considerando que as bolhas formadas sejam esféricas, as variáveis α, v_V e v_L na entrada de região bifásica são calculadas por

$$z = z_3 \rightarrow \alpha = (\pi N_i d_i^3 / 6), \quad v_V = S_i v_L \tag{7}$$

$$v_L = G / [(1 - \alpha) \rho_L + S_i \alpha \rho_V]$$

onde N_i é a densidade inicial de bolhas por unidade de volume, d_i é o diâmetro médio inicial de bolhas e $S_i = 1$ é o deslizamento inicial entre as fases. Seguindo o mesmo procedimento de Schwellnus (1988) assume-se que $N_i = 10^{11} m^{-3}$ e $d_i = 2,5 \times 10^{-5} m$.

A pressão do fluido refrigerante na saída do tubo capilar, ponto 4 da Fig. 1, corresponderá à de evaporação se o escoamento não estiver bloqueado. Caso contrário, poderá ser igual ou superior à pressão de evaporação. O critério de bocagem usado no presente modelo, baseia-se em observações teóricas e experimentais da ocorrência de um gradiente de pressão muito alto, mas finito, no local onde o escoamento torna-se bloqueado (Schwellnus 1988). Para isso, considera-se que a seção de blocagem corresponda ao incremento anterior àquele onde o sinal do gradiente de pressão (dp/dz) se inverte.

Equações Constitutivas. De acordo com o trabalho de Mikol e Dudley (1964), o escoamento ao longo da região bifásica em tubos capilares pode variar desde o regime em bolhas, com frações da vazio reduzidas, até o regime anular misto, com frações de vazio elevadas. Para valores de fração de vazio intermediários, o regime de escoamento é geralmente classificado como agitante (Wallis, 1969). No presente trabalho, é assumido que a transição do regime em bolhas para o agitante ocorra em $\alpha = \alpha_b = 0,3$ e do regime agitante para o anular em $\alpha = \alpha_a = 0,8$ conforme os dados experimentais apresentados por Wallis (1969). As relações constitutivas são razoavelmente conhecidas para os regimes em bolhas e anular, devendo ser obtidas por interpolação para o regime agitante.

(i) Atrito entre a parede do tubo e o fluido refrigerante. Para os regimes de escoamento considerados: $F_{WV} \approx 0$, uma vez que o escoamento da fase líquida é adjacente à parede do tubo. A força de atrito por unidade de volume entre a fase líquida e a parede do tubo é dada por (Carey, 1992)

$$F_{WL} = \phi_L^2 (dp/dz)_L \tag{8}$$

onde ϕ_L^2 é multiplicador bifásico, obtido segundo a correlação proposta por Lockhart e Martinelli (1949), sendo o fator de atrito calculado segundo a correlação de Churchill (1977). $(dp/dz)_L$ é o gradiente de pressão devido ao atrito, que resultaria caso o escoamento fosse somente de líquido à vazão mássica $m_L = \{ (1 - \alpha) \rho_L v_L A \}$, onde A é área da seção transversal do tubo.

(ii) Força Interfacial, F_{LV}. A força entre as fases líquida e vapor é modelada considerando o termo de força de massa virtual e o termo de força de arrasto, sendo dada por,

$$F_{LV} = \xi |v_V - v_L| (v_V - v_L) + C_{mv} (v_V v_{V,z} - v_L v_{L,z}) \tag{9}$$

onde o subíndice z indica derivada em relação à coordenada z, $\xi = \left(2C_{fi}\rho_v\alpha^{0,5}/D\right)$, C_{fi} é o coeficiente de atrito interfacial, calculado pelas correlações de Wallis (1969) e de Dobran (1987) respectivamente para os regimes em bolhas a anular e $C_{mv} = (0,5\alpha\rho_L)$ (Wallis, 1969) é o coeficiente de massa virtual.

Metodologia de Solução. A solução das equações diferenciais, tanto a Eq.'(1) quanto o sistema de equações (2) a (5), é obtida por integração usando o método de Runge-Kutta de quarta ordem. O programa calcula, ou o comprimento do tubo, para o fluxo de massa medido, ou o fluxo de massa a partir do comprimento conhecido. Nesse último caso o processo é iterativo e o fluxo de massa é ajustado para que o local de blocagem do escoamento coincida com a saída do tubo.

Resultados e Discussões

Os resultados obtidos com presente modelo foram comparados com os resultados experimentais obtidos por Melo et al. (1995), e também com os resultados fornecidos pelo modelo homogêneo. No trabalho experimental, desenvolvido por Melo et al. (1995), foram realizadas medições de fluxo de massa, de temperatura e de pressão ao longo de dois tubos capilares identificados como capilar 7: L = 2,998 m, D = 0,607 mm, ε = 1,08 μ e capilar 8: L = 2,973 m, D = 0,871 mm, ε = 0,66 μm, utilizando como fluido refrigerante o HFC-134a. Pressões de condensação na faixa de 9 a 16 bar e subresfriamento na faixa de 2 a 15° C foram escolhidos como condições de operação, sendo todos os ensaios realizados sob condições de escoamento crítico (blocado). Cabe salientar que os resultados experimentais escolhidos para as comparações mostradas neste trabalho, praticamente não apresentaram região de metaestabilidade, uma vez que tal fenômeno é previsto no presente modelo.

Nas Figs. 2 e 3 apresentam-se as comparações entre as vazões mássicas medidas e calculadas, respectivamente para os capilares 7 e 8.
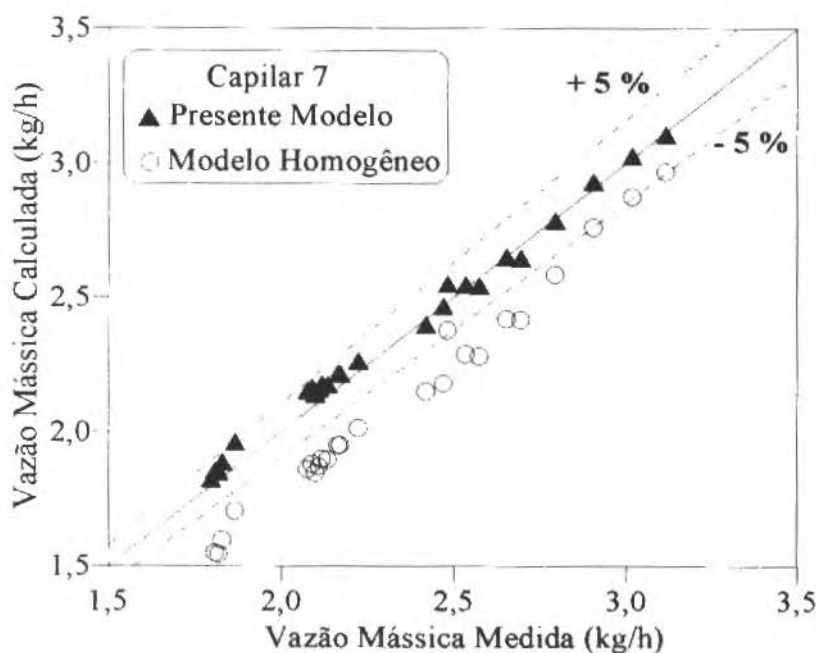

Fig. 2   Comparações entre as Vazões Mássicas Calculadas e Medidas (Melo et al., 1995) para o Capilar 7

Conforme se observa na Fig. 2, as vazões mássicas calculadas pelo presente modelo encontram-se na faixa de ±5% em relação aos valores experimentais, enquanto que para o modelo homogêneo tal diferença é ampliada para - 16%. Para o capilar 8, observe a Fig. 3, os dois modelos fornecem resultados na faixa de ±6%, sendo as vazões mássicas calculadas pelo modelo de dois fluidos superiores aos valores medidos, ocorrendo o inverso para o modelo homogêneo.
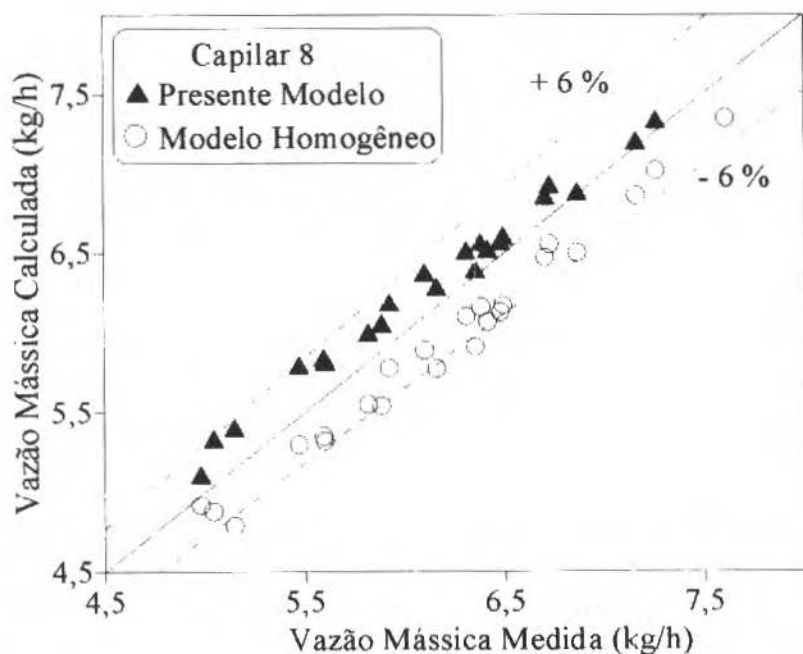

Fig. 3 Comparações entre as Vazões Mássicas Calculadas e Medidas (Melo et al., 1995) para o Capilar 8

As comparações entre as distribuições de pressão medida e calculada ao longo do tubo capilar 7, são mostradas na Fig. 4. Tais comparações são realizadas de duas maneiras: (i) mantendo fixos o comprimento e as condições de operação. Nesse caso a vazão mássica é calculada iterativamente, obtendo-se o perfil de pressão representado pela linha contínua mostrada na Fig. 4. O valor encontrado para vazão mássica calculada é 2% superior ao valor medido; (ii) mantendo fixa a vazão mássica e as condições de operação. Nesse caso, o comprimento é calculado, obtendo-se os perfis tracejados mostrados na Fig. 4. A diferença observada entre os comprimentos calculados e medidos é de 3% e 18%, respectivamente para o presente modelo e para o modelo homogêneo. Os resultados apresentados são dependentes das correlações adotadas para os fatores de atrito e para os termos interfaciais e, também, dos valores da densidade inicial de nucleação e do diâmetro inicial das bolhas.

A Fig. 5 mostra o efeito da variação do fator de atrito na região de líquido sobre o desempenho do modelo. Verifica-se uma variação considerável do perfil de pressão e também do comprimento estimado, quando os valores fornecidos pela equação de Churchill (1977) são alterados em ±5%. Quando essa equação é empregada na forma original o programa superestima o comprimento em 3%. Essa diferença passa a ser de 2% e 8%, respectivamente, quando variações de +5% e -5% são provocadas no fator de atrito. Isto destaca a necessidade do estabelecimento de equações constitutivas confiáveis, sem o que o grau de precisão do presente modelo não poderá ser melhorado.
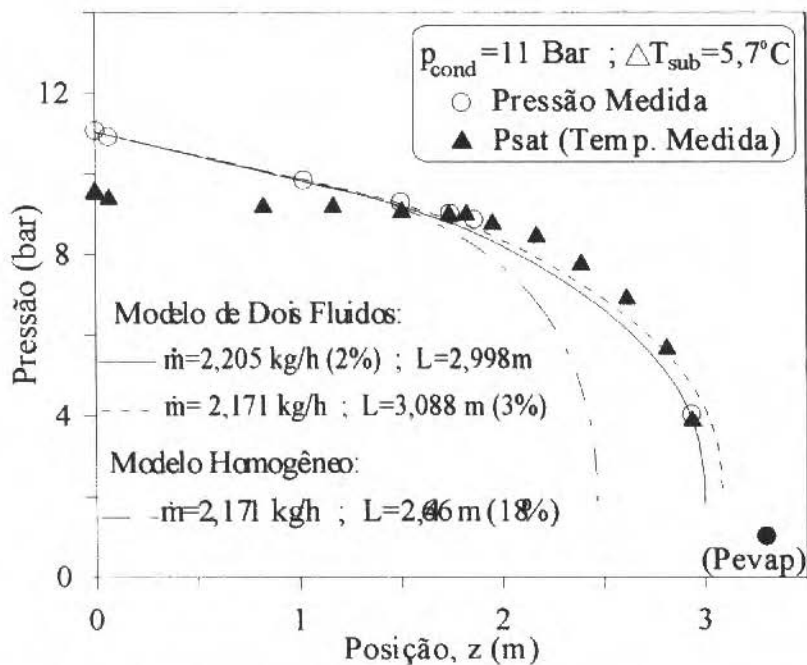
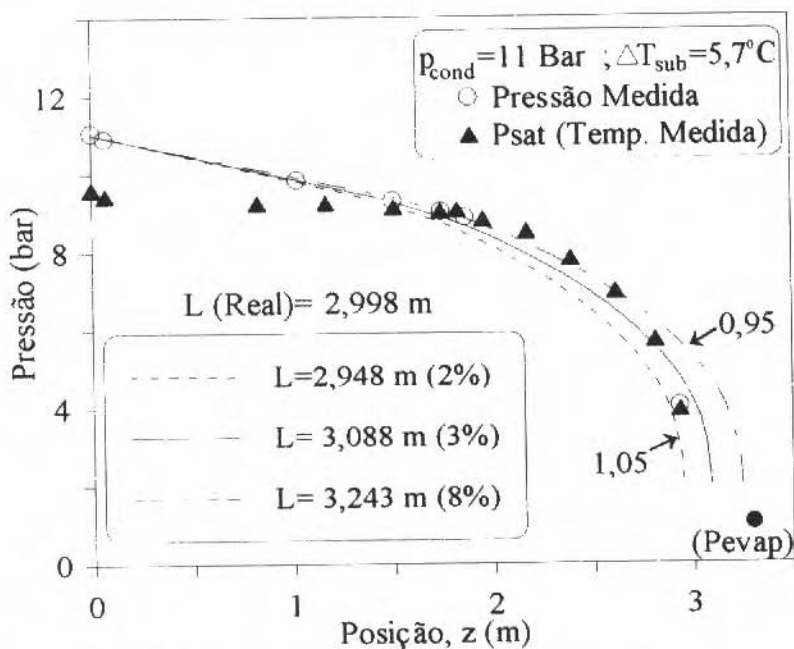Fig. 4   Distribuição de Pressão ao Longo do Tubo Capilar 7: m (Medida) = 2,171 Kg/h; L (Real) = 2,998 m

Fig. 5   Distribuições de Pressão ao Longo do Tubo Capilar 7

Na Fig. 6 são mostradas as distribuições de fração de vazio, título (x = massa de vapor/massa total) e as velocidades de cada fase ao longo do tubo capilar. Observa-se o maior aumento da fração de vazio em relação ao título e a pequena diferença entre as velocidades de cada fase.
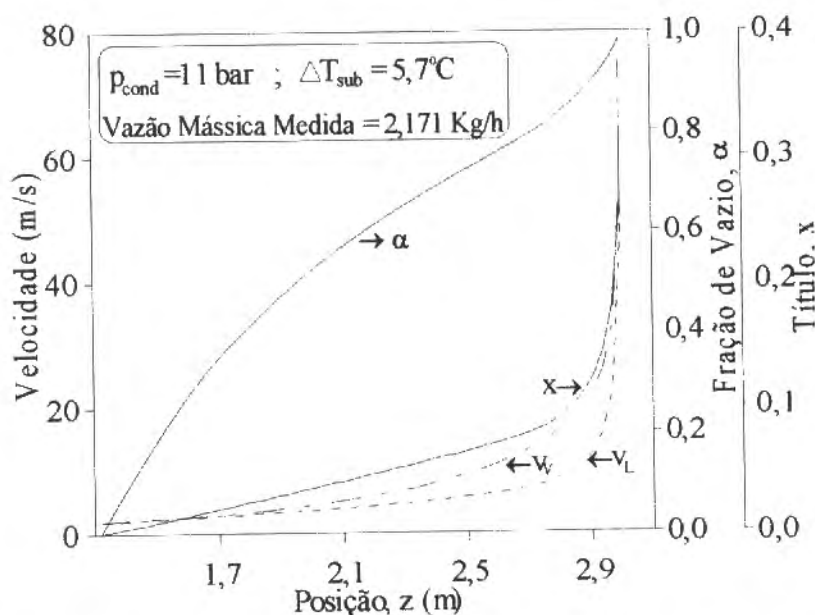
Fig. 6   Distribuição de Fração de Vazio, do Título e das Velocidades de Cada Fase ao Longo do Tubo Capilar

Conclusões

O modelo de dois fluidos é usado para simular o escoamento bifásico do refrigerante HFC-134a ao longo de tubos capilares, usados como dispositivos de expansão em sistemas de refrigeração. Nesse modelo é resolvido um sistema de quatro equações diferenciais na região bifásica, permitindo a consideração do não-equilíbrio hidrodinâmico entre as fases e a modelagem dos fenômenos interfaciais. A comparação entre os fluxos de massa calculados pelo presente modelo com os dados experimentais mostraram uma diferença de ±6%. A mesma comparação com o modelo homogêneo leva a diferenças de até -16%.

O modelo de dois fluidos permite uma abordagem mais realista do escoamento bifásico no interior de tubos capilares. Entretanto, essa sofisticação implica na utilização de um maior número de equações constitutivas em relação ao modelo homogêneo.

Agradecimentos

Este trabalho foi desenvolvido dentro de um programa de colaboração técnico-científico entre a EMBRACO S/A e a UFSC. Externamos nossos agradecimentos à EMBRACO S/A pelo apoio, que tornou possível a realização deste trabalho.

Referências

Bolstad, M. M., e Jordan, R. C., 1948, "Theory and Use of the Capillary Tube Expansion Device", Refrigerating Engineering, Vol. 56, No. 6, pp. 519-523 e p. 552.

Carey, V. P., 1992, "Liquid-Vapor Phase-Change Phenomena", Hemisphere Publishing Corporation.

Churchill, S. W., 1977, "Friction Factor Equation Span all Fluid Regimes", Chemical Engineering, Vol. 84, pp. 91-92.

Dobran, F., 1987, "Nonequilibrium Modeling of Two-Phase Critical Flows in Tubes", Journal of Heat Transfer, Vol. 109, pp. 731-738.

Gallagher, J., McLinden, M., Morrison, G., e Huber, M., 1993, "NIST Thermodynamic Properties of Refrigerants and Refrigerant Mixtures - Version 4", Gaithersburg: U. S. Department of Commerce, National Institute of Standards and Technology.

Ishii, M., 1975, "Thermo-Fluid Dynamic Theory of Two-Phase Flow", Eyrolles, Paris, France.

Lockhart, R. W., e Martinelli, R. C., 1949, "Proposed Correlation of Data for Isothermal Two-Phase, Two-Component Flow in Pipes", Chem. Eng. Prog., Vol. 45, pp. 39-48.

Melo, C., Ferreira, R. T. S., Boabaid Neto, C. Gonçalves, J. M., e Stahelin, R., 1995, "Análise do Desempenho de Tubos Capilares - Parte III, Relatório de Pesquisa Convênio EMBRACO/FEES/EMC/UFSC, Florianópolis.

Mikol, E. P., e Dudley, J. C., 1964, "A Visual and Photographic Study of the Inception of Vaporization in Adiabatic Flow", Journal of Basic Engineering, pp. 257-264.

Schwellnus, C. F., 1988, "A Study of a General One-Dimensional Two-Fluid Critical Flow Model", Master's Thesis, McMaster University, Ontario, Canada.

Wallis, G. B., 1969, "One-Dimensional Two-Phase Flow", McGraw-Hill Book Company, USA.

White, F. M., 1994, "Fluid Mechanics", McGraw-Hill Inc, USA.

Supersonic Flow Past Pressure Vent Orifices on Satellite Launcher Vehicles

Algacyr Morgenstern Jr.
Centro Técnico Aeroespacial
Instituto da Aeronáutica e Espaço
12228-904 - São José dos Campos, SP Brasil

Abstract

The unsteady, viscous, supersonic flow past a pressure vent orifice on the ogive of a satellite launcher vehicle is numerically investigated by solving the Navier-Stokes equations. The time accurate computations are performed employing an implicit numerical algorithm based on the second-order time accurate LU-SGS scheme with the incorporation of a subiteration to maintain time accuracy. Self-sustained oscillations, that affect adversely the flow past the office, are observed and its effects on the characteristics of the flow are reported through instantaneous plots. The unsteady character of the flow is further examined in the frequency domain by the use of the Maximum Entropy Method for spectral analysis and results compared with a semi-empirical formula for the prediction of the principal frequencies of oscillation of this type of flow.
Keywords: Supersonic Flow, Pressure Vent Orifices, Sound Pressure Level Attenuation.

Introduction

During ascent of a satellite launcher vehicle, the pressure in the payload bay must continuously decrease from its initial magnitude, the ambient pressure of the launching site, to values corresponding to the pressure reduction rate as the vehicle climbs to higher altitudes. This is accomplished by insertion of pressure vent orifices on the payload region of the vehicle's surface. These pressure vent orifices on satellite launcher vehicles have been observed to cause high internal noise levels during ascent, compromising the integrity of the payload. The flow past pressure vent orifices, characterized by a cavity flow phenomenon, is of a very complex nature, involving acoustic radiation from the orifice coupled with strong pressure, velocity, and density oscillations inside the orifice. Extensive experimental and theoretical studies (Heller and Bliss, 1975, Rizzeta, 1988, Kim and Chokani, 1992) have shown that the flows past cavities experiences self-sustained oscillations over a wide range of flow conditions, from low subsonic speeds to supersonic speeds. These studies demonstrated that the intensity and existence of the oscillatory flow are a function of flow and geometric parameters.

In the present work, an implicit numerical algorithm, based on the three-dimensional numerical method of Yoon and Kwak (1992), which has been successfully applied to numerous steady, viscous, turbulent, compressible flow was used. This algorithm is second-order accurate in both space and time for steady state calculations, and has a highly efficient structure, which renders CPU speeds comparable to that of explicit schemes. However, to achieve this numerical efficiency, linearization and factorization approximations are employed. In steady flow calculations these approximations are not a reason of concern, since at convergence all the errors due to the above approximations are zero. However, for unsteady flow computations, the time accuracy reduced due to the linearization and factorization approximations must be recovered. In the present work a Newton-like subiteration procedure (Matsuno, 1989) is implemented to recover the time accuracy of the algorithm when applied to unsteady problems.

In this paper, the numerical algorithm was applied to study the flow field and the sound pressure level attenuation of a labyrinth shaped pressure vent orifice on the surface of a satellite launcher vehicle. The time-accurate computations reveal self-sustained oscillations for the flow regime studied. The frequencies of oscillations agree well with semi-empirical predictions for a cavity flow without the labyrinth. In the following sections, the computational techniques used are outlined and a detailed study of the cavity flow field is reported.

Mathematical Formulation

The two-dimensional, unsteady, compressible, turbulent flow past cavities, is governed by the Reynolds averaged Navier-Stokes equations. In conservation law form and in a generalized curvilinear coordinate system (ξ, η), they may be written as

$$\frac{\partial \hat{Q}}{\partial t} + \frac{\partial (\hat{F} - \hat{F}_v)}{\partial \xi} + \frac{\partial (\hat{G} - \hat{G}_v)}{\partial \eta} = 0 \tag{1}$$

where $\hat{Q}$ is the unknown vector, $\hat{F}$ and $\hat{F}_v$ are the inviscid and viscous fluxes in the ξ direction, and $\hat{G}$ and $\hat{G}_v$ the similar fluxes in the η direction.

Numerical Algorithm

The present time-accurate numerical method is based on the observation (Matsuno, 1989) that a δ-form of the governing unsteady equations may be constructed with various combinations of the flux formulae and their Jacobians through the use of Newton-like sub-iterations. Furthermore a suitable choice of the factorization procedure yields a scheme with fast convergence and low computational time per iteration.

Eq. (1) can be written in difference form as

$$\left[\frac{3}{2}I + \Delta t \left(D_\xi \hat{A} \bullet \ + D_\eta \hat{B} \bullet \ \right) \right] \delta \hat{Q}^n$$

$$= \frac{1}{2} \delta \hat{Q}^{n-1} - \Delta t \left[D_\xi (\hat{F}^n - \hat{F}_v^n) + D_\eta (\hat{G}^n - \hat{G}_v^n) \right] \tag{2}$$

where a second order accurate Euler three-point backward time discretization is used. Here I is the identity matrix, and D is a central difference operator. The inviscid and viscous fluxes are linearized by:

$$\hat{F}^{n+1} = \hat{F}^n + \hat{A}\Delta\hat{Q}^n, \qquad\qquad \hat{F}_v^{n+1} = \hat{F}_v^n$$

and the inviscid flux Jacobian matrix defined as

$$\hat{A} = \frac{\partial \hat{F}}{\partial \hat{Q}}$$

similarly for $\hat{G}$, $\hat{G}_v$ and $\hat{B}$.

A finite volume approach is used in the treatment of the spacial discretization of the fluxes. Second order central differences are used in the left hand side. A fourth order artificial dissipation is added to the right hand side to control the undesired effect of odd and even point decoupling characteristic of central differences.

In the present two-dimensional algorithm, the lower-upper symmetric-Gauss-Seidel factorization scheme proposed by Yoon and Kwak (1992) is used. The advantage of this factorization is that the construction of the diagonal of the L and U matrices permits a scalar inversion, leading to a very efficient and vectorizable algorithm. The Jacobian matrix $\hat{A} = \hat{A}^+ + \hat{A}^-$ is approximated by

$$\hat{A}^\pm = \frac{1}{2}[\hat{A} \pm \rho(\hat{A})]$$

where

$$\rho(\hat{A}) = \max[|\lambda(\hat{A})|]$$

and $\lambda(\hat{A})$ is the eigenvalue of the Jacobian matrix $\hat{A}$. A similar procedure is applied to the Jacobian matrix $\hat{B}$.

With these approximations the factorization matrices are given by

$$L = \left(\frac{3}{2} + \Delta t \rho\right) I - \Delta t (\hat{A}^{+}_{i-1,j} + \hat{B}^{+}_{ij-1})$$

$$D = \left(\frac{3}{2} + \Delta t \rho\right) I$$

$$U = \left(\frac{3}{2} + \Delta t \rho\right) I + \Delta t (\hat{A}^{-}_{i+1,j} + \hat{B}^{-}_{ij+1})$$

where

$$\rho = \rho(\hat{A}) + \rho(\hat{B})$$

Equation (2) can thus be written as

$$LD^{-1}U\delta\hat{Q}^{n} = RHS \tag{3}$$

The solution is then obtained in three steps as follows

$$\delta\hat{Q}^{*} = L^{-1}RHS$$

$$\delta\hat{Q}^{**} = D\delta\hat{Q}^{*} \tag{4}$$

$$\delta\hat{Q}^{n} = U^{-1}\delta\hat{Q}^{**}$$

Effects of fine-scale turbulence are included by the use of a Baldwin-Lomax algebraic model with modifications to take into account multiple wall effects (Morgenstern, 1994).

Subiteration Procedure

The above algorithm has given good results for steady flow calculations, see Yoon and Kwak (1992). However, for unsteady flow calculations the approximation of the flux Jacobians matrices and the linearization procedure reduce the accuracy of the time discretization. To overcome this difficulty a procedure presented in Matsuno (1989) is introduced. At each time step a Newton-like iteration procedure is performed until convergence is achieve for each time step, while maintaining the unsteady form of the governing equations in the RHS of the algorithm. The idea of sub-iterations is that the governing equations may be iterated in pseudo time for each physical time-step. At convergence of the pseudo time iterations (sub-iterations), the linearization and factorization errors go to zero, and the full temporal accuracy of the numerical discretization is recovered. This can be obtained by adding a pseudo time derivative (Rogers and Kwak, 1991) of the dependent variable vector to Eq.(1), that may be written as

$$\frac{\partial\hat{Q}}{\partial\tau} + \frac{\partial\hat{Q}}{\partial t} + \frac{\partial(\hat{F}-\hat{F}_{v})}{\partial\xi} + \frac{\partial(\hat{G}-\hat{G}_{v})}{\partial\eta} = 0 \tag{5}$$

where τ is a pseudo time variable that bears no relation with the physical time t. The finite difference form of Eq.(5) is obtained in a similar manner as that of Eq.(2). Using a backward first-order accurate time difference formula to discretize the pseudo time derivative and applying an Euler implicit scheme at the (n+1) time level, it may be written as

$$\left[\frac{3}{2}I + \Delta t\left(D_\xi \hat{A} \bullet \; + D_\eta \hat{B} \bullet \;\right)\right]\delta\hat{Q}^{n,\,m}$$
$$= -\frac{3}{2}\left(\hat{Q}^{n,\,m} - \hat{Q}^n\right) + RHS; \; m = 0, 1, 2, 3, \ldots \tag{6}$$

where the pseudo time increment was assumed very large, and m denotes the pseudo time level. For m=0, $\hat{Q}^m = \hat{Q}^n$, and the logarithm reduces to the steady state formulation of Yoon and Kwak (1992). At convergence of the subiteration procedure $\delta\hat{Q}^{n,\,m} \to 0$ and the accuracy of the solution at each time step is the accuracy of the discretized unsteady governing equations.

Results and Discussion

The main objective of this work is to study the unsteady, compressible, viscous, turbulent, supersonic flow past pressure vent orifices. The capability of the present numerical method to compute these complex flows was validated in previous steady and unsteady computations with the computer code, presented in Morgenstern (1993 and 1994).

The computations were performed on a Cray Y-MP computer. A multiblock strategy was employed in the flow studies to efficiently utilize the computer memory. The computational rate of the code was 18.5×10^{-6} CPU sec/grid point/iteration with two subiterations. The time step was fixed to resolve the frequencies of interest in a time accurate manner. For the unsteady cavity flows, once the initial transients were purged, data was acquired for purposes of spectral analysis. A maximum entropy method (Morgenstern, 1994) for spectral estimation was applied. An attribute of the method was that exceedingly short data lengths, even less than the period of the lowest frequency of interest, are required to yield spectra. This further reduced the necessary computer time required to analyze unsteady flows.

Numerical calculations were performed for a boundary layer outer edge Mach number of 2.93 and Reynolds number of 2×10^6. The geometry of the configuration is shown in Fig. 1 and the computational grid in Fig. 2. The cavity length-to-depth ratio was 1.333. The labyrinth opening was 13 units long and its height was 13 units. Also shown in Figure 1 is the position of the pressure sampling locations, at the cavity trailing edge lip, and at a center point on the end plane of the labyrinth. For the case examined, it was observed the onset of unsteady cavity flow. The computed instantaneous velocity vectors, shown in Fig. 3, illustrates the presence of large vortical structures in the aft region of the cavity. It is also of interest to note that a series of weaker vortex structures is located ahead of this primary vortex structure. Adjacent to the wall, a number of flow reversals are observed, and these disturbances propagate inside the labyrinth region. A series of instantaneous pressure contour plots for four different instants in time incremented by a constant Δt are shown in Fig. 4. The basic unsteady character of the cavity flow can be seen.
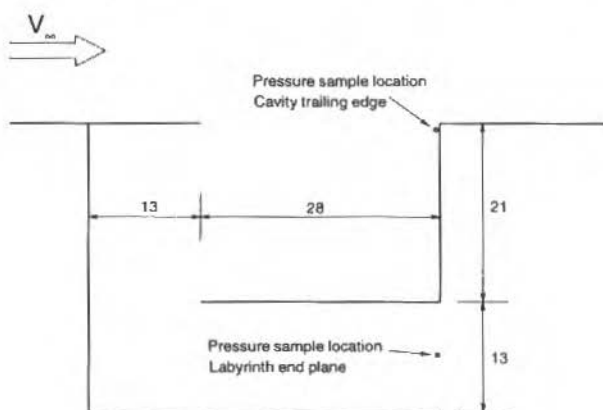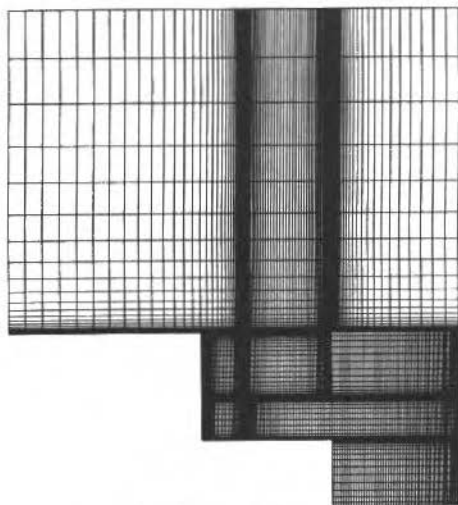

Fig.1   Configuration Geometry

Fig. 2   Computational Grid
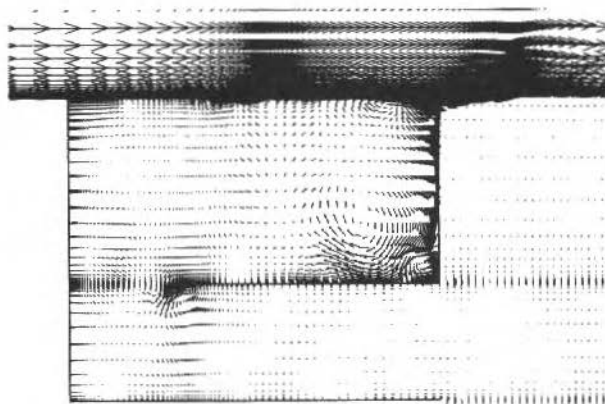
Fig. 3   Instantaneous Velocity Vectors

The shedding of vortices, and their subsequent convection downstream in the shear layer is observed. These small vortices merge with the larger vortical structures; the subsequent interaction of the vortical structures with the cavity rear wall generates pressure waves that propagate upstream. An animation of the cavity flow field showed that the shedding of these vortices was in phase with the arrival of pressure waves propagating upstream within the cavity. These upstream traveling pressure waves interact with the labyrinth wall and are reflected inside the labyrinth.

The time history of pressure at the rear cavity face and at the end plane of the labyrinth is presented in Fig. 5. It can be observed that the amplitude of the pressure oscillations is substantially attenuated for the position at the end plane of the labyrinth as compared with the rear cavity face position. The mean pressure and the differences between the instantaneous and mean pressure decrease from as much as 117% for the position at the rear cavity face to as much as 12% for the position at the end plane of the labyrinth. The mean value of the nondimensional pressure also decrease by a factor of 3%. The character of the time history is typical of that observed in self-sustained cavity flows.

t_1

$t_2 = t_1 + \Delta t$

$t_3 = t_1 + 2^* \Delta t$

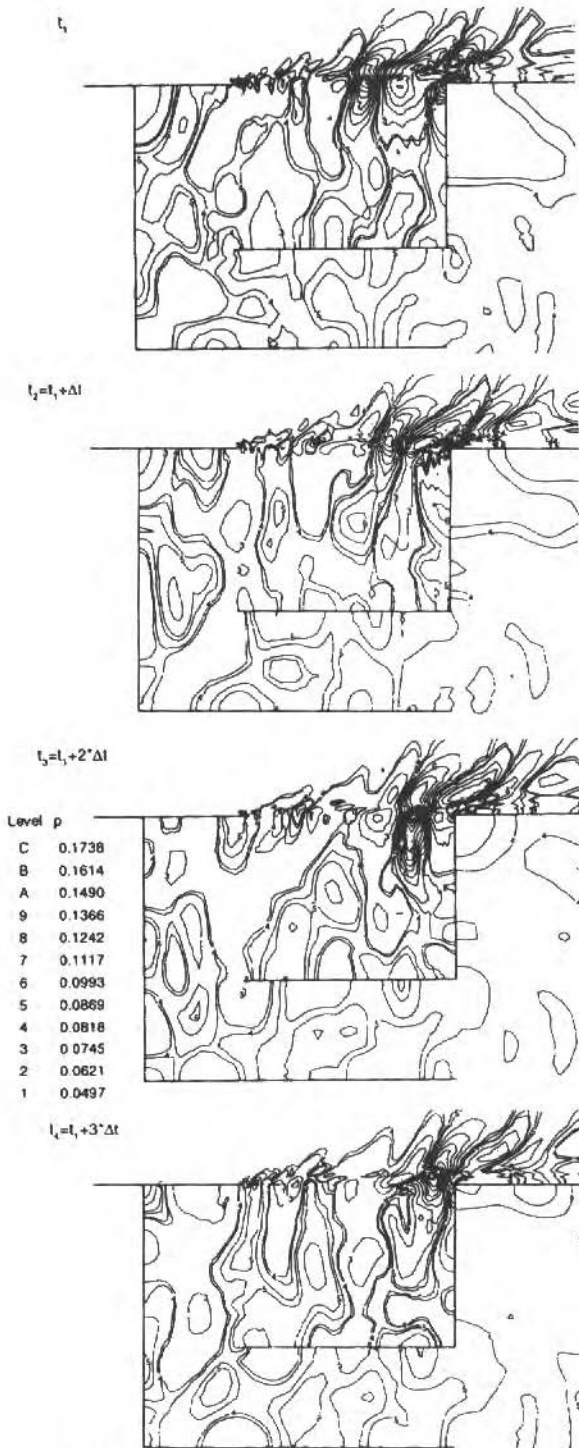| Level	ρ
C	0.1738
B	0.1614
A	0.1490
9	0.1366
8	0.1242
7	0.1117
6	0.0993
5	0.0869
4	0.0818
3	0.0745
2	0.0621
1	0.0497

$t_4 = t_1 + 3^* \Delta t$

Fig. 4 Instantaneous Pressure Contour Plots
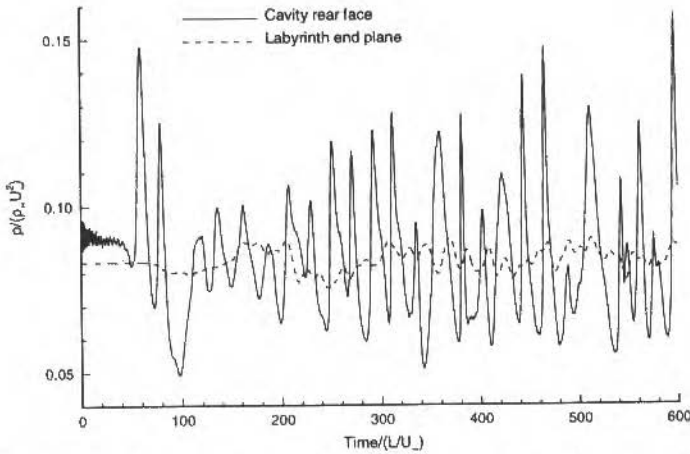
Fig. 5   Time History of Pressure at the Rear Face of the Cavity and at the End Plane of the Labyrinth

Spectral analysis of the unsteady pressure time histories was conducted using an algorithm based on the Maximum Entropy Method (Morgenstern, 1994). The frequency spectra of pressure data sampled at the rear face cavity lip and at the end plane of the labyrinth are presented in Fig. 6. The computed spectral results are compared with frequencies predicted by the modified semi-empirical formula of Rossiter (Heller and Bliss, 1975) shown in the figure by vertical dash-dot lines with the value of the predicted frequencies indicated. The computed spectra are in good agreement with the first four modes predicted by the semi-empirical formula. Overall it is observed the agreement is less good at the low frequency mode compared to the higher frequencies. The effect of the labyrinth on the sound pressure level calculated was to decrease its magnitude at the high frequency range. The reduction was of the order of 50 dB. The low frequency mode had its magnitude preserved and showed a small shift in frequency.

Fig. 6   Frequency Spectra of Sound Pressure Level at the Rear Face Cavity Lip and at the End of the Labyrinth

Conclusions

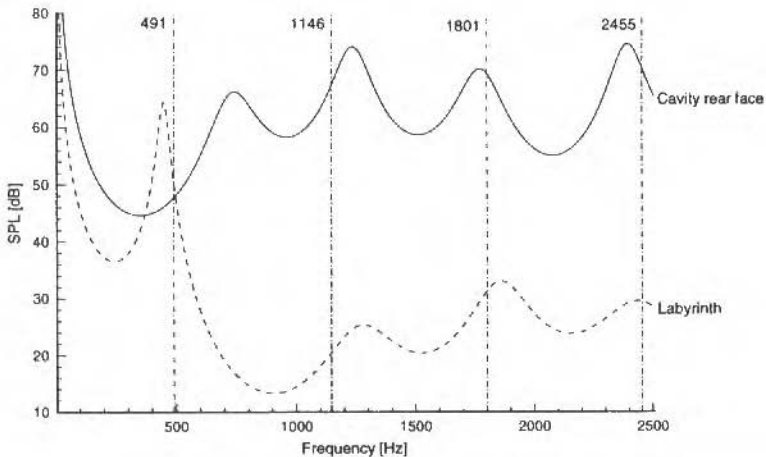A computational investigation of the supersonic flow past a pressure vent orifice with a labyrinth shaped geometry has been accomplished. Time-accurate solutions of the compressible Navier-Stokes equations have been obtained through the use of an implicit numerical algorithm; a subiteration procedure is implemented in the algorithm to achieve time-accuracy. The numerical code is readily vectorizable, may be run at large CFL numbers, and thus is suited to the conduct of parametric studies. For the case studied, self-sustained flow oscillations were observed. The amplitudes of the oscillations are observed to decrease due to the labyrinth geometry. These oscillations are associated with disturbances generated at the front of the cavity and pressure waves that propagate upstream from the rear of the cavity. This work is the first phase of an effort to examine pressure vent orifice flows. In subsequent work, different geometries will be studied, considering three-dimensional configurations.

Acknowledgments

References

Heller, H.H., and Bliss, D.B., 1975, "The Physical Mechanism of Flow-Induced Pressure Fluctuations in Cavities and the Concepts for their Suppression", AIAA 75-491.

Kim, I., and Chokani, N., 1992, "Navier-Stokes Study of Supersonic Cavity Flowfield with Passive Control", Journal of Aircraft, Vol. 29, pp. 217-223.

Matsuno, K., 1989, "A Time-Accurate Iterative Scheme For Solving the Unsteady Compressible Flow Equations", AIAA 89-1992CP.

Morgenstern, A., Jr., and Chokani, N., 1994, "Hypersonic Flow Past Open Cavities", AIAA Journal, Vol. 32, No.12, pp. 2387-2393.

Morgenstern, A., Jr., 1994, "Numerical Investigation of Unsteady Hypersonic Flows Past Cavities", Ph.D. thesis, North Carolina State University.

Rizzetta, D.P., 1988, "Numerical Simulation of Supersonic Flow Over a Three-Dimensional Cavity", AIAA Journal, Vol. 26, pp. 799-807.

Rogers, S.E., Kwak, D., and Kiris, C., Apr. 1991, "Steady and Unsteady Solutions of the Incompressible Navier-Stokes Equations", AIAA Journal, Vol. 29, pp. 603-610.

Yoon, S., and Kwak, D., 1992, "Implicit Navier-Stokes Solver for Three-Dimensional Compressible Flow", AIAA Journal, Vol. 30, pp. 2653-2659.

Análise da Influência do Bocal de Entrada no Comportamento Fluidodinâmico do Leito Pneumático com Alimentador Tipo Jorro

Fluid Dynamics Behavior of a Pneumatic Bed With a Spouted Bed Type Solid Feeding System

Elcio M.V. Silva
Maria do Carmo Ferreira
José T. Freire
Universidade Federal de São Carlos
Departamento de Engenharia Química
13565-905 - São Carlos, SP Brasil

Abstract

The fluid dynamics behavior of a pneumatic bed with a spouted bed type solid feeding system was investigated with measurements of voidages, solid velocities and pressure drop axial profiles. The flow was described by the two-phase unidimensional model for which either the drag coefficient, β, or the particle-wall friction force had to be estimated. The model was only successful if the β values were obtained from an empirical equation adjusted from experimental data. As for the particle-wall friction forces, the equation of Yang led to theoretical predictions for the voidages which were very close to the experimental values.
Keywords: Pneumatic Bed, Spouted Bed Type Solid Feeding System.

Resumo

O comportamento fluidodinâmico de um leito de transporte pneumático com alimentador tipo jorro foi investigado através da obtenção de dados de porosidade, velocidade de sólidos e perfis axiais de queda de pressão. As equações do modelo bifásico unidimensional foram aplicadas para a modelagem do sistema. Para a resolução do modelo é necessária a estimativa do coeficiente de arraste sólido-fluido (β) ou, alternativamente, da força de atrito entre a suspensão e a parede. Neste trabalho foi ajustada uma equação para a previsão de β a partir do coeficiente de arraste efetivo, C_d. O atrito sólido-parede foi estimado a partir de correlações propostas na literatura e o atrito fluido-parede através de uma equação empírica. As porosidades teóricas previstas pelo modelo foram comparadas com valores obtidos experimentalmente.
Palavras-chave: Transporte Pneumático, Alimentador Tipo Jorro.

Introdução

Conforme relatado em Ferreira e Freire (1992), a utilização de um sistema do tipo jorro para a alimentação de sólidos em um tubo de transporte pneumático apresentou algumas características vantajosas em relação aos sistemas tradicionalmente utilizados. A principal delas é a possibilidade de transporte de sólidos em uma ampla faixa de vazões, o que pode ser obtido variando-se a distância entre a extremidade inferior do tubo de transporte e a entrada de ar no leito (denominada distância z_0). A caracterização fluidodinâmica efetuada indicou, entretanto, a ocorrência de instabilidades no escoamento, que se traduziam em oscilações nas colunas de fluido dos manômetros conectados ao longo do tubo de transporte pneumático. Observou-se também que o equipamento não apresentava boa reprodutibilidade, dificultando a obtenção de dados experimentais. Na tentativa de melhorar as condições operacionais do leito, foram efetuados testes utilizando-se um bocal de redução tipo venturi na região de alimentação de ar do sistema. Os efeitos da utilização deste bocal no comportamento fluidodinâmico do leito serão analisados neste trabalho a partir de dados experimentais e da aplicação do modelo bifásico unidimensional.

Formulação Teórica. A análise fluidodinâmica do transporte pneumático vertical em fase diluída é formulada a partir de equações diferenciais de balanço de massa e quantidade de movimento, escritas para cada uma das fases envolvidas, segundo o modelo clássico proposto por Capes e Nakamura (1973). As equações da continuidade para as fases fluida e sólida são dadas por:

$$\frac{d}{dz}(\varepsilon \rho_f u) = 0 \tag{1}$$

$$\frac{d}{dz}((1-\varepsilon)\rho_p v) = 0 \tag{2}$$

Nas equações acima ε é a porosidade da suspensão; u e v são as velocidades intersticiais das fases fluida e sólida, z é a direção do escoamento e ρ a densidade, sendo que os índices f e p serão utilizados para designar fluido e partícula. As equações do balanço de quantidade de movimento para as fases fluida e sólida são:

$$\frac{d[\rho_f u^2 \varepsilon]}{dz} - \varepsilon\left(-\frac{dp}{dz}\right) + \varepsilon \rho_f g + \beta(u-v)^2 + F_f = 0 \tag{3}$$

$$\frac{d[\rho_p v^2(1-\varepsilon)]}{dz} - (1-\varepsilon)\left(-\frac{dp}{dz}\right) + (1-\varepsilon)\rho_p g - \beta(u-v)^2 + F_p = 0 \tag{4}$$

onde p é a pressão na linha, g a aceleração da gravidade, F_f corresponde à perda por atrito da fase fluida na ausência de partículas e F_p corresponde ao atrito da fase sólida. Admite-se que a força de arraste é proporcional ao quadrado da velocidade relativa entre gás e partículas, sendo que o coeficiente de arraste, β, representa esta constante de proporcionalidade. As equações de balanço individuais podem ser combinadas em uma única equação, que representa o balanço para a mistura:

$$\frac{d}{dz}(\rho_f \varepsilon u^2) + \frac{d}{dz}[\rho_p(1-\varepsilon)v^2] = -\frac{dp}{dz} - [(1-\varepsilon)\rho_p + \varepsilon\rho_f]g - F_w \tag{5}$$

onde a perda por atrito entre a suspensão e a parede do tubo é $F_w = F_p + F_f$.

Considerando como incógnitas as variáveis u, v, ε e p, as dificuldades envolvidas na solução deste sistema referem-se à obtenção de equações constitutivas confiáveis para a previsão do coeficiente de arraste entre as fases, β e para a força de atrito F_p. Apesar de existirem controvérsias, diversos autores (Littman, 1993, Mendonça e Massarani, 1994) consideram que no escoamento em regime diluído o atrito sólido-parede pode ser desprezado e na modelagem é considerado apenas o atrito fluido-parede.

No transporte pneumático em regime diluído, fora da região de entrada, o coeficiente de arraste β pode ser relacionado ao coeficiente de arraste efetivo através da equação:

$$C_d = \frac{4}{3(1-\varepsilon)}\left(\frac{\beta d_p}{\rho_f}\right) \tag{6}$$

Diversas correlações empíricas ou semi-empíricas são propostas na literatura para previsão de C_d em suspensões gás-sólido (Lee, 1987, Grbavcic et al, 1991). Os dados experimentais utilizados na obtenção destas equações entretanto são fortemente influenciados pelas condições experimentais em que foram obtidos e envolvem a adoção de simplificações que nem sempre foram verificadas experimentalmente. Isto torna sua aplicabilidade bastante restrita para condições operacionais que não sejam similares às dos sistemas utilizados originalmente.

Metodologia

Equipamento. O leito de transporte pneumático com alimentador tipo jorro utilizado neste trabalho é mostrado esquematicamente na Fig. 1. O tubo de transporte é de ferro galvanizado, com diâmetro interno igual a 53,4 mm e 3,6 m de altura. O ar é fornecido ao sistema por um soprador de 7,5 HP. Como fase sólida utilizou-se esferas de vidro, com diâmetro médio de partícula d_p = 1,0 mm e densidade igual a 2.503 m³/min. Sete tomadas de pressão (2), conectadas a manômetros de tubo em U
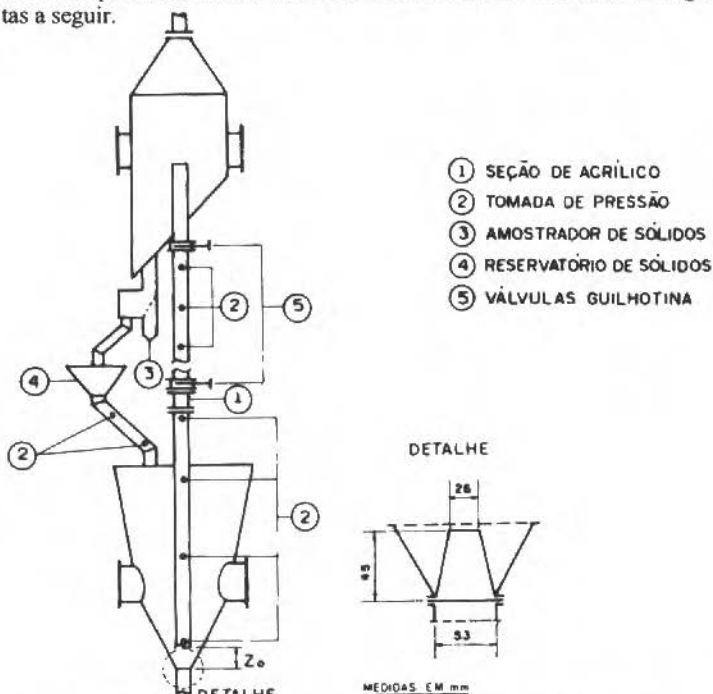
foram distribuídas ao longo do comprimento do tubo para obtenção de perfis axiais de pressão. A determinação da vazão mássica de sólidos foi efetuada desviando-se a direção do escoamento e coletando-se os mesmos no amostrador (3). A vazão de ar alimentada foi determinada com o auxílio de um medidor tipo venturi, e a vazão desviada para o reciclo foi obtida a partir de medidas da queda de pressão no tubo (mantido sempre cheio durante a operação). A vazão no tubo de transporte foi então obtida a partir de um balanço de massa que considerava estes dois termos. Duas válvulas tipo "guilhotina"(5) com acionamento pneumático foram instaladas no tubo, separadas por uma distância de 1,32 m. O acionamento simultâneo das válvulas interrompia o escoamento da suspensão. Os sólidos retidos no interior do tubo eram succionados com o auxílio de uma bomba de vácuo e a porosidade média era determinada a partir da massa de sólidos coletada. O tubo de transporte pode ser deslocado axialmente, permitindo a variação da distância entre sua extremidade inferior e a entrada de ar no sistema (distância z_0 indicada na Fig. 1). O bocal redutor, cujas dimensões são mostradas na Fig. 1, foi instalado na base cônica do leito, acima da entrada de ar. Na Tabela 1 são apresentados os erros das medidas experimentais, estimados segundo o método de Kline e McClintok citado em Holman (1978).

Tabela 1   Erros Estimados Para as Medidas Experimentais

Grandeza	Erro (%)
Veloc. Sup. Gás (m^3/min)	±0,92
Veloc. Sup. Sólido (kg/s)	±2,05
Porosidade *	±0,15
dP/dz (Pa/m)	±3,37

* Erro do processo de medição, estimado estatisticamente (Montgomery, 1991).

Método. Os valores experimentais de porosidades médias obtidos fora da região de aceleração serão comparados com valores previstos pelas equações do modelo bifásico unidimensional. Os dados de porosidades experimentais foram obtidos para diferentes velocidades de gás no tubo de transporte, e para três diferentes distâncias z_0:3,4; 4,7 e 6,0 cm. Embora as equações diferenciais que constituem a base do modelo sejam idênticas, as porosidades teóricas foram obtidas através de duas metodologias diferentes, que serão descritas a seguir.

① SEÇÃO DE ACRÍLICO
② TOMADA DE PRESSÃO
③ AMOSTRADOR DE SÓLIDOS
④ RESERVATÓRIO DE SÓLIDOS
⑤ VÁLVULAS GUILHOTINA

DETALHE

MEDIDAS EM mm

Fig. 1   Representação do Leito Pneumático com Alimentador Tipo Jorro e Bocal Reduto Utilizado

Metodologia (I). Fora da região de aceleração, os termos referentes aos gradientes de porosidade e velocidades são eliminados nas Eqs. (1) a (5) e o gradiente de pressão no tubo de transporte é constante. Este gradiente foi determinado para cada condição experimental, tomando-se a porção linear das curvas de quedas de pressão medidas em função da distância axial. A fim de eliminar o problema da determinação da força de atrito sólido-parede, utilizou-se a equação do balanço de quantidade de movimento do fluido (Eq. 3), cuja solução em ε é iterativa, para a determinação da porosidade teórica. Observa-se que a variação de pressão ao longo do comprimento do tubo de transporte é pouco significativa, e os valores de pressão absoluta foram no máximo 2% superiores à pressão atmosférica. Assim, utilizou-se nos cálculos a densidade do ar estimada a 1 atm e temperatura de 80°C, o valor médio de temperatura medido na linha de alimentação. Foi ajustada uma equação empírica para a estimativa de C_d, em função do número de Reynolds de partícula, $Re_p = d_p(u-v)/v_f$:

$$C_d = \frac{459,29}{Re_p^{1,102}}; \quad 374 < Re_p < 741 \tag{7}$$

Para o ajuste desta equação foram utilizados dados experimentais obtidos para uma distância z_0=6,0 cm. Os coeficientes foram ajustados pelo método dos mínimos quadrados, com um coeficiente de ajuste R^2 = 74,89%. Valores experimentais de β foram determinados pela Eq. (7). Observa-se que para o sistema de alimentação utilizado, a velocidade de transporte dos sólidos é função da distância z_0 e da velocidade do gás. Foi utilizada a técnica de superfície de resposta de Myers (1976) para ajustar uma equação empírica para a previsão da velocidade superficial dos sólidos, tendo sido obtida a seguinte expressão:

$$V = 6,53 \cdot 10^{-3} + 8,84 \cdot 10^{-3}x_1 + 4,31 \cdot 10^{-3}x_2 + 1,01 \cdot 10^{-3}x_1x_2 +$$
$$3,97 \cdot 10^{-3}x_1^2 + 1,65 \cdot 10^{-3}x_2^2 \tag{8}$$

onde $V=(1-\varepsilon)v$ é a velocidade superficial dos sólidos; $x_1 = (0,77z_0 - 3,62)$ e $x_2 = (1,79Q_{ar} - 3,83)$, com z_0 dado em cm e Q_{ar} (vazão volumétrica do ar) em m^3/min. O coeficiente de ajuste desta equação foi R^2 = 99,83%.

A perda por atrito fluido-parede, F_f, também foi obtida empiricamente, a partir de uma equação ajustada usando dados de queda de pressão medidos para o escoamento da fase fluida. Para o cálculo das porosidades teóricas, o procedimento consistiu em resolver a Eq. (3) iterativamente utilizando-se as equações ajustadas como equações constitutivas. Visando efetuar uma comparação com equações propostas na literatura para estimativa do coeficiente de arraste, o mesmo procedimento descrito foi repetido utilizando-se a equação do modelo variacional proposta por Grbavcic et al. (1991) para a previsão do coeficiente β. A correlação proposta pelos autores é função de parâmetros de mínima fluidização do sistema. No caso deste trabalho, tais parâmetros foram obtidos experimentalmente, tendo sido obtidos os valores de 1,0 m/s e 0,42 respectivamente, para a velocidade e porosidade de mínima fluidização. A terceira equação utilizada para a estimativa de C_d foi a correlação proposta por Lee (1987). Este autor admitiu ser válida para o escoamento de suspensão diluída em regime turbulento, uma pseudo lei de Stokes, dada pela equação:

$$C_d = \frac{24}{Re_{pc}} \frac{\bar{v}_f}{v_f} \tag{9}$$

onde Re_{pc} é o número de Reynolds da partícula na posição correspondente ao centro do tubo e $\bar{v}_f$ é a viscosidade cinemática turbulenta. Re_{pc} foi estimado admitindo-se que o perfil radial de velocidade do gás segue a lei 1/10 de potência e que a velocidade do sólido é praticamente constante radialmente (Lee e Durst, 1982). A viscosidade turbulenta foi estimada pela correlação proposta em Lee (1987).

Metodologia (II). A equação do balanço de quantidade de movimento para a mistura (Eq. 5) foi utilizada para a obtenção da porosidade. O coeficiente de atrito partícula-parede foi estimado a partir da correlação proposta por Yang (1978).

$$f_p \frac{\varepsilon^3}{(1-\varepsilon)} = 0,0126\left[(1-\varepsilon)\frac{Re_t}{Re_p}\right]^{-0,979} \tag{10}$$

onde Re_t é o número de Reynolds calculado com a velocidade terminal, estimada através da correlação sugerida por Haider e Levenspiel (1989). A força de atrito foi então calculada admitindo que vale uma relação funcional análoga a de Fanning e somada à força de atrito fluido-parede para a obtenção de F_w. Foram testadas também as correlações de Konno e Saito (citada em Leung, 1980) e de Capes e Nakamura (1973) para previsão de F_p. Num procedimento análogo ao descrito anteriormente, a Eq. (5) foi resolvida iterativamente em ε. A seguir serão apresentados os principais resultados obtidos.

Resultados

A introdução do bocal na entrada de ar provocou uma alteração significativa no comportamento fluidodinâmico do leito. Pelo fato de criar uma zona de vácuo na entrada do tubo de transporte, a vazão de ar que escoa através da região anular é minimizada. Eliminou-se, portanto, a necessidade do escape de ar que existia anteriormente (Silva et al., 1994) e o equipamento passou a apresentar uma excelente reprodutibilidade para as condições experimentais. As vazões de sólidos transportadas diminuíram em comparação com a vazões transportadas na ausência do bocal. Este comportamento se justifica pela diminuição da área livre na base do tubo, o que resulta em uma resistência adicional à alimentação dos sólidos. Com a diminuição da vazão de sólidos, obtém-se uma suspensão diluída e uniforme e a ausência de oscilações das colunas de fluido dos manômetros comprova que as instabilidades anteriormente observadas no escoamento deixaram de existir. Constatou-se também que o aumento da velocidade do gás na entrada do leito provocado pela introdução do bocal incrementa a transferência de quantidade de movimento nesta região, e reduz significativamente o comprimento da região de aceleração das partículas. Na Tabela 2 são mostrados alguns dados ilustrativos obtidos para os sistemas com e sem bocal.

Tabela 2   Dados Comparativos dos Sistemas com e sem Bocal para $z_0 = 6,0$ cm

	W_p (kg/s)	L_e (m)
s/bocal	0,408-0,535	1,46
c/ bocal	0,090-0,113	0,35

w_p - vazão mássica de sólidos; L_e - comprimento de aceleração

Os valores experimentais de porosidade obtidos com a utilização do bocal variaram entre 0,9949 e 0,9992, o que indica escoamento em regime diluído para todas as condições operacionais testadas. O modelo bifásico para escoamento em regime diluído foi aplicado inicialmente segundo o procedimento descrito como Metodologia I. Na Fig. 2 são mostrados os dados experimentais de porosidade obtidos em função dos valores teóricos calculados.
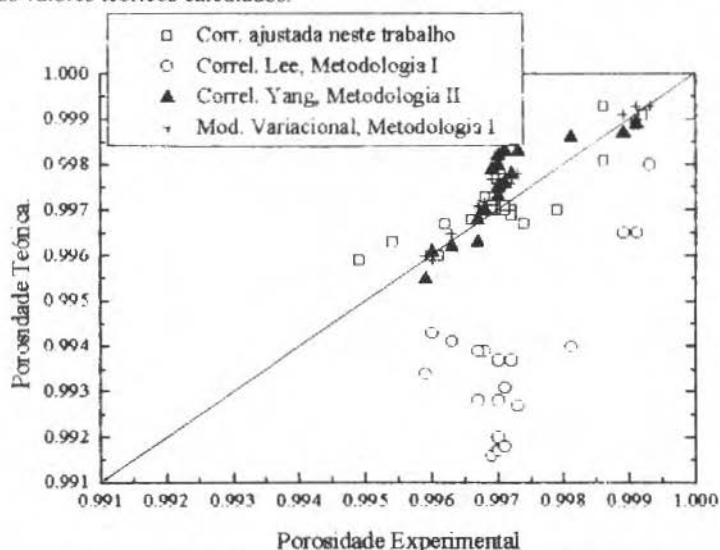
Fig. 2   Comparação entre as Porosidades Experimentais e Teóricas

Os desvios entre os valores experimentais e calculados utilizando-se a correlação ajustada neste trabalho estão uniformemente distribuídos em torno da linha de 45° e variaram entre 0,002 e 0,10%, indicando o bom ajuste do modelo. Com a utilização da correlação de Lee, o ajuste foi menos satisfatório. Os desvios entre os valores teóricos e experimentais foram significativamente maiores, variando entre 0,14 e 0,62%, superiores portanto ao erro experimental. Além disto, os valores teóricos de porosidade estão sendo consistentemente subestimados em relação aos valores experimentais. A provável explicação para este comportamento é o fato de Lee não ter considerado o atrito partícula-parede na obtenção de sua correlação para previsão da viscosidade turbulenta. Os dados utilizados no ajuste da equação foram obtidos a partir de valores experimentais de C_d. A definição utilizada para o coeficiente de arraste, entretanto, admite partículas com velocidade constante, uma suposição que deixa de ser válida quando existem colisões entre as partículas e a parede (Lee, 1990). Esta observação nos permite supor que o atrito partícula-parede não deve ser desprezível, mesmo para transporte pneumático em fase diluída. Com o objetivo de verificar esta hipótese, a força de atrito partícula-parede foi determinada experimentalmente para o sistema em estudo a partir da Eq. (5). Foram utilizados nesta determinação os dados experimentais de porosidade, gradiente de pressão e força de atrito fluido-parede. Os valores obtidos para F_p variaram entre 10 e 149 Pa/m, enquanto F_f ficou entre 22 e 123 Pa/m. Constata-se, portanto, que a ordem de grandeza das forças são comparáveis, o que confirma a suposição de que o termo referente ao atrito partícula-parede não deve ser desprezado na modelagem fluidodinâmica.

Os valores teóricos de porosidade obtidos utilizando a correlação de Yang através da Metodologia II também mostraram excelente concordância entre os valores experimentais. Os desvios ficaram entre 0,008 e 0,15%, portanto dentro do erro experimental. Segundo Leung (1980), as correlações de Yang e de Konno e Saito são as que fornecem melhores ajustes para F_p em relação aos dados experimentais publicados na literatura. No caso deste trabalho, a equação de Yang foi a que forneceu melhores resultados, embora com tendência a superestimar as previsões, especialmente para valores elevados de F_p. Embora a equação de Konno e Saito também tenha sido testada, verificou-se que ela subestimava F_p em relação aos dados experimentais, sendo que os valores de porosidade previstos pelo modelo apresentaram desvios maiores do que o erro experimental. Convém observar também que a utilização desta correlação implicaria na obtenção de valores subestimados para o gradiente de pressão na linha. Já a correlação de Capes e Nakamura (1973) fornecia valores de F_p superestimados em relação aos dados experimentais, resultando em previsões ruins de porosidade.

Conclusões

A utilização de um bocal de redução na alimentação do gás do leito de transporte pneumático com alimentador tipo jorro melhora a estabilidade fluidodinâmica do escoamento, reduz o comprimento de aceleração do leito e garante a reprodutibilidade das condições experimentais. O modelo bifásico unidimensional forneceu excelentes resultados para a previsão da porosidade do sistema, com a utilização de uma equação ajustada para a previsão de C_d. Os dados experimentais indicaram que a força de atrito sólido-parede é significativa no escoamento em regime diluído. A utilização do balanço de quantidade de movimento para a mistura na modelagem fluidodinâmica forneceu bons resultados utilizando-se a correlação de Yang (1978) para a previsão do fator de atrito sólido-parede.

Agradecimentos

Referências

Capes, C.E., e Nakamura, K., 1973, "Vertical Pneumatic Conveying: An Experimental Study ...", Can. J. Chem. Eng., Vol. 51, pp. 31-38.
Ferreira, M.C., e Freire, J.T., 1992, "Fluid Dynamics Characterization of a Pneumatic Bed Using a Spouted Bed Type Solid Feeding System", Can. J. Chem. Eng., Vol. 70, pp. 905-909.

Grbavcic, Z.B. et al., 1991, "Variational Model for Prediction of the Fluid-Particle Interphase Drag Coefficient ...", Powder Technol., Vol. 68, pp. 199-211.

Haider, A., e Levenspiel, O., 1989, "Drag Coefficient and Terminal Velocity of Spherical and Non-Spherical Particles", Powder Technol., Vol. 58, pp. 63-70.

Holman, J.P., 1978, "Experimental Methods for Engineers", Mc Graw Hill, New York.

Lee, S.L., 1987, "Particle Drag in a Dilute Turbulent Two-Phase Suspension Flow", Int. J. Multiphase Flow, Vol. 13, No. 2, pp. 247-256.

Lee, S.L., 1990, "Discussion of Particle Drag in a Dilute Turbulent Two-Phase Suspension Flow", Int. J. Multiphase Flow, Vol. 16, No. 2, pp. 359-361.

Lee, S.L., e Durst, L., 1982, "On the Motion of Particle in Turbulent Duct Flows", Int. J. Multiphase Flow, Vol. 8, No. 2, pp. 125-146.

Leung, L.S., 1980, "The Ups and Downs of Gas-Solid Flow - A Review", in Fluidization, (eds. J.R. Grace e J.M. Matsen), Plenum Press, New York, pp. 25-68.

Littman, H. et al., 1993, "Modelling and Measurement of the Effective Drag Coefficient in Decelerating and Non-Accelerating Turbulent Gas-Solids ...", Powder Technol., Vol.77, pp. 267-283.

Mendonça, K.C.P., e Massarani, G., 1994, "Estudo da Fluidodinâmica de Sistemas de Leito Fluidizado Circulante", Anais do XXII Encontro Sobre Escoamento em Meios Porosos, no prelo, Florianópolis, SC, Brasil.

Myers, R.H., 1976, "Responce Surface Methodology", Ann Arbor, Mich.: Edwards Brothers (distrib.), Virginia.

Silva, E.M.V., Ferreira, M.C., e Freire, J.T., 1994, "Determinação da Porosidade no Leito Pneumático com Alimentador Tipo Jorro", Anais do XXII Encontro Sobre Escoamento em Meios Porosos, no prelo, Florianópolis, SC, Brasil.

Yang, W.C., 1978, "A Correlation for Solid Friction Factor in Vertical Pneumatic Conveying Lines", AIChE Journal, Vol. 24, No. 3.

Inertial Effects on the Retention of Particles in the Near Wake of Blunt Obstacles

Marcos Sebastião de Paula Gomes

Pontifícia Universidade Católica do Rio de Janeiro
Departamento de Engenharia Mecânica
22453-900 - Rio de Janeiro, RJ Brasil

Abstract

This work examines the dispersion of particles in the flow around a blunt obstruction. The investigation involved the development of a numerical procedure based on the k- ε model for turbulence and an Eulerian approach for taking into account the inertial behavior of the particle.
Keywords: Dispersion of Particles, Wake of Blunt Obstacles, Inertial Effects.

Introduction

The investigation of particle dispersion in turbulent distorted flows is of great relevance to various applications. This may include the design and optimization of air cleaning devices, the environmental control of the particle dispersion phenomena in small (e.g. in the work environment and in clean rooms) and in large scales (e.g. atmospheric pollution), aerosol related manufacturing processes, aerosol sampling and transport (e.g. samplers development), among others.

This work describes a simple numerical model for solving problems of particle dispersion in flows around obstructions. We set out to investigate the dispersion of particles in the near wake region of a long two-dimensional flat plat positioned perpendicular to the incoming flow. The geometry of the problem is presented in Fig. 1, below.
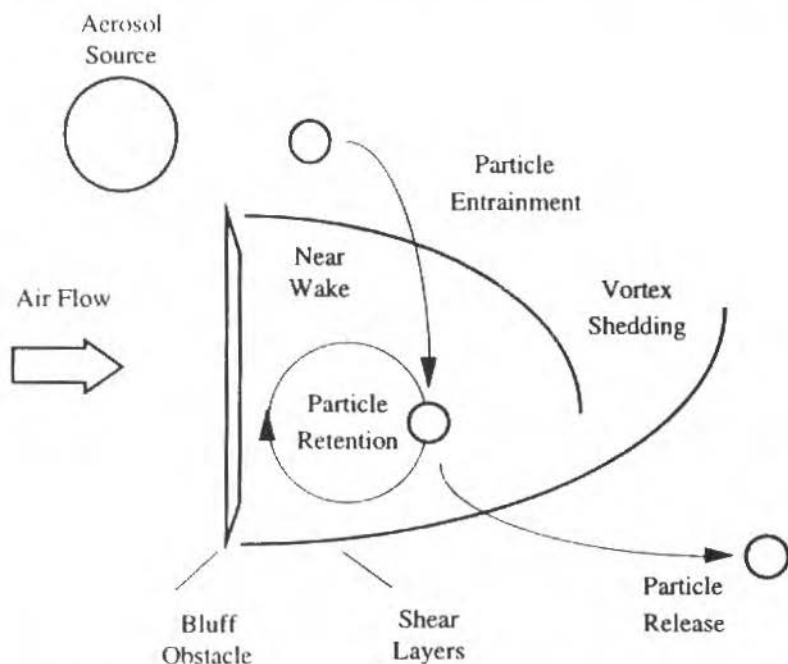

Fig. 1 Geometry to be Investigated, Indicating the Mechanisms of Particle Retention and Release in the Near Wake Region Behind the Blunt Obstacle

Our main concern here is to look at the effect of inertia on the residence time for particles in the near wake region of the bluff body after a source for the aerosol in the neighborhood of the obstacle has been suddenly removed. Due to the recirculation zone behind the obstacle, particles may entrain in that region and stay there for a long time, even after cessation of the aerosol generation process. The investigation involved the prediction of the concentration decay in the near wake region. We will start with a description of the governing equations for the fluid motion, the modeling of turbulence, and the treatment of the unsteady concentration problem. We will next examine the influence of particle inertia on the dispersion process.

Numerical Model

In developing a model that could be easily applied, we solved the flow as if it were steady. We were mainly interested in the time averaged solution for the flow, therefore, we expected the model to provide reasonable results. It also should be mentioned that gravitational effects were neglected. We solved the time averaged Continuity and Momentum Equations:

$$\frac{\partial \bar{u}_i}{\partial x_i} = 0$$

$$\rho \frac{\partial (\bar{u}_i \bar{u}_j)}{\partial x_j} = -\frac{\partial \bar{P}}{\partial x_i} + \frac{\partial}{\partial x_j}\left((\mu + \mu_t)\frac{\partial \bar{u}_i}{\partial x_j}\right) + \frac{\partial}{\partial x_j}\left(\mu_t \frac{\partial \bar{u}_j}{\partial x_i}\right)$$

$$\bar{P} = \bar{p} + \frac{2}{3}\rho k, \text{ and } k = \frac{1}{2}\left(\overline{u'_i u'_i}\right)$$

(1)

Due to the combination of simplicity and reasonably good prediction capabilities, the k-ε model was the one of choice for the calculation of the turbulent viscosity. We then solved the Kinetic Energy and Dissipation Equations:

$$\frac{\partial (\rho \bar{u}_i k)}{\partial x_i} = \frac{\partial}{\partial x_i}\left(\frac{\mu_t}{\sigma_k}\frac{\partial k}{\partial x_i}\right) + G - \rho\varepsilon$$

$$\frac{\partial (\rho \bar{u}_i \varepsilon)}{\partial x_i} = \frac{\partial}{\partial x_i}\left(\frac{\mu_t}{\sigma_\varepsilon}\frac{\partial \varepsilon}{\partial x_i}\right) + (c_1 G - c_2 \rho\varepsilon)\frac{\varepsilon}{k}$$

(2)

$$G = \mu_t\left(\frac{\partial \bar{u}_i}{\partial x_j} + \frac{\partial \bar{u}_j}{\partial x_i}\right)\frac{\partial \bar{u}_j}{\partial x_i}, \text{ and } \mu_t = \frac{c_\mu \rho k^2}{\varepsilon}$$

The values that are recommended for the constants that appear in the above equations are $c_\mu = 0.09$, $c_1 = 1.44$, $c_2 = 1.92$, $\sigma_k = 1.0$, $\sigma_\varepsilon = 1.3$ (Patankar, 1990). The last two are called the turbulent Prandtl numbers for kinetic energy and dissipation, respectively. Much discussion exist with respect to the final values the five constants should have. In a recent paper by Rodi and Mansour (1993), it was concluded that the coefficient c_μ should depend on the type of flow and on the Reynolds number, and may vary from 0.07 to 0.12 in the bulk of the flow. They recommended that the usual constant value of 0.09 should not be used for all situations. In an experimental and numerical investigation regarding the dispersion of inertialess particles around a bluff body (Gomes, 1994), it was found that better agreement between experimental and numerical data was obtained for $c_\mu = 0.12$.

Turning our attention to the particle dispersion problem, we would like to investigate the rate of change for the particle concentration in the near wake region, for the special case in which a source for particles in the neighborhood of the blunt obstacle is suddenly removed. Our purpose is to develop a model for studying the effect of particle inertia in the dispersion phenomenon. The particles will usually have a velocity that is different from the velocity of the fluid. There are two approaches for solving the problem. In the first one, an equation representing the balance of forces acting on each particle (e.g. drag, lift, and time-history forces, among others) is integrated over time to obtain the trajectory of the particle. Trajectories should be calculated for particles released from different

locations in the domain (if the flow is steady) and also from the same location at different times (if the flow is unsteady). A statistical method may be used for combining the information regarding the different trajectories crossing a defined region in space, during a certain interval of time, into particle number concentration. This procedure corresponds to the Lagrangian description of the particle dispersion problem and could be computationally intensive and very time consuming. The second approach deals with the solution of the particle concentration equation considering distinct values for the particle diffusivity, depending on the inertial behavior of the particle. This treatment corresponds to the Eulerian description of the dispersion phenomenon, and it was the procedure of choice in the present work. We solved the unsteady particle concentration equation:

$$\frac{\partial C}{\partial t} + \frac{\partial (u_i C)}{\partial x_i} = \frac{\partial}{\partial x_i}\left(\frac{v_t}{\sigma_c}\frac{\partial C}{\partial x_i}\right) + S_c \tag{3}$$

Where C is the particle number concentration and σ_C is the turbulent Schmidt number, defined as the ratio between the eddy viscosity (turbulent diffusivity for momentum) and the apparent turbulent particle diffusivity. For particles that perfectly follow the flow it is recommended that: for boundary layers on walls σ_C should be set equal to 0.9, while for free jets and wakes the value of 0.5 is more appropriate (Patankar, 1990). In our previous work (Gomes, 1994) it was found that better results for the near wake dispersion of inertialess particles were obtained for $\sigma_C = 0.4$.

As a summary of the proposed model so far, it reduces to (a) solving the turbulent and steady (time averaged) flow of air with constant properties around an obstruction; and (b) solving the unsteady particle dispersion problem superimposed on the obtained velocity field. This uncoupled nature between flow and particle concentration problems is a result of the low concentration and small size of the particles. They do not interfere with the flow conditions.

The above set of equations was solved by using both the SIMPLER and the SIMPLE procedures developed by Patankar (1980). The first one was implemented in a code specifically written for the solution of the problem, the second one was employed as part of the commercial code FLUENT. To avoid instabilities and improve convergence in the solution, an under-relaxation factor of 0.5 was applied to all dependent variables. The concentration decays were observed down to less than 0.1% of the initial value.

The Consideration of Inertial Effects

The transport of large particles in a turbulent flow can be substantially different than that for fine inertialess particles. According to Soo (1967), the first analytical formulation of the problem related to the motion of a suspended particle in a turbulent flow was done by Tchen in 1947. At that time there was a recognition that, due to particle inertia, the particle trajectories were not the same as the fluid streamlines. However, among several other simplifications that were made in his analysis, Tchen also assumed that during its motion the particle remained within the same eddy. This required the particle paths and flow streamlines to be very similar, a rather restrictive assumption.

According to Soo (1967), a less restrictive theory than the one developed by Tchen, taking into account the possibility of different trajectories for particles and fluid elements, was developed by Peskin in 1962. Peskin found that the ratio between particle diffusivity and eddy diffusivity was a function of the particle response time and of the flow Eulerian and Lagrangian micro-scales. The relationship could be written according to:

$$\frac{D_p}{D_f} = 1 - \left(\frac{\lambda_L}{\lambda_E}\right)^2\left(\frac{3\Psi^2}{\Psi + 2}\right) + O\left(\frac{1}{\lambda_E^4}\right) \tag{4}$$

where Ψ, the particle impulse response parameter, is given by:

$$\Psi = \frac{\sqrt{\pi}\rho_p d_p^2}{18}\frac{\overline{(u'^2)}^{1/2}}{\mu}\frac{1}{\lambda_L} \tag{5}$$

The quantity Ψ represents the inertial parameter for a particle following the turbulent fluctuations. In the above expressions, D_p and D_f are the particle and fluid diffusivities, λ_L and λ_E are the Lagrangian and Eulerian micro-scales, d_p is the particle diameter, μ is the absolute viscosity of the fluid, and ρ_p is the particle density.

Physically, Peskin's results were interpreted in the following way:

(a) for a fixed value of the ratio between the micro-scales, if $\Psi = 0$ the particle perfectly follows the flow and the ratio D_p/D_f should be equal to 1, while if Ψ is very large the particle does not respond at all to the turbulent motion, and so $D_p/D_f=0$.

(b) for a finite value of Ψ, suggesting that the particle may not perfectly follow the fluid, if λ_L/λ_E is small there is a strong correlation between fluid elements at neighboring locations so that, even if the particle does not follow the fluid, it will encounter different elements with similar internal velocities. The net result will be that D_p tends towards D_f. When λ_L/λ_E is large, the particle will traverse through uncorrelated neighboring fluid elements and will experience different fluid velocities, what will tend to produce a small particle diffusivity. As a result of this picture, the ratio D_p/D_f will be always less than or equal to 1.

Instead of using the above format for the inertial parameter, it will be more convenient to express the particle inertial behavior through a Stokes number for the mean flow, or:

$$\text{Stk} = \frac{1}{18}\frac{\rho_p d_p^2}{\mu}\frac{U}{D} \tag{6}$$

where U and D are the free-stream velocity and the characteristic dimension of the bluff obstacle, respectively. The Stokes number can be interpreted as the ratio between the particle relaxation time (or the time it takes for the particle to relax or to adjust its velocity to a new set of external conditions) and a time scale related to the flow distortion (e.g. D/U). The Stokes number, as defined above, is related to the properties of the mean flow and to the external or integral scales of turbulence in the near wake cavity.

The relationship between Ψ and Stk may then be written as:

$$\frac{\Psi}{\text{Stk}} = \sqrt{\pi}\frac{(\overline{u'^2})}{\lambda_L}\frac{U}{D} = \sqrt{\pi}\frac{D}{\lambda_L}I \tag{7}$$

where I is the turbulence intensity. Assuming that D is of the order the Eulerian integral scale in the near wake region, we may write:

$$D \sim \frac{\sqrt{\pi}}{2}\lambda_E \tag{8}$$

The above equation is an approximation for the relationship between the Eulerian integral and micro-scales and should not be taken as definite (Hinze 1987). In fact, the investigation of relationships between the turbulence scales still represents a challenge. After neglecting higher order terms, the ratio of particle to fluid diffusivity may be written as a function of the mean flow Stokes number, the local turbulence intensity and the ratio between the Eulerian and Lagrangian micro-scales:

$$\frac{D_p}{D_f} \sim 1 - \frac{3\left(\frac{\pi}{2}I\cdot\text{Stk}\right)^2}{\frac{\pi}{2}I\cdot\text{Stk}\frac{\lambda_E}{\lambda_L} + 2} \tag{9}$$

Results

Figure 2 below shows a plot of the diffusivities ratio D_p/D_f as a function of the Stokes, number, for a few values of the turbulence intensity I and the ratio between the Lagrangian and Eulerian microscales $\lambda_L \lambda_E$. Soo (1967) pointed out that higher-order calculations should indicate that the curves become asymptotic to the x axis for small values of D_p/D_f, according to the expected decrease in

particle diffusivity, with D_p tending towards zero for increasing Stokes numbers. The plot also demonstrates that for the same Stk, an increase in turbulence intensity or in the ratio λ_L / λ_E, both cause a reduction in D_p/D_f.
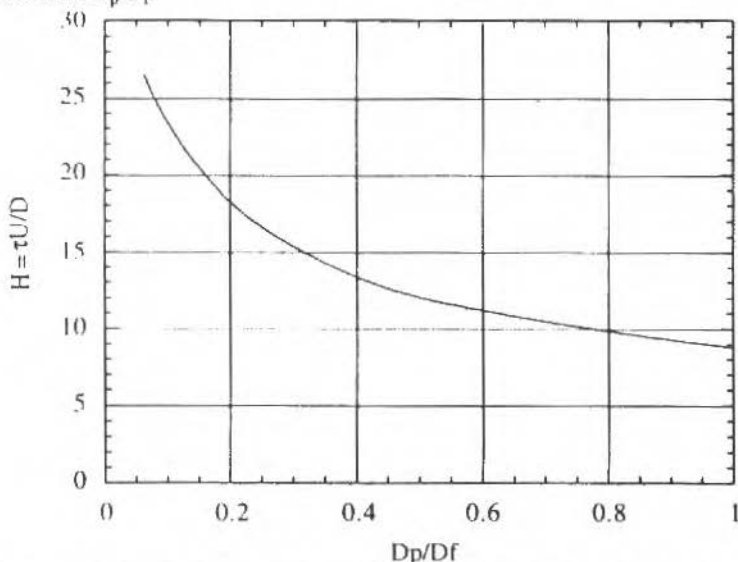

Fig. 2 Influence of the Stokes Number on the Ratio of Particle to Fluid Diffusivity, for Different Values of the Local Turbulence Intensity and the Ratio Between the Lagrangian and Eulerian Micro-Scales

The flow field around the blunt obstacle was obtained by solving the set of Eqs. (1) and (2). The resulting velocity field was then used in the solution of the particle dispersion problem Eq. (3). The concentration field was obtained as a function of the elapsed time after the source for aerosols in the neighborhood of the obstacle has been suddenly interrupted. Previous works (Humphries and Vincent, 1976, Gomes, 1994) have experimentally demonstrated that the decay of particle concentration in the near wake region, after the aerosol source has been removed, becomes exponential following an initial accommodation period. Humphries and Vincent (1976) suggested a dimensionless parameter for characterizing the dispersion phenomena in the near wake, the dimensionless residence time $H = \tau U/D$ (where τ is the time constant for the concentration decay). In Fig. 3, the results of the numerical model are presented in terms of H and D_p/D_f.
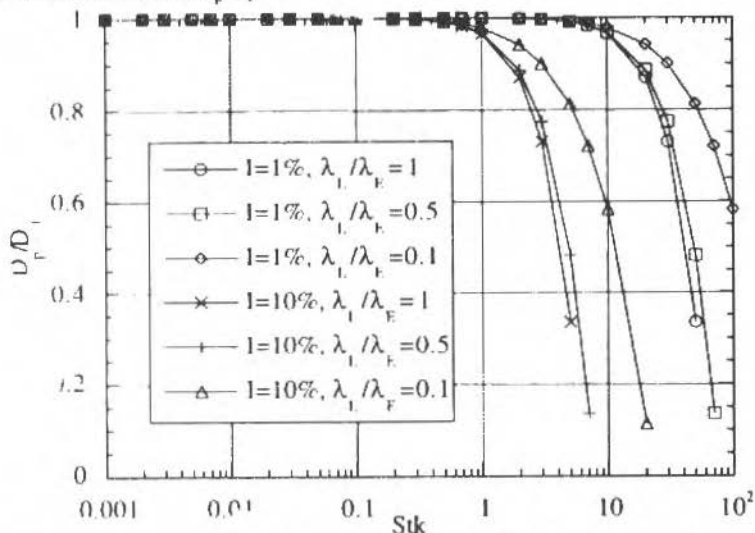

Fig. 3   Dimensionless Residence Time as a Function of the Particle to Fluid Diffusivity

According to the results obtained for the dispersion of inertialess particles (Gomes, 1994), the ratio $D_p/D_f = 1$ was assumed equivalent to $\sigma_C = 0.4$.

With the help of Eq. 9 we may estimate the relationship between the particle inertial behavior (Stk) and the diffusivities ratio (related to σ_C). Although the expression here described is only an approximation, it may provide an indication of the effects that particle inertia may have on the dispersion process.

Conclusion

A simple 2-D numerical procedure was developed, based in the k-ε model of turbulence, for the calculation of the spatial and temporal distribution of the particle number concentration in the flow around a bluff obstacle. Using an analysis based on the work of Peskin (Soo, 1967), we could estimate the ratio between the particle and fluid diffusivities. This approach was used in the investigation of the effect that particle inertia may have on the particle retention in the near wake region of the bluff body. The same procedure could be extended to other turbulent dispersion situations. As expected, the value of the dimensionless residence time in the near wake region (H) increased with the decrease in particle diffusivity, associated with an increase in particle inertia (Stk).

References

Gomes, M.S.P., 1994, "On the Dispersion of Particles in the Near Wake of a Blunt Obstruction", PhD. Thesis, University of Minnesota, Minneapolis, MN, USA.

Hinze, J.O., 1987, "Turbulence", McGraw-Hill, New York.

Humphries, W., and Vincent, J.H., 1976, "An Experimental Investigation of the Detention of Airborne Smoke in the Wake Bubble Behind a Disk", Journal of Fluid Mechanics, Vol. 73, pp. 435-464.

Launder, B.E., and Spalding, D.B., 1972, "Mathematical Models of Turbulence", Academic Press, London.

Patankar, S.V., 1980, "Numerical Heat Transfer and Fluid Flow", Hemisphere Publishing Co., New York.

Patankar, S.V., 1990, "Computation of Fluid Flow and Heat Transfer", Supplementary Material for ME8351, Department of Mechanical Engineering, University of Minnesota.

Rodi, W., and Mansour, N.N., 1993, "Low-Reynolds Number k-ε Modeling with the Aid of Direct Simulation data", Journal of Fluid Mechanics, Vol. 250, pp. 509-529.

Soo, S.L., 1967, "Fluid Dynamics of Multiphase Systems", Blaisdell Pub. Co., Waltham, Massachusetts.

On Kaplun Limits and the Asymptotic Structure of the Turbulent Boundary Layer

Atila P. Silva Freire
Universidade Federal do Rio de Janeiro
COPPE - Programa de Engenharia Mecânica
21945-970 - Rio de Janeiro, RJ Brasil

Abstract

The asymptotic structure of the turbulent boundary layer has been the object of many recent investigations. This has raised some questions as to whether it has a two or a three layered structure. The purpose of this work is to study the turbulent boundary layer asymptotic structure by applying Kaplun limits to a model equation that mimics turbulent flow past over a flat surface. The model equation was chosen for being relatively simple while retaining most of the features of the real problem. This allows one to easily grasp the main concepts and ideas without being hampered by unnecessary details. It turns out that a two-layered structure is derived which, however, is different from the classical structure commonly found in literature, and hence is capable of explaining the flow separation phenomenon. A skin-friction equation resulting from a matching process, and universal laws resulting from local approximated equations are carefully interpreted and evaluated.
Keywords: Turbulent Boundary Layer, Asymptotic Structure, Kaplun Limits.

Introduction

The asymptotic structure of the turbulent boundary layer has been extensively investigated by a number of authors in the past twenty years.

Basically, two approaches are used in literature. In the first, asymptotic methods are applied to the Navier-Stokes averaged equations without appealing to any closure model (Yajnik, 1970, Mellor, 1972). In the second, eddy-viscosity (Bush and Fendell, 1972) or k - ε (Deriat and Guiraut, 1986) models are used to find higher order approximations. In both cases, the theories divide the turbulent boundary layer into two regions, the viscous wall region and the velocity defect region giving raise to a two-layered structure which has become the basis of most subsequently work.

Other authors, however, Long and Chen (1981), Sychev and Sychev (1987), have recently claimed that the turbulent boundary layer has instead a three-layered structure. This structure considers a new region in which a balance of inertia forces, and pressure and turbulent friction forces occur.

In this work, the asymptotic structure of the turbulent boundary layer is investigated by applying Kaplun limits to a model equation that mimics turbulent flow past over a flat surface. The model equation was chosen for being relatively simple while retaining most of the features of the real problem and will hopefully help to further understanding of its conceptual structure. It allows one to easily grasp the main concepts and ideas without being hampered by unnecessary details. It turns out that a two-layered structure is derived which however does not attain the length scales of Sychev and Sychev but is capable of explaining the flow separation phenomenon. A skin-friction is obtained from the matching conditions, and the level of the logarithmic part of the solution, plotted in appropriate coordinates, is shown to be -1.325. This constant results from some hypotheses concerning the nature of the turbulence and is different from the real turbulent boundary layer problem constant (= 5).

The Model Equation

Consider the partial differential equation

$$f\frac{\partial f}{\partial x} - T - \varepsilon\frac{\partial^2 f}{\partial y^2} = 0 \tag{1}$$

$$T = \frac{\partial}{\partial y}\left(\left(ky\frac{\partial f}{\partial y}\right)^2\right), \quad y < y_1 \tag{2}$$

$$T = \varepsilon \times f_0 \ f\frac{\partial^2 f}{\partial y^2}, \quad y \geq y_1 \tag{3}$$

subject to the boundary conditions

$$
\begin{aligned}
x &= 0, & f &= 1 \\
y &= 0, & f &= 0 \\
y &\to \infty, & f &= 1
\end{aligned}
\tag{4}
$$

and where y_1 = point where continuity of f, $\partial f/\partial$ and T must be ensured, $k = 0.4$, $\varepsilon = 10^{-6}$, and $f_0(x)$ = $\partial f(0, x)/\partial y$.

The inertia term in the Navier-Stokes averaged equations is here represented by $f\partial f/\partial$. For the turbulence term, the middle term in Eq.(1), a simple mixing-length/eddy viscosity model is assumed so that the complexity of the problem can be kept to a manageable level and analytical solutions can be obtained. The term with the second derivative in y represents the diffusion term with ε playing the role of the inverse of the Reynolds number. The boundary conditions are standard; thus, at the wall ($y = 0$), the no-slip condition has to be satisfied, whereas, far away from it, the solution must approach a uniform external flow value.

Kaplun Limits

To define Kaplun's limit process we use here the topology on the collection of order classes as introduced by Meyer (1967). The essential idea of η-limit process is to study the limit as $\varepsilon \to 0$ not for fixed x near a singularity point x_d, but for x tending to x_d in a definite relationship to ε specified by a stretching function $\eta(\varepsilon)$. Taking without any loss of generality $x_d = 0$, we define

$$x_\eta = \frac{x}{\eta(\varepsilon)}, \quad G(x_\eta, \varepsilon) = F(x;\varepsilon) \tag{5}$$

with $\eta(\varepsilon)$ a function defined in Ξ (= space of all positive continuous functions on $(0,1]$) and $\varepsilon \in (0, 1]$.

Definition 1 (Meyer, 1967). If the function

$$G(x_\eta;0+) = \lim_{\varepsilon \to 0} G(x_\eta;\varepsilon)$$

exists uniformly on $\{x_\eta/|x_\eta| > 0\}$; then we define $\lim_\eta F(x;\varepsilon) = G x_\eta;(\varepsilon + 0)$.

Transformations (5) and the above definition establish to every order of η a correspondence original equation $\lim_{\to}\eta$ associated equation, on that subset of Ξ for which the associated equation exists (Kaplun, 1967), Silva Freire and Hirata, (1990). The resulting set of associated equations is referred to by Kaplun (1967) as the "splitting" of the original differential equations. The splitting must be seen as a formal property of the equation obtained through a "formal" passage of the η-limits process.

Definition 2. The formal limit domain of an associated equation E is the set of orders ε such that the η-limit process applied to the original equation yields E.

Definition 3. Two equations E_1 and E_2 are said to be equivalent in the limit for a given limit process, $\lim_\eta$, and to a given order, δ, if

$$\frac{E_1(x_\eta, \varepsilon) - E_2(x_\eta, \varepsilon)}{\delta} \to 0, \quad \text{as} \quad \varepsilon \to 0$$

Definition 4 (of formal domain of validity). The formal domain of validity to order δ of an equation E of formal limit domain D is the set $D_0 = D \cup D_i$ where D_i are the formal limit domains of all equations E_i such that E and E_i are equivalent in D_i to order δ.

To relate the formal properties of equations to the actual problem of determining the uniform domain of validity of solutions, Kaplun (1967) advanced two assertions, the Axiom of Existence and the Ansatz about domains of validity. These assertions constitute primitive and unverifiable assumptions of perturbation theory.

Axiom of existence (Kaplun, 1967). If equations E_1 and E_2 are equivalent in the limit to the order δ for a certain region, then given a solution S_1 of E_1 which lies in the region of equivalence of E_1 and E_2, there exists a solution S_2 of E_2 such that as $\varepsilon \to 0, |(S_1 - S_2)/\delta| \to 0$, in the region of equivalence of E_1 and E_2.

To this axiom, there corresponds an Ansatz, namely that there exists a solution S_1 of E_1 which lies in the region of equivalence of E_1 and E_2. More explicitly, we write:

Ansatz (Kaplun, 1967). An equation with a given formal domain of validity D has a solution whose actual domain of validity corresponds to D.

The word "corresponds to" in the Ansatz was assumed by Kaplun to actually mean "is equal to".

Limit-process Analysis

To analyze the problem defined by Eqs. (1) to (3) we consider the following stretching transformations

$$x_\Delta = \frac{x}{\Delta(\varepsilon)}, \qquad y_\eta = \frac{y}{\eta(\varepsilon)}, \qquad g(x_\Delta, y_\eta) = f(x, y)$$

with $\Delta(\varepsilon)$ and $\eta(\varepsilon)$ defined on Ξ.

The resulting transformed equations is

$$\frac{g}{\Delta(\varepsilon)} \frac{\partial g}{\partial x_\Delta} - \frac{\varepsilon}{\eta(\varepsilon)^2} \frac{\partial^2 g}{\partial y_\eta^2} - T_\eta = 0 \tag{6}$$

Passing the η-limit onto Eq. (6) one gets

ord $A\Delta < $ ord $\eta <$ ord 1 : $\qquad g\frac{\partial g}{\partial x_\Delta} = 0,$ \hfill (7a)

ord $A\Delta = $ ord η: $\qquad g\frac{\partial g}{\partial x_\Delta} - T_\eta = 0,$ \hfill (7b)

ord $\varepsilon/A <$ ord $\eta <$ ord $A\Delta$: $\qquad T_\eta = 0,$ \hfill (7c)

ord $\varepsilon/A = $ ord η: $\qquad \frac{\partial^2 g}{\partial y_\eta^2} - T_\eta = 0,$ \hfill (7d)

ord $\eta <$ ord ε/A: $\qquad \frac{\partial^2 g}{\partial y_\eta^2} = 0,$ \hfill (7e)

The above equations were derived under the assumption that the derivatives are ord(A). The signification of A with its physical interpretation is given below.

Equations (7c) and (7d) are distinguished in two ways: i) they are determined by specific choices of η, and ii) they are "richer" than the others in the sense that, application of the limit process to them yields some of the other equations, but neither of them can be obtained from passage of the limit process to any of the other equations. Thus, in the language of Kaplun, these equations are called principal equations. Principal equations are important since they are expected to be satisfied by the corresponding limits of the exact solution. We then make the following definition.

Definition (of principal equation). An equation E of formal limit domain D is said to be principal to order δ if:

i) one can find another equation E', of formal limit domain D', such that E and E' are equivalent in D' to order δ;

ii) E is not equivalent to order δ to say any other equation in D.

A complete solution to our problem should then according to the Axiom of Existence and Kaplun's Ansatz, be obtained from equations (7b) and (7d). The formal domains of validity of these equations cover the entire domain and overlap in

$$D_0 = \{\, ord \ \eta^{//,/}, ord \ \epsilon/A < ord \ \eta < ord \ A\Delta \,\}. \tag{8}$$

The solution of the inner equation, Eq.(7d), is given by

$$g_i = \frac{A}{k}\left[\frac{1-\sqrt{\zeta^2+1}}{\zeta} + \ln(\zeta + \sqrt{1+\zeta^2})\right] \tag{9}$$

with $A = A(x)$ and $\zeta = \dfrac{2Aky}{\epsilon}$

To find a solution for the outer region equation, Eq.(7b), when $y < y_1$, we introduce the variable transformation $t = y_\eta/x_\Delta$ and obtain

$$th'' + h' + \frac{1}{2k^2}h = 0, \tag{10}$$

$$h(t) = g(x_\Delta, y_\eta)$$

The above equation does not have a global analytical solution in domain ord $\eta >$ ord ϵ/A; however, it is possible to find the local behavior that the solution exhibits in the neighborhood of the regular singular point $t = 0$. Thus, as $t \to$, we find

$$h = 1 + B \ \ln \ t - \frac{t}{2k^2} - \frac{Bt}{2k^2}\ln \ t + \frac{t^2}{16k^4} + \frac{Bt}{k^2} + \frac{B}{16k^4}t^2\ln \ t \tag{11}$$

$$+ \left[\frac{1}{36} + \frac{B}{4}\right]\frac{t^3}{8k^6} - \frac{9B}{16k^2}t^2 + \dots$$

On the other hand, when $y \geq y_1$, equation (7b) becomes

$$tp' + p'' = 0 \tag{12}$$

where $p(t) = g(x_\Delta, y_\eta), t = y_\eta/x_\Delta$

The general solution to the above equations is

$$p = E + D\int_0^{t_1} \varepsilon^{-t^2/2} \, dt \qquad (13)$$

To find a solution valid in the whole domain we must show Eqs. (9) and (11) to be equivalent in the overlap domain (8), that is, we must show

$$\lim_\eta (g_i(x_\Delta, y_\eta) - h(y_\eta/x_\Delta)) = 0,$$

η belonging to (8).

From the above limit process, we find

$$\frac{A}{k} \ln \frac{4kAy}{\varepsilon} - \frac{A}{k} = C + B \ln \frac{y\Delta}{x\eta} \qquad (14)$$

This equation shows that overlapping can only be obtained if

$$B = \frac{A}{k}, \qquad (15a)$$

and

$$\frac{A}{k} \ln \frac{4kA\eta x}{\varepsilon\Delta} - \frac{A}{k} = C \qquad (15b)$$

A close inspection of Eq. (15b) reveals that in the limit as $\varepsilon \to 0$

$$\text{ord } (A \ln \varepsilon^{-1}) = \text{ord } 1,$$

and hence

$$\text{ord } A = \text{ord } (\ln \varepsilon^{-1})^{-1} \ll \text{ord } 1$$

This means that the outer and inner regions stretching variables are indeed those indicated in Eqs. (7b) and (7d), that is,

$$\text{ord } \eta = \text{ord } (A\Delta), \qquad (16a)$$

and

$$\text{ord } \eta = \text{ord } (\varepsilon/A), \qquad (16b)$$

respectively.

Since in a turbulent boundary layer the wall stress is given by

$$\tau_w = \mu \frac{\partial u}{\partial y}(x, 0) = \varepsilon \frac{\partial f}{\partial y}(x, 0) = A^2,$$

parameter A represents the friction velocity.

Solutions (9) and (11) can be combined through a composite function rule, that is, by making

$$g_c = g_i + h - \lim_\eta (g_i(x_\Delta, y_\eta) - h(y_\eta/x_\Delta))$$

This procedure yields

$$g_c = \frac{A}{k} \left\{ \frac{1 - \sqrt{\zeta^2 + 1}}{\zeta} + \ln(\zeta + \sqrt{1 + \zeta^2}) \right\} - \frac{\gamma}{2k^2} - \frac{A\gamma}{2k^3} \ln\gamma + \frac{\gamma^2}{16k^4}$$

$$+ \frac{A\gamma}{k^3} + \frac{A}{16k^5}\gamma^2 \ln\gamma + \left[\frac{1}{36} + \frac{A}{4k} \right] \gamma^3 - \frac{9A}{16k^3}\gamma^2 \qquad (17)$$

where $\gamma = y/Ax$.

To ensure continuity of solution at point $y = y_1$, the following three conditions must be satisfied

$$g_c(y_1, x) = p(y_1/Ax), \qquad (18a)$$

$$\frac{\partial}{\partial y} g_c(y_1, x) = \frac{\partial}{\partial y} p(y_1/Ax), \qquad (18b)$$

and

$$\varepsilon f_0 x p \frac{\partial^2 p}{\partial y^2}\Big|_{t=y_1/Ax} = \frac{\partial}{\partial y}\left(k^2 y^2 \left(\frac{\partial g_c}{\partial y}\right)^2 \right)\Big|_{\zeta = \frac{2kAy_1}{\varepsilon}} \qquad (18c)$$

In addition, the boundary condition at infinity yields

$$D \int_0^\infty \varepsilon^{-t^2/2} \, dt + E = 1 \qquad (18d)$$

Solution of the transcendental algebraic system defined by Eqs. (18a) to (18d) furnishes the four unknown parameters A, y_1, D and E.

The value of A, y_1 and D obtained at various stations are shown in Table 1. We recall that physically parameter A represents the friction at the wall.

Comparison of the analytical results given by equation

$$f = \begin{cases} g_c(x, y), & \text{if } y < y_1; \\ p(x/Ay), & \text{otherwise}; \end{cases}$$

with a numerical solution is shown in Fig.1.

Equation (1) is solved numerically through an implicit finite difference scheme. Centered difference accurate to second order are used to discretize the transversal derivatives whereas backward differences accurate to first order are used to discretize the longitudinal derivatives. Simple lagging is used to linearize the obtained algebraic equations. The resulting linearized system is solved by the Thomas algorithm and iteration is used to handle the non-linearity, with the position of y_1 being re-evaluated at each time. Only three iterations were shown to be necessary for convergence of the derivative of f at the wall to an absolute error of 10^{-5}.

Table 1   Predictions of A and of y_1

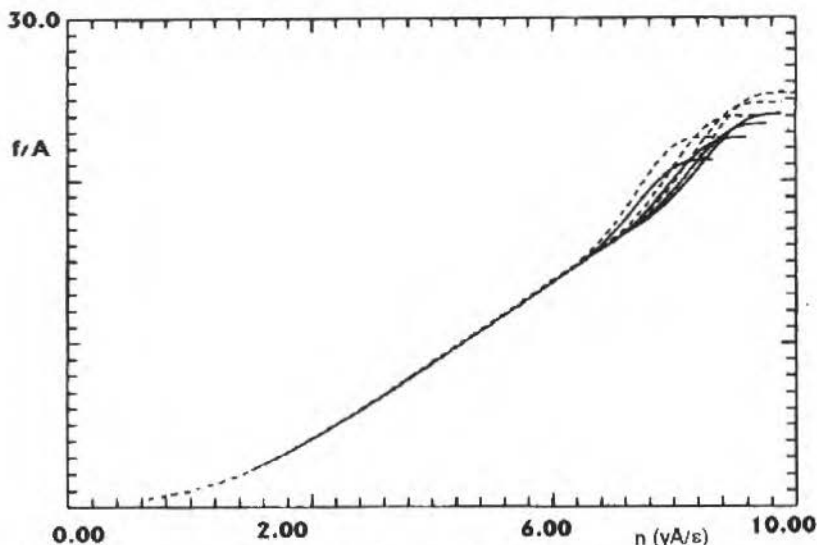|	Theoretical		Numerical	
x	A	y_1	A	y_1
5	0.0469	0.0117	0.0440	0.0112
10	0.0440	0.0220	0.0416	0.0206
15	0.0424	0.0318	0.0403	0.0300
20	0.0414	0.0414	0.0394	0.0392

Fig. 1   The Predictions of f at the Four Stations x=5, 10, 15, 20. -, Theoretical; ... Numerical

If a pressure gradient term is added to our model equation, the two-deck flow structure will remain. The length scale of the outer solution however will change.

To estimate the overlap domain of Eqs. (7b) and (7d) we use Kaplun's concept of equivalent in the limit to obtain

$$R = \frac{\dfrac{\varepsilon}{\eta^2}\dfrac{\partial^2 g}{\partial y_\eta^2} - \dfrac{1}{\Delta}g\dfrac{\partial g}{\partial x_\Delta}}{\varepsilon^\nu}$$

Noting that the leading order term in region $\varepsilon/A < \eta < A\Delta$ is the turbulent term, of ord (A^2/η), we normalize the above equation to order unity to find

$$R = \frac{\nu}{A^2\varepsilon^\nu}\left[\frac{\varepsilon}{\eta^2}\frac{\partial^2 g}{\partial y_\eta^2} - \frac{1}{\Delta}g\frac{\partial g}{\partial x_\Delta}\right]$$

Then since ord $(\partial^2 g/\partial y_\eta^2)$ = ord $(g\partial g/\partial x_\Delta)$ = A, the formal domain of overlapping is given by

$$D = \{\eta/\text{ord } (\varepsilon^{1-\nu}/A) < \text{ord } \eta < \text{ord } (\varepsilon^\nu A\Delta)\}$$

Thus according to Kaplun's Ansatz about domains of validity, the above approximate solutions, Eqs. (9) and (11) only overlap if

$$0 \le \nu \le \frac{1}{2}\left(1 - \frac{\ln A^2\Delta}{\ln \varepsilon}\right)$$

Conclusion

The application of Kaplun limits to our model equation does suggest the turbulent boundary layer to have a two-deck structure, the principal equations being located at points $A\Delta$ and ε/A of the Ξ space. For flows where an additional pressure-gradient like term must be considered in the model equation, the asymptotic structure will remain the same but the position of the outer principal equation will change to $A^2\Delta$.

The analytic solution shows that in the overlap region, Eq. (8), the inner equation tends asymptotically to

$$g_i = \frac{A}{K} \ln \frac{4Aky}{\varepsilon} - \frac{A}{k},$$

that is,

$$g_i = \frac{A}{K}\left(\ln \frac{Ay}{\varepsilon} - 1,325 \right), \tag{19}$$

an expression different from the law of the wall equation commonly quoted in literature.

For real flows, the linear coefficient in Eq. (19) is 5.0 yielding values of A lower than those found in the present analysis. The constant 1.325 in Eq. (19) is solely a consequence of the specified turbulence model, which must be modified if a more realistic description of the flow is desired.

To the author's knowledge, this is the first time that Kaplun limits are used to analyze the turbulent boundary layer problem where quantitative results are presented. In particular, it is the first time that Eq. (17) is presented. In most analyses of the problem, approximate solutions are obtained by breaking-up Eq. (7d) into the two intermediate Eqs. (7c) and (7e). This procedure introduces a spurious constant into the problem associated with the patching of the intermediate solutions in ord η = ord ε/A, which is determined on physical grounds and hence ensures a reasonable agreement of the analytic solution with the experimental profile. Equation (17) is resultant of the principal equations solutions, and for this reason dispenses this true juggling.

Acknowledgments

References

Yajnik, K.S., 1970, "Asymptotic Theory of Turbulent Shear Flow", J.F.M., Vol. 42, pp. 411-427.

Mellor, G.L., 1972, "The Large Reynolds Number Asymptotic Theory of Turbulent Boundary Layers", Int. J. Engng. Sci., Vol. 10, pp. 851-873.

Bush, W.B., and Fendell, F.E., 1972, "Asymptotic Analysis of Turbulent Channel and Boundary Layer Flows, J.F.M., Vol. 56, pp. 657-681.

Deriat, E. and Guiraud, J.P., 1986, "On the Asymptotic Description of Turbulent Boundary Layers", J. Theor. Appl. Mech., Special issue, pp. 109-140.

Long, R.R., and Chen, J.C., 1981, "Experimental Evidence for the Existence of the Mesolayer" in the Turbulent Systems", J.F.M., Vol. 105, pp. 19-59.

Sychev, V.V., and Sychev, V.V., 1987, "On Turbulent Boundary Layer Structure", P.M.M. U.S.S.R., Vol. 51, pp. 462-467.

Meyer, R.E., 1967, "On the Approximation of Double Limits by Single Limits and the Kaplun Extension Theorem", J. Inst. Maths. Applics., Vol. 3, pp. 245-249.

Kaplun, S., 1967, "Fluid Mechanics and Singular Perturbations", Academic Press.

Silva Freire, A.P., and Hirata, M.H., "Approximate Solutions to Singular Perturbation Problems: the Intermediate Variable Technique", J. Math. Analysis and Appl., Vol. 145, pp. 241-253.

Turbulent Incompressible Flow Within a Channel With Transpiration: Solution of the Coupled Problem Porous Wall - Main Flow

G.A.C. França
Universidade Federal de Minas Gerais
Departamento de Engenharia Mecânica
31270-901 - Belo Horizonte, MG - Brasil

G. Tedeschi
A. Lallemand
CETHIL - INSA de Lyon
URA CNRS 1372, Villeurbanne - France

Abstract

A turbulent non-isothermal flow of air in a channel, with cool air injection through a porous plate in the bottom of the channel, is simulated. Lam-Bremhorst turbulence model with the Yap correction is used. Main flow and bottom wall temperature profiles are presented and discussed, as well as friction coefficient and Stanton number, with or without injection. Calculations have been found in good agreement with experimental data. For the studied case, the optimum blowing rate to cool the porous wall is found to be of the order of 1% of the main flow rate.

Keywords: Turbulent Flow, Channel with Transpiration.

Introduction

Transpiration cooling and film cooling are two methods used to project a solid wall from thermal effects of a hot gas flow. They have been developed to cool walls exposed to severe heat sources, for example to respond to the need of high turbine inlet temperatures, in order to increase engine performances.

In the following of the study, the hot flow developing on the wall will be called main flow and the cool flow used to protect wall, secondary flow. The film cooling method consists in injecting cool gas through slots or rows of roles to create a cool layer on the surface, whereas in transpiration cooling the secondary flow occurs through a porous material and is generally considered uniform.

If film cooling has been widely studied and used as it is relatively easy to implement, it is less efficient than transpiration cooling (Eckert and Cho, 1994) and the insulating film is more sensitive to the main flow turbulence (Mehendale et al., 1994 and Lebedev et al., 1994). Moreover, in transpiration cooling, the cooling process is not only due to the cool layer but also to heat transfer inside the porous wall. Literature is less abundant for this technique, and studies are mainly experimental or analytical. Experiments have been realized by Romanenko and Kharchenko (1963), Moffat and Kays (1968) and Andrews and Ansere (1984). Analytical studies have been held for more than thirty years (for example Koh and del Casal, 1965), until nowadays. Simpson (1970) and França et al. (1994) studied characteristics of turbulent transpired boundary layers. Many studies realized in Soviet Union were derived from works made by Kutateladze and Leontiev (1990). They expressed changes in Stanton number and friction coefficient as functions of injection rate. Brouwers (1995), more recently, found another expression for Stanton number, using a simplified film model, and it was extended to friction coefficient by Tedeschi et al. (1995).

In the case of transpiration cooling, the complete problem turbulent main flow coupled with the flow through porous wall has not been solved. Many studies give emphasis to only one of these aspects. Lips et al. (1994) have calculated velocity and temperature of gases with a detailed model through a porous plate, coupled with a simple model for main flow. On the contrary, Eckert and Cho (1994) used a realistic model for the turbulent main flow but coupled with a very idealized model for the secondary flow.

In this study, we consider a turbulent air flow at high temperature developing on a porous plate cooled by a transversal flow occurring through it. The secondary flow is supposed to be laminar. Calculations are realized with SIMPLEST algorithm of Patankar (finite volume method). Lam-Bremhorst (1981) and Yap (1987) models are used for turbulent main flow. An expression for pressure losses through porous wall found by Lips et al. (1994) from various expressions and experiments is used. Thermal equilibrium is supposed to exist between the solid and the gas inside the porous wall.

Profiles of temperature inside the wall and in the flow are presented, changes in Stanton number and friction coefficient on the wall are studied as functions of the injection rate, as well as their evolutions as function of the Reynolds number.

Presentation of the Studied Problem

A diagram of the studied flow is presented on Fig. 1. The turbulent main flow of air in the rectangular channel is supposed steady, non-isothermal and incompressible. Air is injected through a region of the bottom wall of the channel (porous plate).
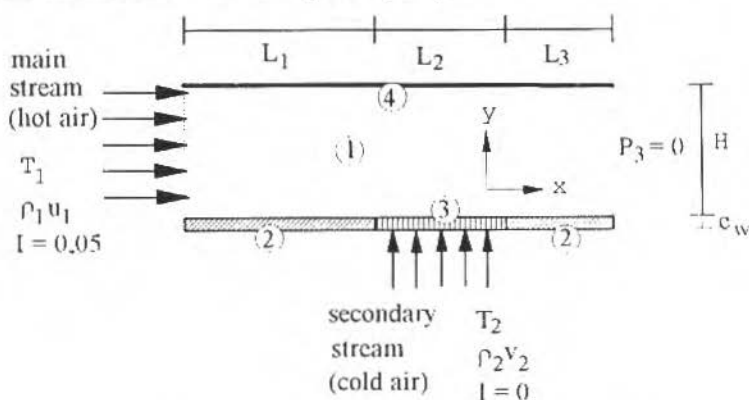
Fig. 1 Diagram of the Flow in the Channel With Blowing

For needs of numerical modeling of the problem, four specific areas are defined:

1 - The main flow, with uniform inlet conditions for temperature (T_1), relative pressure (P_1), mass flux $(\rho_1 u_1)$ and turbulence intensity $(I = 5\%)$;

2 - The first and the third part of bottom wall (whose lengths are respectively L_1 and L_3) are not porous and are submitted to thermal transfers on their bottom, top and lateral surfaces;

3 - The part of bottom wall (porosity φ) is submitted to the same transfers. Uniform inlet conditions are considered on its bottom surface for temperature (T_2), relative pressure (P_2) and mass flux $(\rho_2 v_2)$. The turbulence intensity of the secondary stream is supposed negligible and

4 - The top wall, non porous and at a constant temperature T_1.

Following hypothesis have been considered. Air is an ideal gas with variable density, viscosity and thermal conductivity (with temperature). Thermal capacity $(c_p = 1004 \ Jkg^{-1}K^{-1})$ and Prandtl number $(Pr = 0,715)$ are constant. Thermal radiation is not taken into account. The flow is two-dimensional in the channel and one-dimensional in the porous plate. The length L_1 is calculated in order to have the Reynolds number based on longitudinal abscissa $Re_x = 2 \times 10^5$ at the beginning of injection area.

Numerical Modeling of the Problem

The general differential equation for the transport of a mean intensive quantity ϕ can be written (Patankar, 1980):

$$\frac{\partial}{\partial x}(\rho u \phi) + \frac{\partial}{\partial y}(\rho v \phi) = \frac{\partial}{\partial x}\left(\Gamma_\phi \frac{\partial \phi}{\partial x}\right) + \frac{\partial}{\partial y}\left(\Gamma_\phi \frac{\partial \phi}{\partial y}\right) + S_\phi \tag{1}$$

where ρ is the density, x the cartesian horizontal coordinate from the channel inlet, y the vertical coordinate from the bottom surface of the bottom wall, Γ_ϕ the isotropic diffusive coefficient and S_ϕ the source rate by volume for the considered ϕ quantity.

Area 1: main flow. The Lam-Bremhorst (1981) $k - \varepsilon$ model has been chosen for calculation of the kinetic turbulent energy (k) and dissipation rate for the kinetic turbulent energy (ε) in the main flow. Its effectiveness has been proven in various studies on turbulent flows with coupled thermal transfers (Triboix and Lenat, 1994 and Patel et al., 1984). This model tends however to overestimate energy and momentum transfers at the wall, in the case of flows with detachment and reattachment of the boundary layer, occurring in flow with injection. For this reason, the Lam-Bremhorst model with Yap correction (1987) has been used. This correction consists in adding a source term in the ε equation, reducing turbulence intensity in the wall vicinity. Diffusive coefficients are defined by:

$$\Gamma_k = \rho v + \frac{\rho v_t}{\sigma_k} \qquad\qquad \Gamma_\varepsilon = \rho v + \frac{\rho v_t}{\sigma_\varepsilon} \tag{2}$$

where v is the fluid kinematic viscosity, v_t the turbulent kinematic viscosity of the flow and σ_k and σ_ε are constants. Sources are defined by:

$$S_k = G - \rho\varepsilon$$

$$S_\varepsilon = C_{\varepsilon 1} f_1 \frac{\varepsilon}{k} G - C_{\varepsilon 2} f_2 \rho \frac{\varepsilon^2}{k} + E$$

Values of coefficients can be easily found in original papers of Lam and Bremhorst (1981) and Yap (1987). Difference between models consists in the E term: E = 0 for Lam-Bremhorst model and

$$E = \max\left[0.83\rho\frac{\varepsilon^2}{k}\left(\frac{l_1}{C_1 y_m}-1\right)\left(\left(\frac{l_1}{C_1 y_m}\right)^2, 0\right)\right]$$

for Yap correction, with $l_1 = \frac{k^{1.5}}{\varepsilon}$, $C_1 = 2.44$ and where y_m is the vertical distance to the nearest wall.

Boundary conditions associated to k and ε equations are, for main stream inlet (França et al., 1994):

$$k = (Iu_1)^2 \qquad \text{and} \quad \varepsilon = 0.1643\frac{k^{1.5}}{0.05H} \tag{5}$$

and for the porous plate surface on the main stream side:

$$k_w = 0 \quad \text{and} \quad \frac{\partial\varepsilon}{\partial y}\bigg|_w = 0 \tag{6}$$

subscript w referring to wall boundary. Conditions (6) mean that, on the plate, the mean horizontal velocity is equal to zero and spatial velocity fluctuations are negligible.

Area 2: solid plates. In this area, only the energy equation has to be solve. Thermal diffusion along x is supposed negligible compared to the one along y, then:

$$\frac{\partial}{\partial y}\left(\lambda_s \frac{\partial T_s}{\partial y}\right) = 0 \tag{7}$$

where λ_s and T_s are respectively the thermal conductivity and the absolute temperature of the solid. Boundary conditions associated to Eq. (7) are, for bottom surface of the plate:

$$\lambda_s \frac{\partial T_s}{\partial y}\bigg|_b = h(T_b - T_2) \tag{8}$$

where h is the global coefficient for thermal transfer between plate and outside and subscript b referring to bottom surface of the solid plate, and for top surface of the plate:

$$\lambda_s \frac{\partial T_s}{\partial y}\bigg|_w = \lambda \frac{\partial T}{\partial y}\bigg|_w \tag{9}$$

Equation (9) expresses continuity condition for heat flux and temperature profile at the air-solid plate interface.

Area 3: porous plate. In this area, flow is supposed to be one-dimensional ($u = 0$) and there is locally thermal equilibrium between air and solid ($T = T_s$). Energy equation is then (Nield and Bejan, 1992):

$$\rho \upsilon c_p \frac{\partial T}{\partial y} = \frac{\partial}{\partial y}\left(\lambda_e \frac{\partial T}{\partial y}\right) \tag{1}$$

where υ is the mean flow velocity in porous plate defined by $\upsilon = \varphi$ (φ plate porosity) and λ_e is the equivalent conductivity of porous plate:

$$\lambda_e = (1 - \varphi)\lambda_s + \varphi\lambda \tag{11}$$

Boundary conditions associated to Eq. (10) are, for bottom surface of the porous plate:

$$\lambda_e \frac{\partial T}{\partial y}\bigg|_b = 0 \tag{12}$$

and for top surface of the porous plate:

$$\rho \upsilon c_p (T_w - T_2) = \lambda_e \frac{\partial T}{\partial y}\bigg|_w = \lambda \frac{\partial T}{\partial y}\bigg|_w \tag{13}$$

Pressure profile inside the porous plate can be obtained through the following equation found by Lips et al. (1994):

$$\frac{\partial P}{\partial y} = K_0\left(\frac{\rho_2 \upsilon_2}{\rho}\right)^\alpha \frac{(\rho_2 \upsilon_2)^2}{\rho v} \tag{14}$$

where K_0 and α are empirical constants calculated from experimental values of total pressure loose through porous plate ΔP and mass flux $\rho_2 \upsilon_2$.

Solution of Differential Equations Set

Differential equations and boundaries conditions have been discretised with the finite volume method and the resultant algebraic equations set has been solved with SIMPLEST algorithm. Hyperbolic solution has been used, with hybrid interpolation scheme for convective terms. Scalar and vectorial quantities have been defined in calculation domain with staggered grids. Diffusive terms have been discretised using harmonic mean for diffusive coefficients.

Convergence tests and grid set up. Preliminary tests allowed to define grid and number of iterations needed to reach convergence on velocity and temperature. Tests have been developed with uniform grid along x and along y in areas 2 and 3 and with symmetric and non-uniform grid along y in area 1. Spacing between grids along y (Δy) in area 1 are defined by the law $\Delta y_j = F \Delta y_{j-1}$, subscript j referring to grid number from nearest wall. The value Δy_1 (centre distance of first grid from wall) has been calculated in order to have $y^+ = u_\tau y / \nu < 1$ at the centre of the grid, u_τ being the friction velocity defined by $u_\tau = \sqrt{\tau_p / \rho}$, where τ_p is the wall shear stress. Value of τ_p can be estimated using the following expression: $\tau_p = c_f/2 \left(\rho_1 u_1 \right) = 0.0295\, Re_L^{-0.2}$, Re_L being the value of Reynolds number at the beginning of the porous plate (2×10^5). With the value $F = 1.1$, 94 grids have been obtained along y in area 1, with 5 values of $y^+ \le 11.5$ in the vicinity of top and bottom walls. The laminar sublayer is thus taken into account in the calculation domain. Ten uniform grids have been used along y in area 2 and 3 and 20 uniform grids along x for the whole calculation domain. Convergence has been reached after 250 iterations.

Turbulent Flow on a Flat Plate

Turbulent flow on a flat plate (semi-infinite flow) has been chosen to validate the model because this case is very close to the one interesting us and, moreover, experimental data can be found in literature. In figure 2, values of the skin friction coefficient $c_{f_0}/2$ without injection calculated with Lam-Bremhorst model and Lam-Bremhorst model with Yap correction are compared to values calculated with the following empirical expression (Moffat and Kays, 1968):

$$\frac{C_{f_0}}{2} = 0.0295 Re_x^{-0.2} \tag{15}$$

as a function of Reynolds number Re_x.

In Fig. 3 are presented similar results but with Stanton number, defined by:

$$St = \frac{q_w}{\rho_1 u_1 c_p (T_1 - T_w)} \tag{16}$$

where q_w is the heat flux at the wall and T_w the temperature of the air at the wall. Empirical expression for the Stanton number without injection is (Moffat and Kays, 1968):
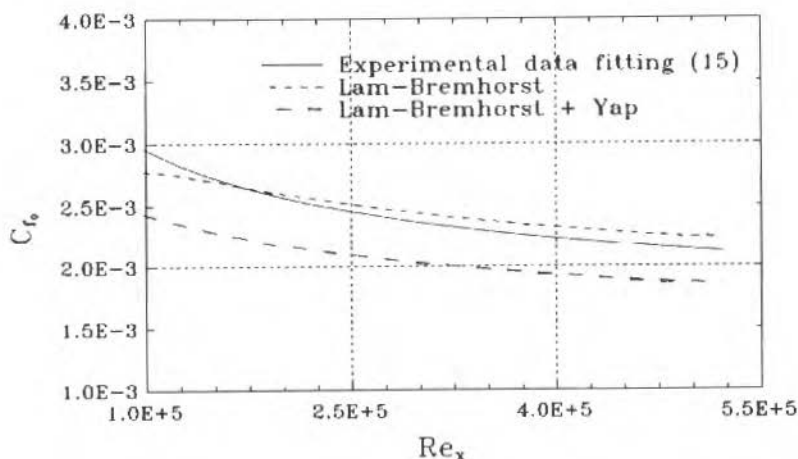

Fig. 2   Skin Friction Coefficient $c_{f_0}/2$ as a Function of the Reynolds Number for a Flat Plate without Injection, Comparison Between Calculated Values and Empirical Expression
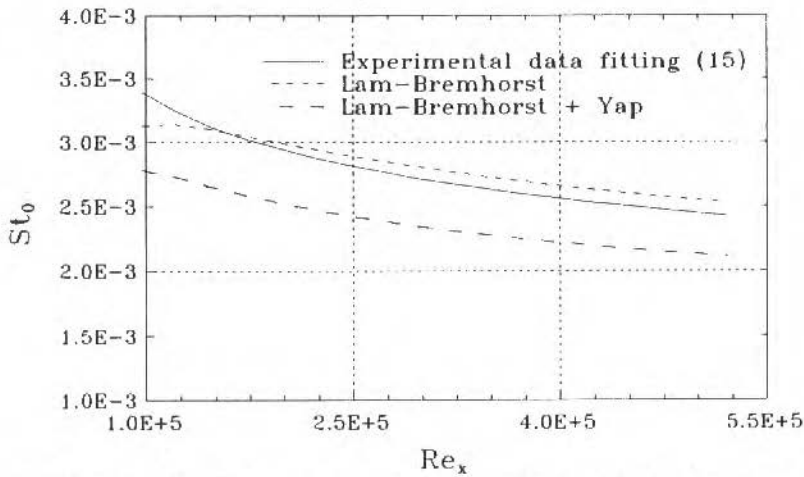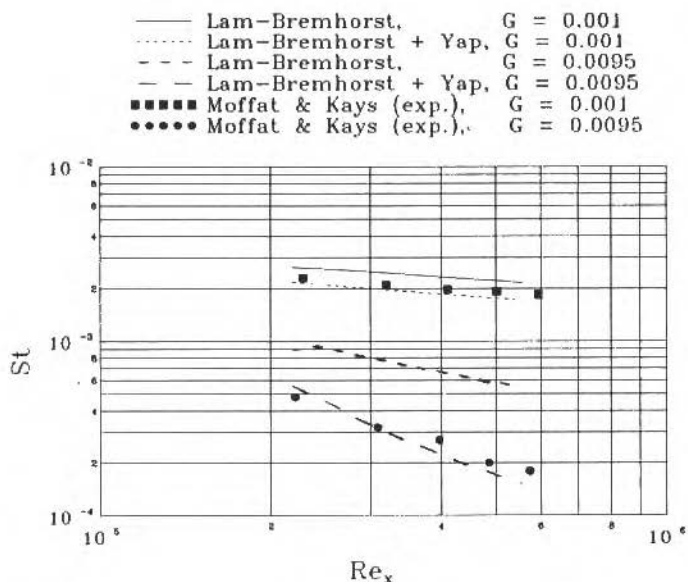
Fig. 3 Stanton Number (St_0) as a Function of the Reynolds Number (Re_x) for a Plane Plate Without Injection; Comparison Between Calculated Values and Empirical Expression

$$St_0 = 0.0295 \ Re_x^{-0.2} Pr^{-0.40, 4} \tag{17}$$

with Prandtl number $Pr = 0.715$ (for air at $20°C$).

It can be noticed, in Figs. 2 and 3, that results obtained with Lam-Bremhorst model are close to experimental results. On the other hand, Yap correction reduces unadequately values of skin friction coefficient and Stanton number in this condition.

Figure 4 presents a comparison between calculated Stanton number and experimental data obtained by Moffat and Kays (1968), as a function of the Reynolds number, for two values of injection rate ($M = 0.001$ and $M = 0.0095$) defined by $M = \frac{\rho_2 v_2}{\rho_1 u_1}$ or $M = \frac{v_2}{u_1}$, if ρ is constant. These results show that Yap correction improves Lam-Bremhorst model, specially for the highest injection rate ($M = 0.0095$).

On Fig. 5 are plotted numerical values and experimental data (obtained by Moffat and Kays, 1968 and Romanenko and Kharchenko, 1963) of the ratio St/St_0 as a function of the ratio M/St_0. Calculations made with Yap correction are more accurate than calculations made with Lam-Bremhorst model without correction.

Turbulent Flow of Air in a Rectangular Channel with Injection

Lam-Bremhorst model with Yap correction has been used to simulate a turbulent flow of air in a channel with injection of air, gas properties being not constant. Temperature of the main flow is $T_1 = 573K$, velocity $u_1 = 14$ m/s and temperature of the secondary flow is $T_2 = 300K$. The ratio between the thermal conductivity of solid and air is $\frac{\lambda_S}{\lambda} = 2500$ and the coefficient for thermal transfer $h = 10$ W m^{-2}K^{-1}. Dimensions of the channel are (as defined in Fig. 1): $L_1 = 0.6$ m, $L_2 = 0.3$ m, $L_3 = 0.3$ m, $H = 0.2$ m and $e_w = 0.01$m.

Fig. 4   Stanton Number (St) as a Function of the Reynolds Number (Re$_x$) for a Plane Plate with Injection;
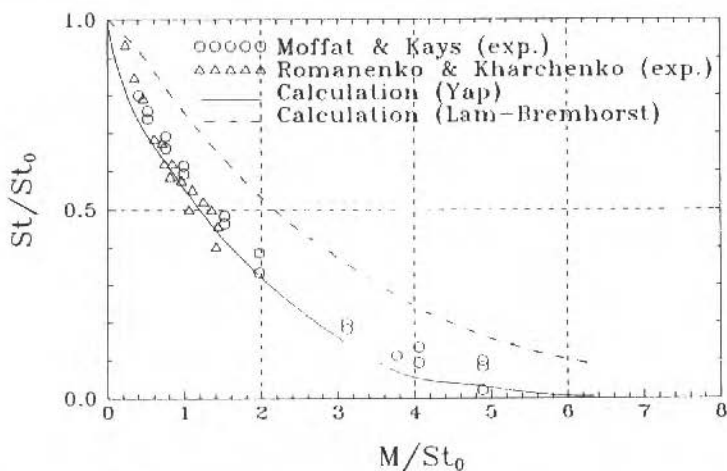Comparison Between Calculated Values and Experimental Data

Fig. 5   St/St$_0$ as a Function of M/St$_0$; Calculated and Experimental Values

Figure 6 presents profiles of dimensionless temperature $\theta = \frac{T - T_2}{T_1 - T_2}$ calculated for $x = 0.75$ m
(middle of the injection area), for different injection rates. Curves 2, 3 and 4 show that thermal
protection of the wall increases with injection rates M. The value $M = 0.01$ seems to be a limiting
value, surface temperature of wall being almost the same for $M = 0.012$.
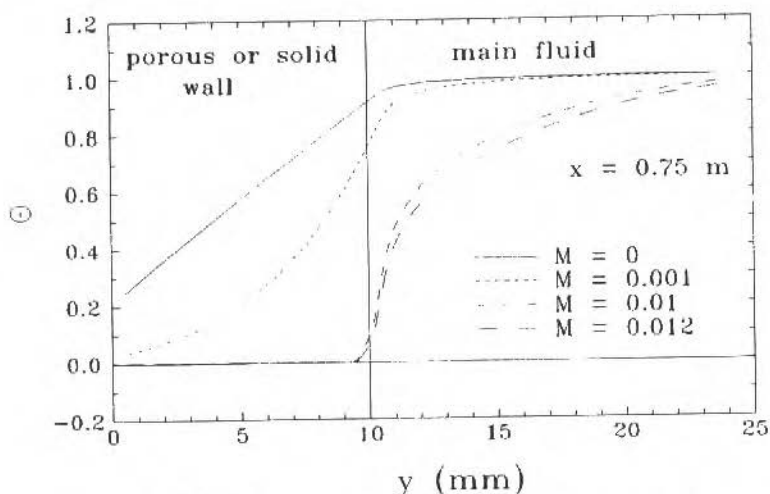
Fig. 6   Dimensionless Temperature for Various Injection Rates

Figure 7 shows profiles of dimensionless temperature $\Theta = \dfrac{T_w - T_2}{T_{w_0} - T_2}$ along the bottom wall of channel, T_w and T_{w0} being the upside surface temperature of the wall respectively with and without blowing. Protective effect of injection is negligible upstream blowing region for all injection rates. In the blowing region, temperature is lower for high injection rates and is almost the same for M = 0.01 and M = 0.012, as already seen on Fig. 6. The refreshing effectiveness decreases rapidly downstream blowing region.
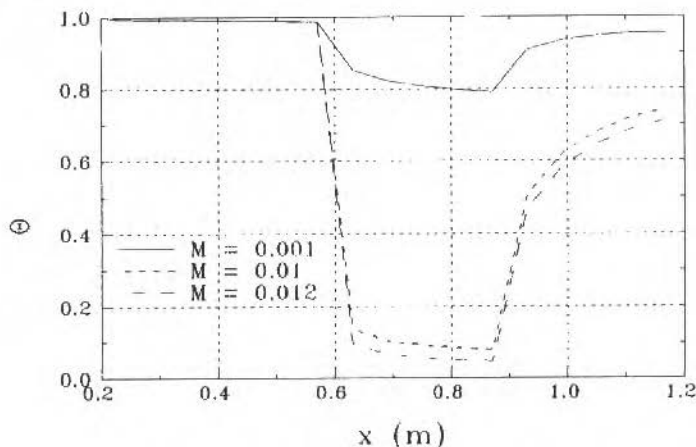
Fig. 7   Dimensionless Temperature Along the Bottom Wall of Channel (Blowing Region: $0.6 \leq x \leq 0.9$)

Conclusion

Effect of the Yap correction on Lam-Bremhorst model has been shown in the simulation of turbulent flow on permeable and impermeable plates. This model has been used for simulation of turbulent non-isothermal flow of air in a rectangular channel, with injection of air through a region of

its bottom wall. Profiles of temperature in the bottom wall and in the main flow are presented, supposing thermal equilibrium between solid and air inside the porous plate. Results allow to determine, for the studied case, an optimum injection rate of the order of 0.01 for the porous plate cooling. Results show also that injection has no influence on temperature profiles upstream injection area, and that cooling effectiveness decreases rapidly downstream the porous plate.

Acknowledgments

References

Andrews, G.E., and Asere, A., 1984, "Transpiration Cooling of Gas Turbine Combustion Chamber Walls", 1st UK Nat. Conf. on Heat Transfer, pp. 1047-1056, Leeds, England.

Browers, H.J.H., 1995, "Comments on Transition from Transpiration to Film Cooling", Int. J. of Heat Mass Transfer, Vol. 38, pp. 183-184.

Eckert, E.R.G., and Cho, H.H., 1994, "Transition from Transpiration to Film Cooling", Int. J. of Heat and Mass Transfer, Vol. 37, suppl. 1, pp. 3-8.

França, G.A.C., Li, C. and Lallemand, A., 1994, "Simulação, por Volumes Finitos, do Escoamento Turbulento Incompressível, Não-isotérmico, no Interior de um Duto Retangular, com Injeção", XV CILAMCE, pp. 323-332, Belo Horizonte, Brasil.

Koh, J.C.Y., and del Casal, E., 1965, "Heat and Mass Flow Through Porous Matrices for Transpiration Cooling", Proc. of 1965 Heat Transfer and Fluid Mech. Inst., Los Angeles, U.S.A.

Kutateladze, S.S. and Leontiev., A.I., 1990, "Heat Transfer, Mass Transfer, and Friction in Turbulent Boundary Layers", Hemisphere Publishing Corporation, New York.

Lam, C.K.G., and Bremhorst, K., 1981, "A Modified Form of the k- ε Model for Predicting Wall Turbulence", Trans. of ASME, Vol. 103, pp. 456-460.

Lebedev, V.P., Lemanov, V.V., Mysyura, S.Y., and Terekhov, V.I., 1994, "Efficiency of a Proctetive Gas Film with High Injection Ratios in a Highly Turbulent Main Flow", Journal of Applied Mech. and Tech. Phys., Vol. 35, pp. 49-52.

Lips, B., Andoh, H.Y., and Lallemand, A., 1994, "Couplage Entre un Ecoulement Pariétal et un Ecoulement Effusif à Travers une Paroi Poreuse", Revue Générale de Thermique, No. 395, pp. 659-668.

Mehendale, A.B., Ekkad, S.V., and Han, J.C., 1994, "Mainstream Turbulence Effect on Film Effectiveness and Heat Transfer Coefficient of a Gas Turbine Blade with Air and CO2 Film Injection", Int. J. of Heat and Mass Transfer, Vol. 37, pp. 2707-2714.

Moffat, R.J., and Kays, W.M., 1968, "The Turbulent Boundary Layer on a Porous Plate: Experimental Heat Transfer with Uniform Blowing and Suction", Int. J. of Heat and Mass Transfer, Vol. 11, pp. 1547-1566.

Nield, D.A., and Bejan, A., 1992, "Convention in Porous Media", Springler-Verlag, New York.

Patankar, S.V., 1980, "Numerical Heat Transfer and Fluid Flow", Hemisphere Publishing Corporation, New York.

Romanenko, P.N., and Kharchenko, V.N., 1963, "The Effect of Transverse Mass Flow on Heat Transfer and Friction Drag in a Turbulent Flow of a Compressible Gas along an Arbitrarily Shaped Surface", Int. J. of Heat and Mass Transfer, Vol. 6, pp. 727-738.

Simpson, R.L., 1970, "Characteristics of Turbulent Boundary Layers at Low Reynolds Numbers with and without Transpiration", Journal of Fluids Mechanics, Vol. 42, part 4, pp. 769-802.

Tedeschi, G., França, G.A.C. et Lallemand, A., 1995 (in press), "Refroidissement de Paroi Plane par Transpiration: Comparison de Différents Modèles pour le Calcul des Echanges Thermiques", Congrès Société Française de Thermicien - S.F.T.

Triboix, A. and Lenat, Y., 1994, "Couplage Conduction-Convention-Rayonnement par la Méthode des Volumes Finis", Revue Générale de Thermique, No. 387, pp. 190-197.

Yap, C., 1987, "Turbulent Heat and Momentum Transfer in Recirculating and Impinging Flows", Pd.D. Thesis, Faculty of Technology, University of Manchester, U.S.A.

Wall Effects for a Sphere Falling in a Non-Newtonian Fluid

Marco André O.M. Teixeira
Imperial College of Science
Department of Mechanical Engineering
Technology and Medicine, London UK

Maurício N. Frota
Pontifícia Universidade Católica do Rio de Janeiro
Department of Mechanical Engineering
22453-900 - Rio de Janeiro, RJ Brasil

Abstract

The present investigation considers the problem of a sphere falling along the axis of a vertical cylindrical tube containing a non-Newtonian fluid. The wall proximity effects, characterized by the radius ratio of the sphere to the container, and the shear-thinning properties of the fluid are examined experimentally. The flow of a non-Newtonian fluid past a sphere on the centerline of a cylindrical tube is of fundamental importance to the development of falling ball viscometry techniques.
Keywords: Non-Newtonian Flow, Wall Effects, Falling Ball Viscometry.

Introduction

Since Stokes (1845) first studied the slow motion of a rigid sphere through a viscous liquid, many investigators have analyzed the motions of various shapes of particles, drops and bubbles in Newtonian and non-Newtonian fluids, see, for instance, Leal (1980), Probstein (1989), and Happel and Brenner (1991).

The understanding of the behaviour of the fluids in non-viscometric flows is of great importance in non-Newtonian fluid mechanics, and the translational motion of a sphere in a non-Newtonian liquid is an example of such a problem. A detailed discussion on this subject for the case of an infinite medium, ie. absence of wall effects, may be found in the classical studies of Leslie (1961), Caswell and Schwarz (1962), and Giesekus (1963).

The analysis of the influence of wall effects is of fundamental significance for the development of falling ball viscometry techniques for Newtonian and non-Newtonian fluids. The most widely used procedure for non-Newtonian fluids is the one presented by Caswell (1970).

The influence of wall proximity upon the translation of a sphere falling under gravity on the centreline of a cylindrical tube is well established for Newtonian fluids and can be found on the book by Clift et al. (1978). The corresponding studies for non-Newtonian fluids without yield stress may be found elsewhere (see, for example, Gu and Tanner, 1985; Chhabra, 1986; Sugeng and Tanner, 1986; Mena et al., 1987; Chhabra and Uhlherr, 1988a; and Carew and Townsend, 1988). The literature in viscoplastic medium (ie. non-Newtonian fluids with yield stress) has been summarised by Chhabra and Uhlherr (1988b), and Atapattu et al. (1990).

In the present study, an experimental analysis of the influence of wall effects in the development of falling ball viscometry techniques for non-Newtonian fluids is presented. The shear-thinning and wall effects are described for various sphere to cylinder diameter ratios, and for creeping and low inertia flow regimes.

Theoretical Background

The Stokes drag force D_{St}, for a sphere falling in an infinite expanse of Newtonian fluid may be expressed as:

$$D_{St} = 6 \pi a \mu u_\infty \tag{1}$$

here a is the radius of the sphere, μ is the absolute viscosity of the fluid and u_∞ is the terminal velocity of the sphere. The Stokes drag coefficient $C_{D_{St}}$ is given by:

$$C_{D_{St}} = \frac{D_{St}}{\frac{1}{2}\rho u_\infty^2 \pi a^2} = \frac{24}{Re_\infty} \tag{2}$$

and

$$Re_\infty = \frac{u_\infty \, d \, \rho}{\mu} \tag{3}$$

Re_∞ is the Reynolds number based on the diameter of the sphere d, and ρ is the density of the fluid.

The Stokes law is only valid for $Re_\infty < 0.1$, because the inertia terms are neglected. An improved solution, valid for $Re_\infty < 1$, was presented by Oseen (1927), and reads:

$$C_D = \frac{24}{Re_\infty}\left(1 + \frac{3}{16}Re_\infty\right) \tag{4}$$

A well-known empirical correlation, usually accepted up to $Re_\infty = 100$, may be expressed as:

$$C_D = \frac{24}{Re_\infty}\left(1 + \frac{3}{16}Re_\infty\right)^{1/2} \tag{5}$$

On an experimental study presented by Slattery and Bird (1961), the drag coefficient may be determined for spheres falling in an infinite expanse of non-Newtonian fluids.

The wall proximity effect for a sphere of radius a, falling in a Newtonian fluid along the axis of a cylinder of radius R, may be characterized by a wall correction factor f (a/R), where the drag force on the sphere is:

$$D = 6 \pi a\mu u f(a/R) \tag{6}$$

and the function f (a/R) can be expressed as proposed by Faxén (1923):

$$f(a/R) = \frac{1}{1 - \frac{a}{R}[2.1044 - (2.088\,(a/R))^2 + \ldots]} \tag{7}$$

Faxén's wall correction factor may be used for Reynolds numbers Re < 0.1 and radius ratio a/R < 0.32.

In the absence of wall effects, Eq. (6) reduces to the Stokes drag Eq. (1), and the following relation is obtained:

$$u_\infty = u \, f(a/R) \tag{8}$$

which for Newtonian fluids may be used to obtain the wall correction factor for either the drag or the velocity, due to the linearity of the constitutive equation. However, for non-Newtonian fluids, the viscosity is a function of the shear rate and the velocity has to be corrected.

The drag force on a sphere falling in a non-Newtonian fluid may be expressed as:

$$D = 6 \pi a \mu(\dot{\gamma})u f \tag{9}$$

here, $\mu(\dot{\gamma})$ is the non-Newtonian viscosity, which is a function of the shear rate $\dot{\gamma}$, and f is the wall correction factor, which depends on the non-Newtonian behavior of the fluid.

Experimental evidence has shown that when shear-thinning effects are important, the shear rate $\dot{\gamma}$, may be approximated as:

$$\dot{\gamma} = \frac{u}{2a} \tag{10}$$

and the wall correction factor f, only valid for the velocity correction is:

$$f = \frac{u_\infty}{u} \tag{11}$$

The generalized Reynolds number based on the shear rate dependent viscosity takes the following form:

$$Re = \frac{u\,d\,\rho}{\mu(\dot{\gamma})} \tag{12}$$

Experimental Details

In order to achieve a wide range of values of the radius ratio ($0.1 \le a/R \le 0.5$), and the Reynolds number ($0.01 \le Re \le 33$), two cylindrical tuber of internal diameters of 77mm and 50mm were used with several spheres of stainless steel and plastic, ranging in diameter from 3.5 to 38.5 mm. The weight, diameter and density of each sphere were determined individually. The cylindrical tubes were long enough for the spheres to reach the terminal velocity, which was measured with a digital stopwatch (0.1s precision).

The reproducibility and accuracy of the experiments were set with Newtonian fluids, ie. Glycerol and Glycerol-water solutions of various viscosities. The non-Newtonian polymer used was a 0.75% aqueous solution of carboxymethylcellulose (CMC), power-law flow behavior index $n = 0.7$, consistency parameter $K = 12.8$ Pa·s^n, and density $\rho = 1000$ kg m^{-3}. All tests were carried out at the same temperature ($20 \pm 0.5°C$), and a complete description of the experimental set may be found in Teixeira (1991).

Results

The results for the wall correction factor $f(a/R)$ for Newtonian fluids, and f for the aqueous solution of CMC are presented in Figs. 1 and 2 respectively, for five different radius ratio and are plotted as a function of the Reynolds number. It should be noted first that the results shown in Fig. 1 reproduces the experimental data available in the literature within 3%. It can be seen, from comparing Figs. 1 and 2, that the decrease in the wall correction factor with the increase in the Reynolds number is notably smaller for the non-Newtonian case. For example, for a Newtonian fluid and radius ratio a/ $R = 0.5$, the wall correction factor decreases 60% when the Reynolds number increases from about 0.5 to 33, while for the non-Newtonian fluid the decrease is only about 26%.
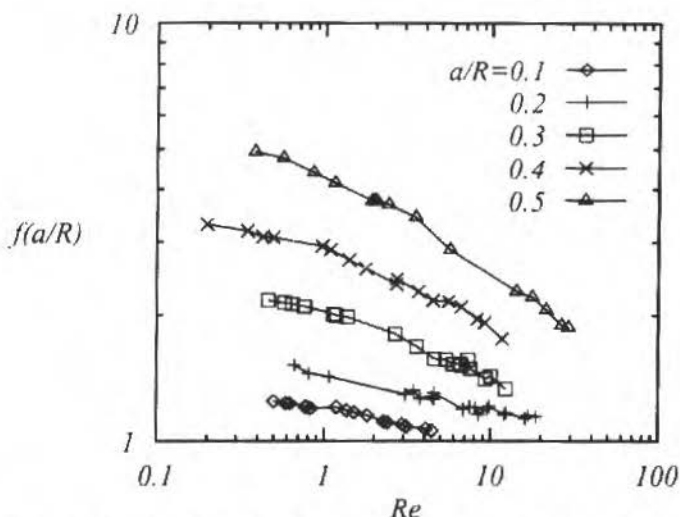
Fig. 1   Variation of the Wall Correction Factor with Reynolds Number for Newtonian Fluids

Turning now into the effects of wall confinement on the drag coefficient, the results for the five radius ratio are presented as a function of the Reynolds number for Newtonian fluids, Figure 3, and CMC, Fig. 4. The solid line in both Figs. represents the variation of the drag coefficient with Reynolds number for the case of infinite medium, ie. absence of wall effects. The symbols (also connected by solid lines) represent the results of the present experiments and clearly demonstrate that the wall effect increases the drag coefficient for increasing radius ratio and decreasing Reynolds number. Once again the reduction in the drag coefficient with the increase in the Reynolds number is smaller for CMC. For example, for a Newtonian fluid and radius ratio a/R = 0.5, the drag coefficient decreases from about 5 to 2.5 times the value of the infinite medium when the Reynolds number increases from about 0.5 to 33, while for CMC decreases from 3.25 to 2.75.

Finally, Fig. 5 illustrates the drag reduction occurred on the drag coefficient when the Newtonian fluid is compared with CMC. Although Fig. 5 only represents the comparison for a/R = 0.5, the same physical behavior was found for all radius ratio.
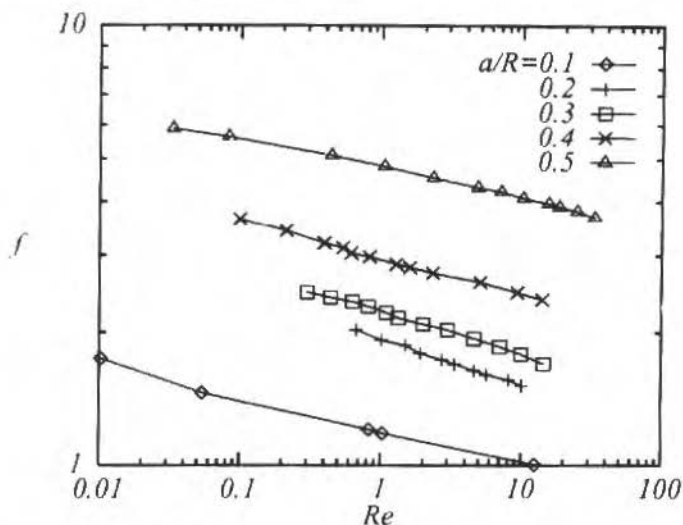
Fig. 2   Variation of the Wall Correction Factor with Reynolds Number for CMC ($n = 0.7$)
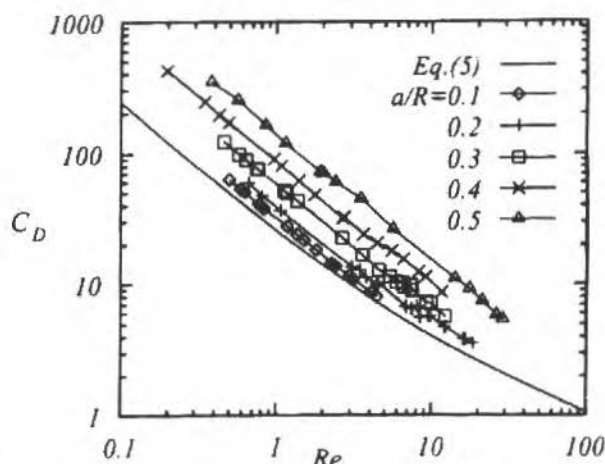
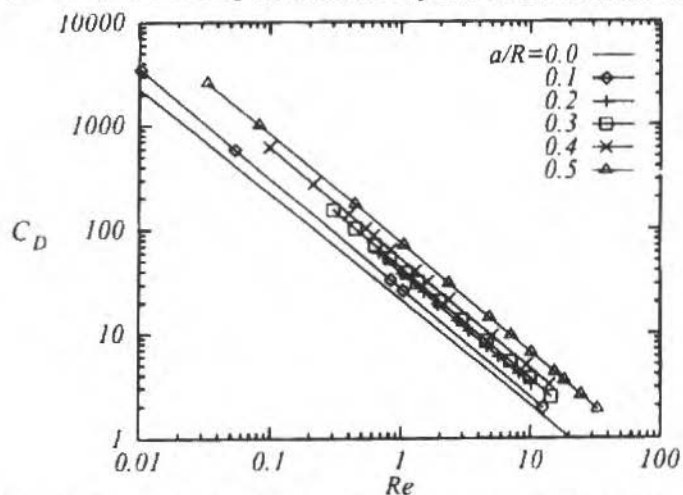Fig. 3 Variation of the Drag Coefficient with Reynolds Number for Newtonian Fluids

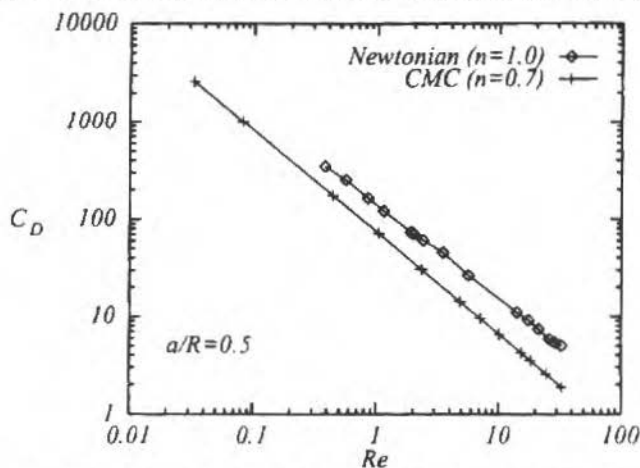Fig. 4 Variation of the Drag Coefficient with Reynolds Number for CMC ($n = 0.7$)

Fig. 5 Comparison of Drag Coefficient for CMC ($n = 0.7$) and Newtonian Fluids (a/R = 0.5)

Conclusions

An experimental study has been carried out and presented the wall correction factor and drag coefficient for radius ratio $a/R = 0.1$ to $a/R = 0.5$ and Reynolds number $Re = 0.01$ to $Re = 33$. Glycerol and Glycerol-water solutions of various viscosities were used as Newtonian fluids, and an aqueous solution of CMC ($n = 0.7$) was used as the non-Newtonian fluid. On the basis of the analysis of the experimental results. it is concluded that:

- The wall effect promotes for both Newtonian and non-Newtonian fluids, a drastic increase in the viscous drag acting on the particle surface and a reduction on the terminal velocity of the particle falling in the fluid, along the axis of the duct;

- The decrease in the wall correction factor and in the drag coefficient with the increase in the Reynolds number is notably smaller for the non-Newtonian case, and

- The present work also identifies a strong drag reduction for the non-Newtonian case, when compared to the Newtonian fluid flow situation.

References

Atapattu, D.D., Chhabra, R.P., and Uhlherr, P.H.T., 1990, "Wall Effect for Spheres Falling at Small Reynolds Number in a Viscoplastic Medium", Journal of Non-Newtonian Fluid Mechanics, Vol. 38, pp. 31-42.

Carew, E.O.A., and Townsend, P., 1988, "Non-Newtonian Flow Past a Sphere in a Long Cylindrical Tube", Rheologica Acta, Vol. 27, pp. 125-129.

Caswell, B., 1970, "The Effect of Finite Boundaries on the Motion of Particles in Non-Newtonian Fluids", Chemical Engineering Science. Vol. 25, pp. 1167-1176.

Caswell, B., and Schwarz, W.H., 1962, "The Creeping Motion of a Non-Newtonian Fluid Past a Sphere", Journal of Fluid Mechanics, Vol. 13, pp. 417-426.

Chhabra, R.P., 1986, "Encyclopedia of Fluid Mechanics", N.P. Cheremisinoff (Ed.), Vol. 1, Gulf Publishing Co., Houston.

Chhabra, R.P., and Uhlherr, P.H.T., 1988a. "The Influence of Fluid Elasticity on Wall Effects for Creeping Sphere Motion in Cylindrical Tubes", Canadian Journal of Chemical Engineering, Vol. 66, pp. 154-157.

Chhabra, R.P., and Uhlherr, P.H.T., 1988b, "Encyclopedia of Fluid Mechanics". N.P. Cheremisinoff (Ed.), Vol. 7, Gulf Publishing Co., Houston

Clift, R., Grace, J.R., and Weber, M.E., 1978, "Bubbles, Drops and Particles", Academic Press, New York.

Faxen, H., 1923, Arkiv. Mat. Astron. Fys., Vol. 17, No. 27, pp. 1.

Giesekus, H., 1963, "Die Simultane Translations - und Rotations-bewegung Einer Kugel in Einer Elastoviskosen Flüssigkeit". Rheologica Acta, Vol. 3, pp. 59-71.

Gu, D. and Tanner, R.I., 1985, "The Drag on a Sphere in a Power-Law Fluid", Journal of Non-Newtonian Fluid Mechanics, Vol. 17, pp. 1-12.

Happel, J., and Brenner, H., 1991, "Low Reynolds Number Hydrodynamics", Kluwer Academic Publishers, Dordrecht.

Leal, L.G., 1980, "Particle Motions in a Viscous Fluid", Annual Review of Fluid Mechanics, Vol. 12, pp. 435-476.

Leslie, F.M., 1961, "The Slow Flow of Visco-Elastic Liquid Past a Sphere", Quarterly Journal of Mechanics and Applied Mathematics, Vol. 14, pp. 36-48.

Mena, B., Manero, O. and Leal, L.G., 1987, "The Influence of Rheological Properties on the Slow Flow Past Spheres", Journal of Non-Newtonian Fluid Mechanics, Vol. 26, pp. 247-275.

Oseen, C.W., 1927, "Neuere Methoden und Ergebnisse in der Hydrodynamik, Aka-desmiche Verlag, Leipzig.

Probstein, R.F., 1989, "Physicochemical Hydrodynamics - An Introduction", Butterworths Publishers, Boston.

Slattery, J.C., and Bird, R.B., 1961, Chemical Engineering Science, Vol. 16, pp. 231-241.

Stokes, G.G., 1845, Trans. Cambridge Phil. Soc., Vol. 8, pp. 287.

Sugeng, F., and Tanner, R.I., 1986, "The Drag on Spheres in Visco Elastic Fluids with Significant Wall Effects", Journal of Non-Newtonian Fluid Mechanics, Vol. 20, pp. 281-292.

Teixeira, M.A.O.M., 1991, "Influência do Confinamento e do Expoente Power-Law no Escoamento de Sistemas Fluido-Particula", (in Portuguese), M.Sc. Dissertation, Pontifícia Universidade Católica do Rio de Janeiro, RJ, Brazil.

Abstracts

Nogueira, F., and Almeida, S. F. M. "Preliminary Considerations on a New Design Concept for Below the Knee Energy Storing Prosthesis", RBCM - J. of the Braz. Soc. Mechanical Sciences, Vol. 18, No. 1, pp.

This study develops a concept for the design and manufacture of energy storing prosthesis that attempts to simplify the design process of such prosthetic devices. This concept consists of three basic steps: identifying requirements, computational analysis and tests. The most relevant parameters used in the process and design compromises between these parameters are identified and explained. Non linear behavior and expected results of non linear finite element analyses are explained together with an overview of laboratory and field tests performed. Some critical points identified in preliminary test results are presented. The methodology proposed was successively applied to the development of a composite material energy storing prosthesis.
Keywords: Energy Storing Prosthesis, Composite Material, Biomechanics

Teodoro, E. B., and McConell, K. G., "Dynamic Response of a Damped Cable With a Compliant Damped Support System", RBCM - J. of the Braz. Soc. Mechanical Sciences, Vol. 18, No. 1, pp.

Power lines are subject to complex aerodynamic forces that may cause galloping. Then a mathematical model was developed in which the conductor is represented by a taut string and the insulator support is modeled as a mass, spring, and damper. A technique called model modification was employed to study this model. A computer program was written to simulate the behavior of the cable under certain boundary conditions while different types of excitations are applied to the cable. The mode-summation method was successfully applied to this class of problem and the advanced model analysis indicated that energy absorber device reduced cable motion while reducing the forces transmitted to the supporting tower.
Keywords: Damped Cable, Support Systems, Mode - Summation Method

Arruda, J. R. F., and Santos, L. A. S. B., "A Data Compression Method for the Modal Analysis of Spatially Dense Laser Vibrometer Measurements", RBCM - J. of the Braz. Soc. Mechanical Sciences, Vol. 18, No. 1, pp.

This paper investigates a method which can be used to compress two-dimensional velocity fields measured with the scanning LDV. The compressed data can be used as virtual measurements when estimating modal parameters. The data is compressed spatially using a two-dimensional Fourier series model. The approximation reduces and filters the measured data in the output space for each frequency line.
Keywords: Data Compression, Modal Analysis, LDV

Silva, E. C., and Buttom, S. T., "Cylinders and Rings Hot Upset Forging Analysis by the Finite - Element Method", RBCM - J. of the Braz. Soc. Mechanical Sciences, Vol. 18, No. 1, pp. (In Portuguese).

The state of the art in forging points to precision forging. The modern competitive forging industry uses computational systems to plan it, instead of the conventional trial and error methods. Based on this tecnology, this work develop a bidimensional finite element mathematical model of rigid-viscoplastic analysis of cylinders and rings hot upsetting, and the code validated by comparing simulation with the upper bound method and experimental results. Teoretical calibration curves used to define friction in the ring test were provided with simulations by the finite element method (FEMME).
Keywords: Forging Hot Upsetting, Finite Element Method, Cylinders, Rings

Duduch, J. G., Porto, A. J. V., Jasinevicius, R. G., and Gee, A. E., "Model of Brittle Materials Single Point Machining With High Removal Rates", RBCM - J. of the Braz. Soc. Mechanical Sciences, Vol. 18, No. 1, pp.

Diamond turning and form-grinding are viable options for manufacturing optical surfaces with adequate surface finish for use in infra-red and forseeably in visual light applications, both spherical and aspherical, without the need for post-machining finish. This restrict ductile-regime (plastic removal of material) diamond turning requires that no cut should exceed the so called critical depth or thickness producing crack-free grooves. However, very low material removal rates are obtained. This work proposes a model in which a greater part of the material may be removed through brittle microfracture whilst a surface and sub-surface can be obtained with low damage levels.
Keywords: Single Point Machining, Brittle Materials, High Removal Rate.

Forcellini, F. A., and Back, N., "Analysis of the Structural Static Response,
Eigenvalues and Eingenvectors of Manipulators With Flexible Joints and Links",
RBCM - J. of the Braz. Soc. Mechanical Sciences, Vol. 18, No. 1, pp. (In Portuguese).

This work presents a methodology for simulation and analysis of the manipulators with flexible joints and links.
Are proposed numerical procedures that permit obtain the structural static response, natural frequencies,
vibration modes for diferents positions of the system.
Keywords: Flexible Joint Robots, Structural Static Response, Natural Frequencies, Vibration Modes

Seixlack, A. L., Prata, A. T., and Melo, C., "Analysis of the HFC-134a Refrigerant Flow
through Capillary Tubes Using the Two-Fluid Model", RBCM - J. of the Braz. Soc.
Mechanical Sciences, Vol. 18, No. 1, pp. (In Portuguese).

This work presents a numerical model to simulate refrigerant flow through capillary tubes, commonly used as
expansion devices in refrigeration systems. The capillary tube is considered straight and horizontal. The flow is
taken as one-dimensional and adiabatic. Steady state and thermodynamic equilibrium conditions are assumed.
The two-fluid model, involving four conservation equations and considering the hidrodynamic nonequilibrium
between the liquid and vapor phases is applied to the flow region. The pressure profiles and the mass flow rates
given by the model are compared with experimental data.
Keywords: Refrigerant Fluid, Flow Through Capillary Tubes, Two-Fluid Model, HFC-134a

Morgenstern Jr., A., "Supersonic Flow Past Pressure Vent Orifices on Satellite
Launcher Vehicles", RBCM - J. of the Braz. Soc. Mechanical Sciences, Vol. 18, No. 1,
pp.

The unsteady, viscous, supersonic flow past a pressure vent orifice on the ogive of a satellite launcher vehicle is
numerically investigated by solving the Navier-Stokes equations. The time accurate computations are performed
employing an implicit numerical algorithm based on the second-order time accurate LU-SGS scheme with the
incorporation of a subiteration to maintain time accuracy. Self-sustained oscillations, that affect adversely the
flow past the office, are observed and its effects on the characteristics of the flow are reported through
instantaneous plots. The unsteady character of the flow is further examined in the frequency domain by the use
of the Maximum Entropy Method for spectral analysis and results compared with a semi-empirical formula for
the prediction of the principal frequencies of oscillation of this type of flow.
Keywords: Supersonic Flow, Pressure Vent Orifices, Sound Pressure Level Attenuation.

Silva, E. M. V., Ferreira, M. C., and Freire, J. T., "Fluid Dynamics Behavior of a
Pneumatic Bed With a Spouted Bed Type Solid Feeding System", RBCM - J. of the
Braz. Soc. Mechanical Sciences, Vol. 18, No. 1, pp. (In Portuguese)

The fluid dynamics behavior of a pneumatic bed with a spouted bed type solid feeding system was investigated
with measurements of voidages, solid velocities and pressure drop axial profiles. The flow was described by the
two-phase unidimensional model for which either the drag coefficient, β, or the particle-wall friction force had
to be estimated. The model was only successful if the β values were obtained from an empirical equation
adjusted from experimental data. As for the particle-wall friction forces, the equation of Yang led to theoretical
predictions for the voidages which were very close to the experimental values.
Keywords: Pneumatic Bed, Spouted Bed Type Solid Feeding System.

Gomes, M. S. P., "Inertial Effects on the Retention of Particles in the Near Wake of
Blunt Obstacles", RBCM - J. of the Braz. Soc. Mechanical Sciences, Vol. 18, No. 1, pp.

This work examines the dispersion of particles in the flow around a blunt obstruction. The investigation involved
the development of a numerical procedure based on the k-ϵ model for turbulence and an Eulerian approach for
taking into account the inertial behavior of the particle.
Keywords: Dispersion of Particles, Wake of Blunt Obstacles, Inertial Effects.

Freire, A. P. Silva, "On Kaplun Limits and the Asymptotic Structure of the Turbulent Boundary Layer", RBCM - J. of the Braz. Soc. Mechanical Sciences, Vol. 18, No. 1, pp.

The asymptotic structure of the turbulent boundary layer has been the object of many recent investigations. This has raised some questions as to whether it has a two or a three layered structure. The purpose of this work is to study the turbulent boundary layer asymptotic structure by applying Kaplun limits to a model equation that mimics turbulent flow past over a flat surface. The model equation was chosen for being relatively simple while retaining most of the features of the real problem. This allows one to easily grasp the main concepts and ideas without being hampered by unnecessary details. It turns out that a two-layered structure is derived which, however, is different from the classical structure commonly found in literature, and hence is capable of explaining the flow separation phenomenon. A skin-friction equation resulting from a matching process, and universal laws resulting from local approximated equations are carefully interpreted and evaluated.
Keywords: Turbulent Boundary Layer, Asymptotic Structure, Kaplun Limits.

França, G. A. C., Tedeschi, G., and Lallemand, A., "Turbulent Incompressible Flow Within a Channel With Transpiration: Solution of the Coupled Problem Porous Wall - Main Flow", RBCM - J. of the Braz. Soc. Mechanical Sciences, Vol. 18, No. 1, pp.

A turbulent non-isothermal flow of air in a channel, with cool air injection through a porous plate in the bottom of the channel, is simulated. Lam-Bremhorst turbulence model with the Yap correction is used. Main flow and bottom wall temperature profiles are presented and discussed, as well as friction coefficient and Stanton number, with or without injection. Calculations have been found in good agreement with experimental data. For the studied case, the optimum blowing rate to cool the porous wall is found to be of the order of 1% of the main flow rate.
Keywords: Turbulent Flow, Channel with Transpiration.

Teixeira, M. A. O. M., and Frota, M. N., "Wall Effects for a Sphere Falling in a Non-Newtonian Fluid", RBCM - J. of the Braz. Soc. Mechanical Sciences, Vol. 18, No. 1, pp.

The present investigation considers the problem of a sphere falling along the axis of a vertical cylindrical tube containing a non-Newtonian fluid. The wall proximity effects, characterized by the radius ratio of the sphere to the container, and the shear-thinning properties of the fluid are examined experimentally. The flow of a non-Newtonian fluid past a sphere on the centerline of a cylindrical tube is of fundamental importance to the development of falling ball viscometry techniques.
Keywords: Non-Newtonian Fluid, Wall Effects, Falling Ball Viscometry.

Revista Brasileira de Ciências Mecânicas
Revisores - 1996

Journal of the Brazilian Society of Mechanical Sciences
Referees - 1996

Álvaro Toubes Prata	UFSC
Américo Scotti	UFU
Angela O. Nieckele	PUC/RJ
Alselmo Diniz	UNICAMP
Antonio Cláudio de França Correa	UNICAMP
Aristeu Silveira Netto	UFU
Aureo Campos Ferreira	UFSC
Benedito de Moraes Purquério	USP/EESC
Benedito di Giacomo	USP/EESC
Carlos Alberto Martini	UFSC
Carlos Amadeu Pallerosi	UNICAMP
Celio Xavier	EP/USP
Deniol Katsuki Tanaka	EP/USP
Domingos Fernandes Campos	UFRGN
Edison da Rosa	UFSC
Edison Gonçalves	EP/USP
Emanuel Rocha Woiski	UNESP/FEIS
Ettore Bresciani Filho	UNICAMP
Eugênio Spanó Rosa	UNICAMP
Genésio José Menon	EFEI
Geraldo Nonato Telles	UNICAMP
Hans Ingo Weber	UNICAMP
Henrique Rozenfeld	USP/EESC
Jair Carlos Dutra	UFSC
Jesualdo Luis Rossi	IPEN-CNEN/SP
João Batista Aparecido	UNESP/FEIS
João Fernando Gomes de Oliveira	USP/EESC
José Angelo R. Gregolin	UFSCar
José Daniel Biasoli de Mello	UFU
José Luiz França Freire	PUC/RJ
José M. Saiz Jabardo	USP/EESC
José Ricardo Figueiredo	UNICAMP
Jurandir Itizo Yanagihara	EP/USP
Lourival Boehs	UFSC
Miguel Fiod Neto	UFSC
Milton Biage	UFU
Nelson Back	UFSC
Nelson F. F. Ebecken	COPPE/UFRJ
Paulo José Modenesi	UFMG
Petrônio Noronha de Souza	INPE
Rezende Gomes dos Santos	UNICAMP
Roseana da Exaltação Trevisan	UNICAMP

COBEM 95 - 13th ABCM MECHANICAL ENGINEERING CONFERENCE ISSUE
Belo Horizonte, MG - December 12-15, 1995